Microresonator Brillouin Laser Gyroscope

Thesis by
Yu-Hung Lai

In Partial Fulfillment of the Requirements for the
Degree of
Doctor of Philosophy

Caltech

CALIFORNIA INSTITUTE OF TECHNOLOGY
Pasadena, California

2019
Defended Apr 18 2019

Yu-Hung Lai
ORCID: 0000-0002-9639-6569

ACKNOWLEDGEMENTS

First of all, I appreciate the full trust of my advisor, Prof. Kerry Vahala, who gave me the freedom to explore interesting topics. He was open to crazy ideas and willing to discuss the research constraints. In the research phase, he was like a coach monitoring my performance, giving me suggestions to develop my skill sets. He challenged my results and forced me to pursue deeper toward the fundamental physics to get higher quality conclusions. He inspired me to be an efficient learner, to be a strategic planner, and to be a curious scientist. I appreciate his patience through the tough phase of my research career, and his support in helping me acquire the courage to perservere even when my life seemed to be in the middle of nowhere. *Prof. Vahala, even though I was defeated in the dark, you helped me see the light of the stars. Thank you for your accompanying me in this science quest.*

I enjoyed the experience as a teaching assistant working with Prof. Vahala, Prof. Oskar Painter, Prof. Keith Schwab, and Prof. Axel Scherer. I was amazed by their capability to deliver comprehensive lectures and to motivate students to think critically. *You ignited my passion for inspiring the next generation.*

I appreciate Prof. Oskar Painter, Prof. Harry Atwater, and Prof. Azita Emami for being my thesis committee. They helped me convey my idea more effectively. Their genuine feedback helped me polish my presentations.

Collaborating with Dr. Or Peleg, Boris Loevsky, Dr. Scott Diddams, Prof. Andrei Faraon, Dr. Jesse Frantz, and Prof. Mani Hossein-Zadeh guided me to develop my career path. I appreciate their generous sharing and discussion.

I cherish the time working with Dr. Stephanie Liefer, Dr. Gautam Vasisht, and Dr. Ivan Grudinin from JPL for the astrocomb project at W. M. Keck Observatory in Hawaii. The challenging trip became the most beautiful memory in my Caltech life – measuring the spectrum of an exoplanet from Earth with a group of professional scientists. The intense discussions reminded me of the curiosity to explore nature.

I thank my collaborators, Myoung-Gyun Shu, Yu-Kun Lu, Boqiang Shen, and Qifan Yang in the gyro project. With your suggestions and high-quality work, we pushed the research project forward together. *I appreciate your patience and persistence even when the project seemed to be impossible.*

I appreciate all of the advice from my mentor, Kiyoul Yang. Thank you for training me as an independent researcher. Your kind sharing of tough experience supported me to go over the hard situations in my life. *Thank you, my big brother. Hope you have a successful future!*

I appreciate Jiang Li, Xu Yi, Dongyoon Oh, Hansuek Lee, Seunghoon Lee, ChengYing Bao, Heming Wang, Xinbai Li, Lue Wu, and Zhiquan Yuan for their research discussions. We shared in life together in the group, and I enjoyed our chats to push the understanding of our projects further.

I appreciate the high-quality work on machining from Richard Germond, Matavos Zargarian, Ali Kiani, and Joseph Haggerty. Their sophisticated work on the machining was artful and enabled the complicated design of my system. Their dedication to the work inspired me.

I appreciate the indispensable help from Christy Jenstad, Cecilia Gamboa, Mabel Chik, Jennifer Blakenship, and Connie Rodriguez. I can trust them when I need help in the administrative process, purchasing orders, and funding. All of the discussions helped me maneuver through issues efficiently. *You are heroines of Caltech!*

I give special thanks to the director of Glee Club, Nancy Sulahian. Her music helped me enjoy vivid Caltech activities. With her warm music, I could go through the long journey of research. I have learned from experiences on stage to enjoy the moment.

Thank you, Lilien Voong. I appreciate your advice to polish my writing skills. *You relieved my writing anxiety and taught me to strengthen my writing skills. I gained confidence in writing when I saw my progress. I believe you can save lots of writers' lives like mine.*

I appreciate the generous support from DARPA, Caltech-KNI, Caltech-IQIM, and National Science Foundation. Their research funding supported me through my Ph.D. study, and made this project possible.

I thank all of my old friends in Association of Caltech Taiwanese: Chun-Lin Liu, Lucas Peng, Yuh-Shyang Wang, Min-feng Tu, Hsieh-Chen Tsai, Shu-Yu Ho, Ying-Yu Ho, Chun-Jun Hsueh, Albert Chern, Felix Chern, Kuan-Chang Chen, Tzu Chieh Chou, Ho Cheng Tsai, Yu-Hsien Hwang-Fu, Ho-Hsuan Wei, Yuri Lu, Shao Min Hung. We enjoyed events together in Caltech like a family. We chatted to find our next steps and encouraged each other to pursue our dreams.

I thank my friends, Bassam Helou, Nicole Yunger Halpern, Magnus Haw, Amanda Shing, Georgia Papadakis, Teddy Albertson, Jeremy Brouillet, Daniel Brooks, Aaron Pearlman, Dave Aasen, and Matthew Fishman. You made my life in Caltech vivid and expanded my horizons in California. I appreciate the deep discussions and the inside jokes. The Caltech-style talks are the best way to celebrate our identity.

I appreciate the warm support from my family, especially my beloved parents. Your trust gave me the courage to explore different cultures and makes my study possible. I can go the distance with your love in mind, and there is always a place called home to replenish my spirit.

Last, I appreciate my girlfriend, Yung-Hsin Kao, at Stanford. I work in optics, and you are the rainbow making life colorful. We shared the happiness and hardships in our relationships. With your honesty and gentleness and trust, I learned how to live.

This thesis is a gift for all people who have supported me through my Ph.D. study. Thank you very much.

ABSTRACT

Optical Gyroscopes are among the most accurate rotation-measuring devices and are widely used for navigation and accurate compasses. With the advent of integrated photonics for complex telecommunication chips, there has been interest in the possibility of chip-scale optical gyroscopes. Besides the potential benefits of miniaturization, such solid-state systems would be robust and resistant to shock. In this thesis, we investigate a chip-based optical gyroscope using counter-propagating Brillouin lasers on a monolithic silicon chip. The near-degenerate lasers mimic a commercial ring laser gyroscope including the existence of a locking band. By using physical properties associated with the Brillouin process, a solid-state unlocking method is demonstrated. We focus on three topics to explore the potential of the counter-propagating Brillouin-laser gyroscope. First, we explore the physics of the counter-propagating Brillouin lasers by deriving the theory to link the passive cavity mode with the lasing gain medium. We explicitly show how the dispersion, Kerr nonlinearity, dissipative coupling, and Sagnac sensing affect the beating frequency of the Brillouin lasers. Second, we experimentally demonstrate the performance of the gyroscope. Most notably, the gyroscope is used to measure the rotation of the Earth, representing an important milestone for chip-scale optical gyroscopes. Third, we investigate the non-Hermitian interaction between the counter-propagating Brillouin lasers. We test the recent prediction of the EP-enhanced Sagnac effect, and observe a Sagnac scale factor boost by over 4× by measurement of rotations applied to the resonator. Our research shows the feasibility of the chip-based Brillouin laser gyroscope. This gyroscope paves the way towards an all-optical inertial guidance system.

PUBLISHED CONTENT AND CONTRIBUTIONS

Journal Papers

[1] **Yu-Hung Lai**, Ki Youl Yang, Myoung-Gyun Suh, and Kerry J. Vahala. Fiber taper characterization by optical backscattering reflectometry. *Opt. Express*, **25**: 22312–22327, (2017). doi: 10.1364/OE.25.022312.
Y.H.L. participated in the conception of the project, fabricated fiber tapers, transferred the samples, proceeded the OFDR measurement, simulated and analyzed the data, derived the theory, and participated in writing the manuscript.

[2] **Yu-Hung Lai***, Yu-Kun Lu*, Myoung-Gyun Suh*, and Kerry J. Vahala. Enhanced sensitivity operation of an optical gyroscope near an exceptional point. *arXiv:1901.08217*, (2019).
Y.H.L. participated in the conception of the project, built the experiment setup, proceeded the measurement, co-analyzed the data, co-derived the theory, and participated in writing the manuscript.

[3] **Yu-Hung Lai***, Myoung-Gyun Suh*, Yu-Kun Lu, Boqiang Shen, Qi-Fan Yang, Jiang Li, Seung Hoon Lee, Ki Youl Yang, and Kerry J. Vahala. Earth rotation measured by a chip-scale Brillouin laser gyroscope. *arXiv preprint*, (2019).
Y.H.L. participated in the conception of the project, led the project and managed the funding, built the full experiment setup and the gyro package, proceeded the spectral measurement and the Earth rotation measurement, analyzed the data, derived the theory, and participated in writing the manuscript.

[4] Myoung-Gyun Suh, Xu Yi, **Yu-Hung Lai**, S. Leifer, Ivan S. Grudinin, G. Vasisht, Emily C. Martin, Michael P. Fitzgerald, G. Doppmann, J. Wang, D. Mawet, Scott B. Papp, Scott A. Diddams, C. Beichman, and J. Kerry Vahala. Searching for exoplanets using a microresonator astrocomb. *Nature Photonics*, **13**:25–30, (2019). doi: 10.1038/s41566-018-0312-3.
Y.H.L. participated in building the experiment setup and participated in the EOM/soliton-comb measurement in W. M. Keck Observatory, Kamuela, HI, USA.

[5] Seung Hoon Lee*, Dong Yoon Oh*, Qi-Fan Yang*, Boqiang Shen*, Heming Wang*, Ki Youl Yang, **Yu-Hung Lai**, Xu Yi, Xinbai Li, and Kerry J. Vahala. Towards visible soliton microcomb generation. *Nature Communications*, **8**: 1295, (2017). doi: 10.1038/s41467-017-01473-9.
Y.H.L. participated in building the QPSK frequency-tuning setup for soliton generation, and fabricated the fiber tapers for 1550nm, 1060nm, 778nm, and 532nm wavelength.

Conference Papers / Presentations

[1] **Yu-Hung Lai***, Myoung-Gyun Suh*, Yu-Kun Lu, Boqiang Shen, Qi-Fan Yang, Jiang Li, Seung Hoon Lee, Ki Youl Yang, and Kerry J. Vahala. Measurement of the earth's rotation using a chip-based Brillouin laser gyroscope. In *Conference on Lasers and Electro-Optics JTh5A.8*, (2019). doi: 10.1364/CLEO_AT.2019.JTh5A.8.
Y.H.L. participated in the conception of the project, led the project, built the experiment setup, proceeded the spectral measurement and the Earth rotation measurement, analyzed the data, derived the theory, wrote the manuscript, and presented in the post-deadline oral session.

[2] **Yu-Hung Lai**, Myoung-Gyun Suh, and Kerry J. Vahala. A Brillouin optical gyroscope using a high-Q silica-on-silicon optical microcavity. In *SPIE Photonics West OPTO 10934-12*, (2019).
Y.H.L. participated in the conception of the project, led the project, built the experiment setup, proceeded the measurement, analyzed the data, derived the theory, and gave the talk.

[3] Dong Yoon Oh*, Qi-Fan Yang*, Seung Hoon Lee*, Heming Wang*, Boqiang Shen*, Ki Youl Yang, **Yu-Hung Lai**, Xu Yi, and Kerry J. Vahala. Towards visible soliton microcomb generation. In *Nonlinear Optics, NTh3A.3*. Optical Society of America, (2017). doi: 10.1364/NLO.2017.NTh3A.3.
Y.H.L. participated in building the QPSK frequency-tuning setup for soliton generation, and fabricated the fiber tapers for 1550nm, 1060nm, 778nm, and 532nm wavelength.

[4] Kerry J. Vahala, **Yu-Hung Lai**, Myoung-Gyun Suh, and Jiang Li. A Brillouin gyroscope using chip-integrable high-Q optical cavities. In *Advanced Photonics (BGPP, IPR, NP, NOMA, Sensors, Networks, SPPCom, SOF) IM3I.2*. Optical Society of America, (2018). doi: 10.1364/IPRSN.2018.IM3I.2.
Y.H.L. participated in the conception of the project, built the experiment setup, proceeded the measurement, co-analyzed the data, and proofread the manuscript.

[5] Kerry J. Vahala, **Yu-Hung Lai**, Myoung-Gyun Suh, Jiang Li, and Ki Youl Yang. Towards integrated optical gyros using Brillouin lasers. In *Solid-State, Actuators, and Microsystems Workshop*, (2018). doi: 10.31438/trf.hh2018.23.
Y.H.L. participated in the conception of the project, built the experiment setup, proceeded the measurement, co-analyzed the data, and proofread the manuscript.

[6] Kerry J. Vahala, **Yu-Hung Lai**, and Myoung-Gyun Suh. An on-chip optical Brillouin gyroscope with earth-rotation-rate sensitivity. In *Conference on Lasers and Electro-Optics FTu3B.1*, (2019). doi: 10.1364/CLEO_QELS.2019.FTu3B.1.

Y.H.L. participated in the conception of the project, built the experiment setup, proceeded the measurement, and co-analyzed the data.

[7] Qi-Fan Yang*, Seung Hoon Lee*, Dong Yoon Oh*, Boqiang Shen*, Heming Wang*, Ki Youl Yang, **Yu-Hung Lai**, Xu Yi, and Kerry J. Vahala. Soliton microcomb operation to 778 nm. In *IEEE Photonics Conference (IPC)*, pages 139–140, (2017). doi: 10.1109/IPCon.2017.8116040.
Y.H.L. participated in building the QPSK frequency-tuning setup for soliton generation, and fabricated the fiber tapers for 1550nm, 1060nm, 778nm, and 532nm wavelength.

[8] Yu-Kun Lu, **Yu-Hung Lai**, Myoung-Gyun Suh, and Kerry J. Vahala. Exceptional points in microresonator Brillouin laser systems. In *APS March Meeting **64**(2) F23.00006*, (2019).
Y.H.L. participated in the conception of the project, built the experiment setup, proceeded the measurement, and co-analyzed the data.

*These authors contributed equally to this work.

TABLE OF CONTENTS

LIST OF ILLUSTRATIONS

NOMENCLATURE

AM. Amplitude Modulation.

AOM. Acousto-Optic Modulator.

CCW. Counterclockwise.

CROW. Coupled-Resonator Optical Waveguide.

CW. Clockwise.

ECDL. External Cavity Diode Laser.

EDFA. Erbium-Doped Fiber Amplifier.

EMI. Electromagnetic Interference.

EOM. Electro-Optic Modulator.

EP. Exceptional Point.

ESA. Electrical Spectrum Analyzer.

FC. Frequency Counter.

FFT. Fast Fourier Transform.

FM. Frequency Modulation.

FOG. Fiber Optic Gyroscope.

FSK. Frequency Shift Keying.

FSR. Free Spectral Range.

FWHM. Full-Width-Half-Maximum.

FWM. Four-Wave-Mixing.

LED. Light-Emitting Diode.

MEMS. Micro-Electro-Mechanical Systems.

OBR. Optical Backscattering Reflectometry.

OFDR. Optical Frequency Domain Reflectometry.

OSA. Optical Spectrum Analyzer.

PD. Photo-Detector.

PI. Proportional-Integral (servo).

PID. Proportional-Integral-Derivative (servo).

PM. Phase Modulation / Phase Modulator.

PZT. Lead Zirconate Titanate ($Pb[Zr(x)Ti(1-x)]O_3$), a piezoelectric material.

QPSK. Quadrature Phase Shift Keying.

RF. Radio Frequency.

RLG. Ring Laser Gyroscope.

SBL. Stimulated Brillouin Laser.

SBS. Stimulated Brillouin Scattering.

SCISSOR. Side-Coupled Integrated Spaced-Sequence of Resonators.

SEM. Scanning Electron Microscope.

TEC. Thermoelectric Cooler.

UHQ. Ultra-High-Quality factor.

VCO. Voltage-Controlled-Oscillator.

WGM. Whispering-Gallery Mode.

Chapter 1

INTRODUCTION OF OPTICAL GYROSCOPES

1.1 Introduction of the Sagnac effect

Optical gyroscopes are rotation-measurement devices based on the Sagnac effect, a small phase difference of laser lights propagating in opposite directions under rotation[1, 2]. When clockwise (CW) light and counterclockwise (CCW) light travel around closed paths in a steady plane, their propagation times are equal. However, when the plane is rotating, the counter-propagating lights experience different travel times due to the path length difference under rotation (Figure 1.1). This time difference can be precisely measured by using optical interference and converted into a phase shift or frequency shift. By tracking the beating shift of the counter-propagating lights, we can measure the rotation.

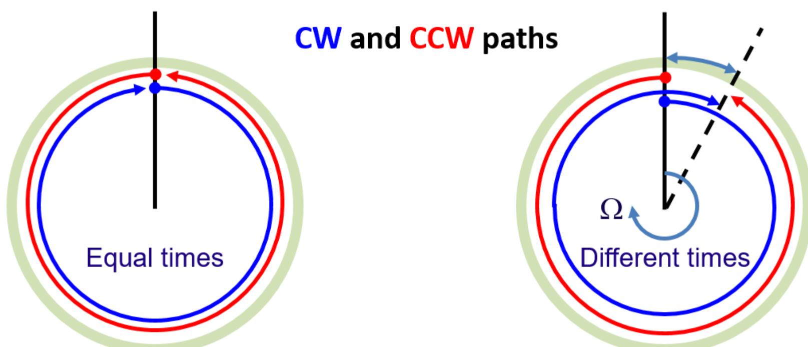

Figure 1.1: **Sagnac Effect. Left:** When the clockwise (CW) light and the counterclockwise (CCW) light are propagating in a close loop, their propagation time should be equal if the system is steady. **Right:** When the loop is rotating, the CW and CCW lights travel back to the same point on the loop at the different time. The counter-propagating lights have a path length difference which can be detected as a phase shift or a frequency shift.

1.2 Commercial gyroscope

Currently, the high-end commercial market is dominated by optical gyroscopes. They create long physical or effective pathlengths to boost the sensitivity of the gyroscope. The mature products are the He-Ne ring laser gyroscope (RLG)[3] and the fiber optic gyroscope (FOG)[4–6]. Both of them can achieve sub-millidegree per hour sensitivity and bias drift. The performance allows these gyroscopes to be useful for a wide range of applications in the markets of automation, navigation, and positioning[7–9].

He-Ne ring laser gyroscope

The He-Ne ring laser gyroscope (Figure 1.2a) uses a glass ring tube to hold the Helium-Neon mixture and excites the gas as a gain medium to generate the counter-propagating laser. Because the quality factor of the resonator (glass tube) is ultra-high, the counter-propagating lights circulate millions to billions times within the resonator to create huge effective pathlength. Equivalently, the linewidth of the laser is very narrow, so a small frequency shift under rotation can be detected by the following equation[2]:

$$\delta\nu = \frac{4\mathbf{A}\cdot\Omega}{\lambda P}, \tag{1.1}$$

where $\mathbf{A}$ is the surface area vector enclosed by the counter-propagating light, Ω the rotation velocity vector, λ the light wavelength, and P the roundtrip optical pathlength, which depends on the refractive index.

The back-scattering and loss lock the counter-propagating lights and create a deadband in the gyro readout[3]. To minimize the deadband, the glass tube and electrodes are designed symmetrically. In addition, applying mechanical dithering further unlocks the gyro operation for sensitive measurement.

Fiber optic gyroscope

The fiber optic gyroscope (Figure 1.2b) uses a long fiber spool to create a long physical pathlength for the counter-propagating lights. The beating of the lights is equivalent to the Michelson interferometry and generates a phase shift under rotation. The phase shift is determined by the following equation[2]:

$$\delta\phi = \frac{8\pi N\mathbf{A}\cdot\Omega}{\lambda c}, \tag{1.2}$$

where N is the number of the loops, $\mathbf{A}$ the surface area vector of a single loop, c the speed of light. Specifically, the phase shift under rotation is independent of the refractive index of the medium. With a huge number of loops, the fiber optic gyroscope can achieve extreme accuracy and sensitivity.

The sensitivity of the fiber optic gyroscope is limited by material loss, scattering, and bending. In addition, the coherence of the lasers affects the readout noise. To maximize the signal to noise ratio, several methods have been applied, such as reciprocal cancellation, reverse or dual phase modulation, low-coherence interference with the superluminescent diode, and balanced detection[4, 6].

MEMS gyroscope

Another category of gyroscopes is the MEMS gyroscope, which uses integrated electronics and micromechanical components to detect the Coriolis effect under rotation[10]. The sensing components are fully integrated on a microchip such that the overall footprint is less than $1\text{cm}^2 \times 1\text{cm}^2$ (Figure 1.2c). The manufacturing process further reduces the overall cost of the MEMS gyroscopes, so they are widely used in cellphones and dominate the portable market, which requires the sensitivity above $10^\circ/\text{h}$.

The success of the MEMS gyroscope demonstrates well the capability of the integration technology. It is obvious that the optical gyroscope could follow a similar roadmap with the integrated photonics. Integrated photonics can interconnect the optical and electrical components on a single chip, so the rugged structure without moving components enables the operation in the harsh environment such as high-G vibration or ballistic shock. The reduced size may further reduce the drift sources for better performance.

Figure 1.2: **Commercial Gyroscopes.** **a,** Helium-Neon ring laser gyroscope.∗ **b,** Fiber optic gyroscope.† **c,** MEMS gyroscope.‡

1.3 Chip-based optical gyroscope

In the past decades, several chip-based optical gyroscopes have been proposed, but are not demonstrated until recently. Here, we quickly review the chip-based optical gyroscope[11].

Microresonator Brillouin laser gyroscope

The microresonator Brillouin laser gyroscope uses the solid-state material as a gain medium to generate the backward propagating Brillouin lasers[12, 13]. The Brillouin lasing process is directional and can be cascaded, so intrinsically the

[*]Photo: NCSIST http://www.ncsist.org.tw/eng/csistdup/products/product.aspx?product_Id=189&catalog=21
[†]Photo: EMCORE http://emcore.com/products/eg-200-fiber-optic-gyroscope-fog/
[‡]Photo: DARPA https://www.darpa.mil/program/micro-technology-for-positioning-navigation-and-timing

counter-propagating Brillouin lasers do not interact with each other. The independent counter-propagating Brillouin lasers, therefore, sense the Sagnac rotation and become a chip-based ring laser gyroscope. Currently, the silica on silicon resonator (Figure 1.3a) and the silicon nitride platform (Figure 1.3b) have been demonstrated. We investigate the microresonator Brillouin laser gyroscope on a silica-on-silicon chip in this thesis.

Integrated interferometric optical gyroscope

The integrated interferometric optical gyroscope uses a long spiral waveguide to maximize the enclosed Sagnac sensing area on a chip (Figure 1.3c)[14]. This gyroscope mimics the fiber optic gyroscope to detect the phase change of the counter-propagating lasers under rotation. Currently, the waveguide loss limits the maximum available sensing area and gyro performance.

Resonator micro-optical gyroscope

The resonator micro-optical gyroscope (RMOG) uses a passive cavity to detect the nonreciprocal shift of the mode. The CW and CCW passive modes split under rotation, and the mode shift can be detected from the PDH error signal, the coupling power change, or the optical spectrum[15–17]. The RMOG draws attention due to the simplicity of the structure design. How to improve the resolution and to suppress the drift are active research fields (Figure 1.3d-f).

Semiconductor ring laser gyroscope

The semiconductor ring laser gyroscope uses III-V material as a gain medium to amplify the counter-propagating lasers. The lasers are both amplified by a single gain medium, so the mode competition poses a constraint on the gyro operation similar to the He-Ne ring laser gyroscope. The gyro performance is still under investigation[11].

Coupled resonator gyroscope

The coupled resonator gyroscope uses multiple rings to couple the counter-propagating lights. The interaction from the coupling lifts the modes by dispersion[18] and creates nonlinear readout shifts under rotation. Famous examples include CROW[19] and SCISSOR[20]. The Sagnac factor can be enhanced such that a small rotation induces a huge change of the response near the modal splitting point.

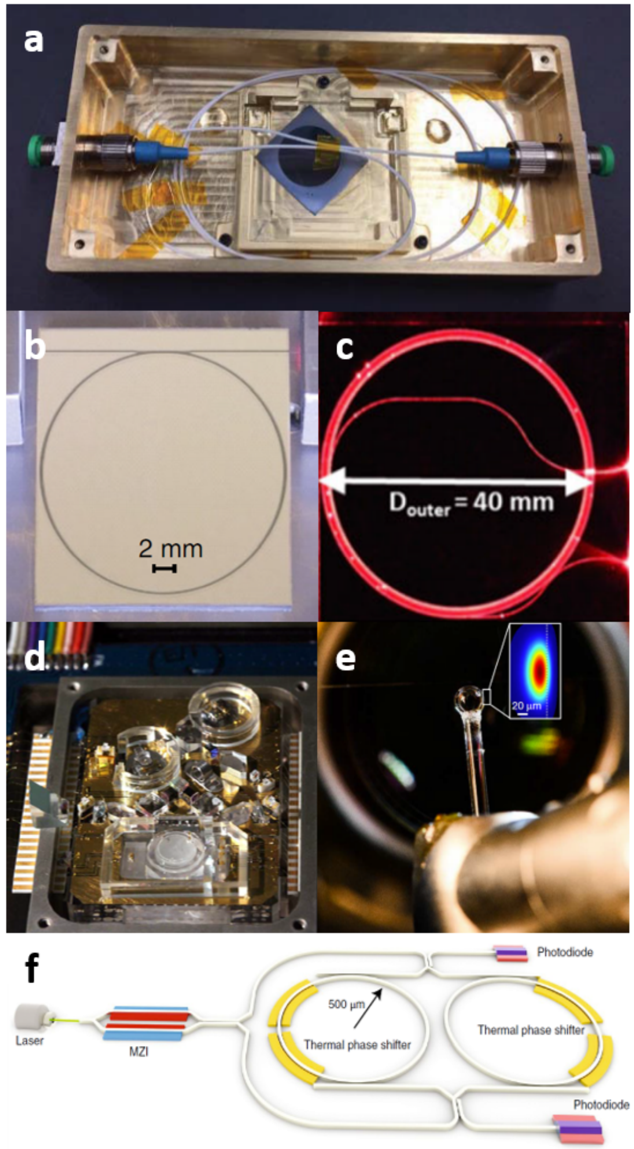

Figure 1.3: **Recent Chip-Based Gyroscopes.** **a,** A microresonator Brillouin laser gyroscope made from a chip-based silica-on-silicon microresonator coupled with fiber taper waveguide.[12] **b,** A microresonator Brillouin laser gyroscope made from a chip-based silicon nitride waveguide resonator.[13] **c,** An integrated interferometric optical gyroscope made from silicon nitride spiral waveguide.[14] **d,** A resonator micro-optical gyroscope made from calcium fluoride crystalline resonator.[15] **e,** A spherical silica resonator testing the nonreciprocal splitting under rotation.[16] **f,** A resonator micro-optical gyroscope made from two silicon nitride rings for reciprocal drift suppression under dithering.[17] (Figures are adapted from the references.)

1.4 Summary of the Chapters

Based on the knowledge of the commercial ring laser gyroscope, we investigate the Sagnac sensing on a chip-based platform. In this thesis, we demonstrate a ring laser gyroscope by a silica microresonator using Brillouin gain. A novel offset counter-pumping approach is used to create independent counter-propagating laser waves whose difference in frequency is sensitive to rotation rate. To capture this rotation readout, we develop the theoretical model to show the signal and drift sources of the gyroscope. Then, we demonstrate the gyroscope's sensitivity by sinusoidal rotation measurement, and further show the Earth's rotation measurement as a milestone of the gyroscope performance. Finally, we show the Sagnac factor enhancement near the exceptional point. In addition, because the gyroscope is coupled by a silica fiber taper, we demonstrate how to characterize fiber tapers in a separate chapter.

The thesis is organized as follows:

In Chapter II, we introduce the optical microresonators and their applications in nonlinear optics. Then, we quickly review the physics and performance of the Brillouin lasers. In the later part, We showed the recent demonstration of the cascaded Brillouin laser gyroscope.

In Chapter III, we introduce a new scheme of the counter-pumped Brillouin lasers. We investigate the physics of the SBLs such as mode-pulling effect, dissipative-coupling-induced locking, Kerr nonlinearity, and the Sagnac shift. The drift sources and possible feedback scheme are further discussed.

In Chapter IV, we demonstrate the performance of the counter-pumped Brillouin laser gyroscope by showing the sinusoidal rotation measurement, the Allan deviation traces, and the drift reduction algorithm. We measure the Earth's rotation as a milestone of the gyro performance.

In Chapter V, we introduce the recently predicted enhancement of the gyro Sagnac factor from the exceptional point (EP). We show the underlying physics of the modal coupling and demonstrate an enhancement factor near EP.

In Chapter VI, we show the fabrication and characterization of the silica fiber taper waveguide, which is an indispensable component to couple the light into the silica microresonator on a chip.

In Chapter VII, we conclude the findings in this thesis.

Chapter 2

BRILLOUIN LASERS IN SILICA MICRORESONATORS

2.1 Whispering-gallery-mode Microresonators

A whispering-gallery-mode resonator is a structure made into a circular shape such as a disk, a sphere, or a rod. The light or sound wave can circulate around its circumference through the total internal reflection, and store the energy in the resonant mode[21, 22]. For example, in St. Paul's Cathedral, sound can be guided near the wall of a circular chamber, so a whisper from one side of the room is clearly heard at the other side (Figure 2.1). This phenomenon shows how the "whispering-gallery-mode (WGM)" gets its name.

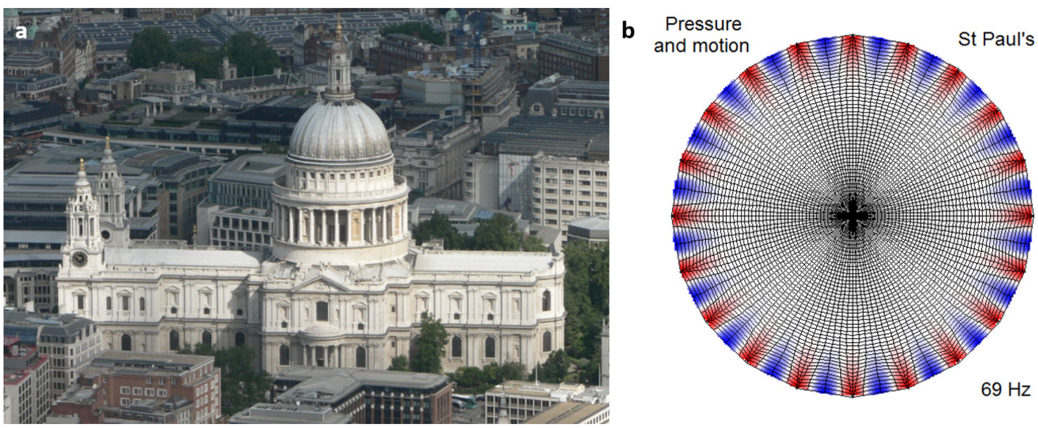

Figure 2.1: **Whispering-Gallery-Mode in St Paul's Cathedral. a,** Picture of St Paul's Cathedral. The circle-shaped wall guides the acoustic wave near the circumference, such that a whisper from one side of the dome can be heard clearly at the opposite side.∗ **b,** Simulation of an acoustic mode in St Paul's Cathedral. The acoustic wave is stored in the structure and circulates along the wall to cause the whispering-gallery effect.†

In the past decades, a wide range of studies have investigated the physics of the WGM microresonators with different shapes, materials, and structures[22, 23]. To characterize the performance of the whispering gallery mode, a number called quality factor (Q) is used. The Q factor is defined by the mode frequency (ν) over linewidth ($\Delta\nu$), and equivalently equals to the ratio of the stored energy (E_{mode}) over

∗Photo: Wikipedia (By Mark Fosh) https://commons.wikimedia.org/w/index.php?curid=46084308
†Photo: Wikipedia (By Femtoquake) https://commons.wikimedia.org/w/index.php?curid=18233779
Simulation: Applied Solid State Physics Laboratory, Division of Applied Physics, Faculty of Engineering, Hokkaido University Sapporo, Japan.

power loss (P_{loss}) times modal angular frequency ($\omega \equiv 2\pi\nu$).

$$Q \equiv \frac{\nu}{\Delta\nu} = \omega\frac{E_{\text{mode}}}{P_{\text{loss}}}. \tag{2.1}$$

The Q factors of these resonators depend on the material absorption and the scattering process. Typical Q factor ranges from 10^4 to 10^{10}. With these Q factors, a small fraction of coupled power becomes a huge circulating intensity in the resonator. For example, 1 mW of coupled power (P_c) to a 3mm-diameter ($V_{\text{mode}} = 5\times10^5\mu\text{m}^3$) silica wedge disk with Q = 200 million at 1.55μm wavelength becomes a circulation intensity (I_{circ}) around 10MW/cm^2 in the resonator by

$$I_{\text{circ}} = \frac{c}{V}\int_t^{t+\tau} P_c dt' \approx \frac{Q}{V}\frac{c}{\omega}P_c. \tag{2.2}$$

Such a high circulating intensity in a cavity enables nonlinear interactions between lights and materials[24]. For example, the photon-phonon interaction enables stimulated Brillouin scattering[25–29], stimulated Raman scattering[30], and optomechanics[31–35]. The photon-photon interaction enables four-wave-mixing[36, 37], soliton generation[38–40], second harmonic generation[41], and third harmonic generation[41]. Therefore, optical microresonators become platforms to test the nonlinear optics, quantum optics, and laser physics[42–45]. By properly designing the resonator, we can implement the microresonators as active or passive optical devices on a chip, and design functional integrated photonic systems[13, 46, 47]. A wide range of applications has been demonstrated recently, such as the sub-Hertz linewidth laser[13, 47, 48], rotation sensor[12–17], reference cavity[49, 50], microwave generation for frequency synthesizer[27, 51], spectroscopy[52–54], range finder[55, 56], imaging[57], and optical clock[58]. The microresonator is a critical component in the photonics era.

Another key parameter of the microresonator is the free spectral range (FSR), which is defined by the frequency difference between adjacent modes in the same mode family. In a WGM, the FSR is calculated by

$$\pi D n_g = m\lambda_m = m\frac{c}{\omega_m}, \tag{2.3}$$

$$\text{FSR} \equiv \omega_{m+1} - \omega_m = \frac{c}{\pi D n_g}, \tag{2.4}$$

where D is the size of the resonator, n_g the modal group refractive index, m the azimuthal mode number, λ_m and ω_m the corresponding wavelength and frequency in free space, and c the speed of light. The FSR is used for characterizing the round trip time of a microresonator. In addition, the FSR captures the modal group refractive index, which depends on the material, geometry, and active process of a cavity. Therefore, the change of the FSR is used for characterizing the group dispersion (group refractive index change at different frequencies).

To couple the light into microresonators, several studies use free space coupling, butt coupling, or evanescent coupling by either fiber tapers or prisms. Throughout this thesis, we couple silica microresonators with fiber tapers (Figure 2.2)[59, 60]. The taper width is similar to the wavelength, so the light leaks out from the taper core into the air and interacts with the WGM in the microresonator. The taper coupling provides a wide range of tunability for fast characterization of the microresonator and is even used in the packaged device. For detailed characterization of fiber tapers, please see Chapter VI.

Figure 2.2: **Coupling of Silica Disk.** A silica microresonator was coupled by a silica fiber taper (the thin white line in the picture). The fiber taper has a width close to the optical wavelength, so the evanescent wave leaks out and couples to the microresonator. The quality factor of the silica microresonator can reach over 100 M, so a small fraction of coupling light becomes a huge circulating intensity in the cavity. The nonlinear process is generated once the phase matching condition is achieved. (Photo: Yu-Hung Lai)

2.2 Brillouin laser generation

A Brillouin laser is the light amplification by Brillouin scattering[28, 61–63]. When a coherent light wave is propagating in a material, the amplitude of the light wave causes force on the atoms and changes the refractive index locally. Equivalently, light generates a grating in a material. If another light with different frequency propagates in the opposite direction, the interference of the two lights generates a moving grating. This grating propagates in the material like acoustic waves and transfers the energy and momentum quantized as acoustic phonons. The grating also scatters the pump photon into a back-propagating photon called Stokes photon (Figure 2.3). This process is called Brillouin scattering.

In silica, Brillouin scattering has a bandwidth of $20 - 60$ MHz[64], and the phonon frequency is around 10.8 GHz. Now, we add a resonator. If we precisely control the dimension of the resonator such that the backscattered light is held in the resonator, and the SBS gain band is aligned with the optical mode, this process is actively enhanced. The pump continuously generates the phonons and SBS photons in the resonator, and the SBS photons further speed up the coherent conversion process. The coherent SBS photons start to lase when the pump intensity is above the threshold (Figure 2.4).

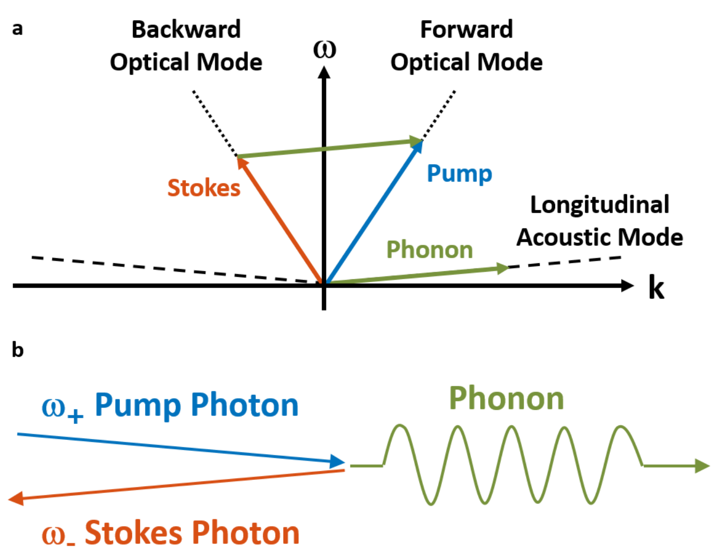

Figure 2.3: **SBS Diagram. a,** The dispersion diagram of the SBS process. When pump light is propagating in a medium, the pump photon interacts with the lattice and decays into a backward Stokes photon and an acoustic phonon. **b,** A simplified SBS process depicts the phase matching condition. The interference of the pump and the Stokes field generates a moving grating (phonon) in the medium.

To calculate the Brillouin shift, we consider the energy and momentum conservation laws,

$$\text{Energy Conservation:} \quad \hbar\omega_p = \hbar\omega_s + \hbar\Omega_B, \tag{2.5}$$

$$\text{Momentum Conservation:} \quad \hbar k_p = -\hbar k_s + \hbar k_B, \tag{2.6}$$

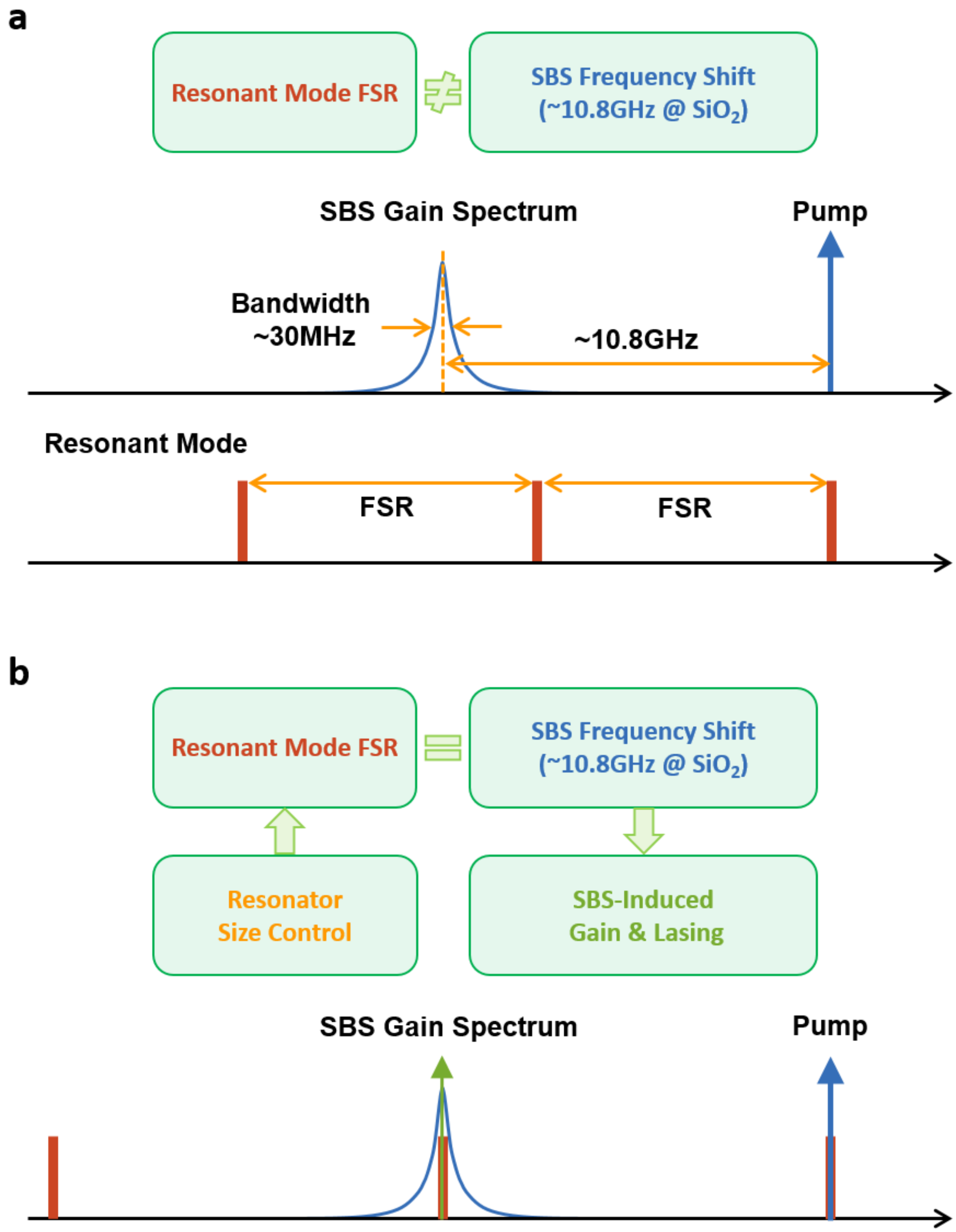

Figure 2.4: **SBL Generation Process.** **a,** When the resonant mode and the SBS gain spectrum are mismatched, even though the pump intensity is very high, the SBS photon cannot be stored. Therefore, the lasing process is rejected. **b,** By precisely controlling the size of the resonator, the resonant mode and the SBS gain spectrum are matched. The SBS photon can be stored in the resonator and further amplified. Once the pump exceeds the threshold, the coherent Stokes field starts to generate SBL.

where ω_p (k_p), ω_s (k_s), Ω_B (k_B) are the angular frequency (wavevector) of pump photon, Stokes photon, and Brillouin phonon, respectively. We can rewrite Eq. (2.6) by using the dispersion relation:

$$k_B = \frac{\Omega_B}{c_s} = \frac{n}{c}\left(\omega_p + \omega_s\right) = k_p + k_s, \tag{2.7}$$

where c_s is the speed of sound in the medium, c the speed of light in vacuum, and n the refractive index of the medium. Since $\omega_p \approx \omega_s \gg \Omega_B$, we simplify the equation as:

$$\Omega_B \approx \frac{2nc_s\omega_p}{c} = \frac{4\pi nc_s}{\lambda_p}, \tag{2.8}$$

where λ_p is the wavelength of the pump in vacuum.

The Brillouin scattering process is originally a parametric process. When the acoustic field decays much faster than the optical field does, the damped acoustic phonons are adiabatically eliminated from the system, such that the remaining optical photons are amplified. Therefore, the parametric process turns into a stimulated scattering process.

As an aside, when the acoustic field decays much slower than the optical field does, the phonon mode is amplified and becomes a phonon laser (phaser)[31, 33]. The cavity optomechanics dominates in such a system, and interesting phonon cooling[29] or optomechanics-induced transparency[65] can be observed.

2.3 Cascaded Brillouin laser

The Brillouin scattering process can be cascaded when the phase matching condition of the high order Stokes light is achieved. When the original pump light is high enough, the high intensity of the first order Stokes light acts as a new pump for the second order Stokes light. The second order Stokes light starts to lase once the gain exceeds the loss (threshold). This process can continue as long as the high order Stokes lights can be stored in the resonators and the pump power can compensate the overall loss mechanisms in the Brillouin scattering process (Figure 2.5). Due to the backscattering nature of SBS, we intrinsically generate counter-propagating SBLs in the resonator.

We visualize this process from the frequency spectrum. If the modes of the resonator are aligned with the mode of SBLs, each order of SBL can be stored in the resonator and further amplify the next order SBL. (Figure 2.6) This process is called the cascaded generation of SBLs. In the cascaded process, the propagation direction of

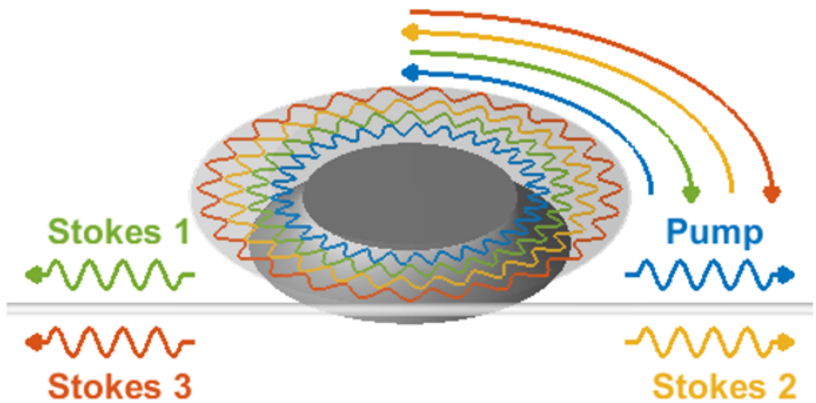

Figure 2.5: **Cascaded SBS in the Microresonator.** When the SBS frequency shift equals to a multiple of free spectral range of the resonator, the SBS process can be cascaded. Once the pump power (blue) is high enough, the corresponding first order Stokes power (green) acts as a pump to amplify the second order Stokes (yellow). Similarly, the third order Stokes (red) starts to lase when the pump is further increased.

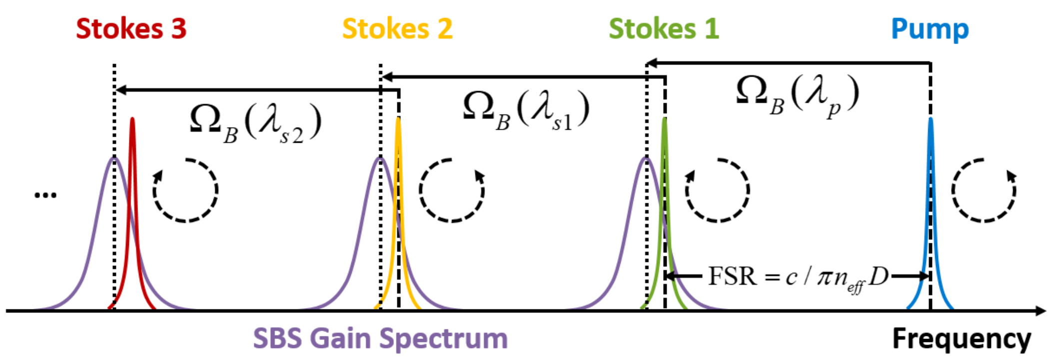

Figure 2.6: **Cascaded SBS spectrum diagram.** The cascaded SBS process is a natural way to generate counter-propagating Brillouin lasers in a resonator. The even-order Stokes laser and the odd-order Stokes laser have opposite propagating direction, so their beating captures the Sagnac rotation shift. Ω_B is the Brillouin angular frequency shift.

SBLs flips at each order. The even-order Stokes laser and the odd-order Stokes laser have opposite circulating directions. The beating of the counter-propagating SBLs, therefore, captures the Sagnac rotation shift.

In our experiment, we generate the cascaded SBLs up to 9^{th} order (Figure 2.7a). We detect the light at one output of the fiber taper waveguide, so the high peaks (odd order Stokes) shows the output from the resonator, and the low peaks (even order Stokes) shows the backscattering in the system. This asymmetry indicates the counter-propagating natures of the even/odd order SBLs. In addition, we check the beating of the 1^{st} order and 3^{rd} order SBLs. The beating frequency is around twice

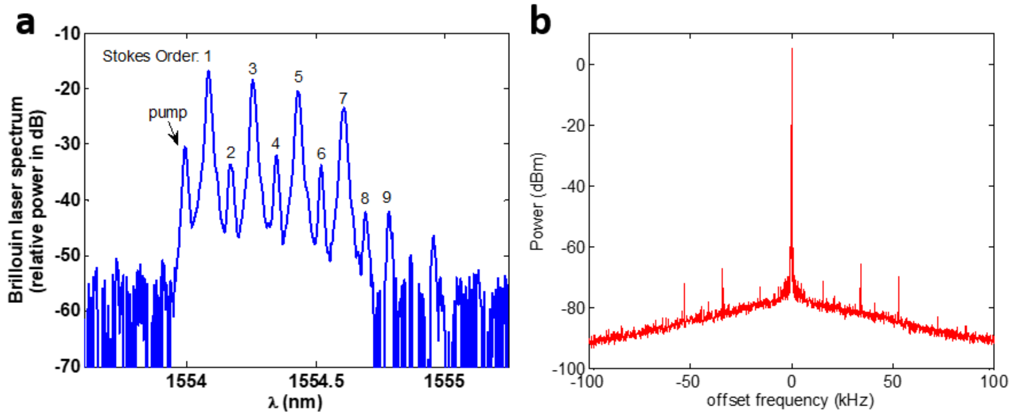

Figure 2.7: **Cascaded SBL Spectrum and Linewidth. a,** The cascaded SBL is generated up to 9^{th} order. The photodetector detects the SBLs from the odd order sides of the fiber waveguide. The pump and the even-order SBLs are detected due to the back-reflection (≈ -20 dB) in the optical line. **b,** the beating linewidth of the 1^{st} order and the 3^{rd} order SBL. The beating frequency is around 21.7 GHz. Since the lasers are in the same resonator, most of the common noise has been canceled. In addition, the SBL linewidth is Schawlow-Townes noise limited, so the beating linewidth can be less than a Hertz. (This figure is adapted from reference [48].)

the Brillouin shift and the linewidth is less than a Hertz. The sub-Hertz linewidth comes from two reasons. First, the lasers are held in the same resonator, so most of the common noise has been canceled through the beating process. Second, the SBL linewidth is Schawlow-Townes noise limited, and the high-quality factor of the resonator narrows the linewidth of the SBL (Figure 2.7b).

To verify that the counter-propagating SBLs track the Sagnac shift, we packaged an 18mm-diameter disk in a brass package. One end of the package was fixed at a pivot point, and another end of the package was put on a piezoelectric stage. By modulating the stage, we applied a sinusoidal rotation on the resonator in parallel with the resonator axis and detected the beating frequency change of the counter-propagating SBLs. In Figure 2.8, the beating frequency shows 90° phase shift relative to the angular displacement, indicating the beating frequency change tracks the rotation properly. The minimal measured root-mean-square rotation rate is 22°/h. This result is the first demo of a microresonator Brillouin laser gyroscope[12].

The gyro readout frequency of the cascaded Brillouin laser gyroscope is at the microwave region ($\approx$ 10.8 GHz). Building a readout circuit at microwave band with Hertz level resolution complicates the electronic system design. To further simplify the system for integration, a lower readout frequency is preferred. We introduce a novel method to generate the gyro readout at the audio rate in the next chapter.

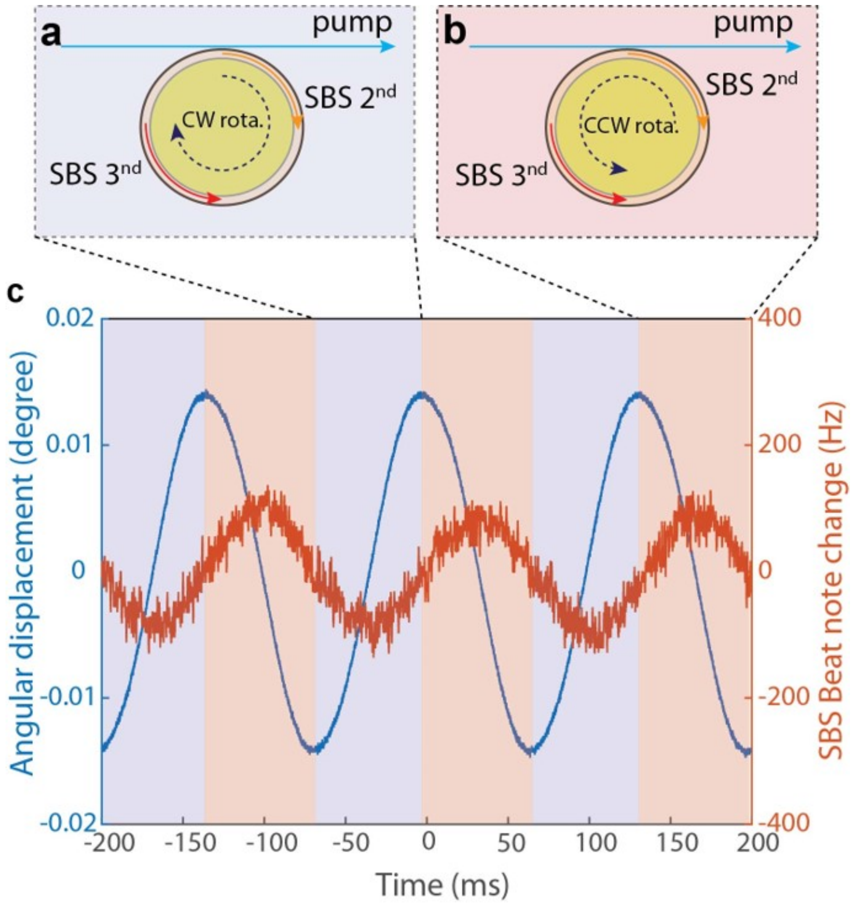

Figure 2.8: **Cascaded SBL for Rotation Sensing. a & b,** We packaged the resonator and applied a sinusoidal rotation on the resonator. The blue, orange, and red arrows show the direction of the pump, 2^{nd} order SBS, 3^{rd} order SBS, respectively. The black dashed arrow shows the direction of the external rotation. **c,** We read out the beating frequency of the 2^{nd} order SBL and the 3^{rd} order SBL, and compare the trace with the modulated angular displacement. The 90° phase shift shows the differential nature between the angular displacement and the angular velocity. (This figure is adapted from reference [12].)

Chapter 3

PHYSICS OF THE COUNTER-PUMPED BRILLOUIN LASER

In this chapter, we introduce a new method to generate the nondegenerate counter-propagating SBLs in a microcavity. By precisely controlling the frequencies of the counter pumps, the nonzero detuning frequency of the pump unlocks the corresponding SBLs. We use the coupled mode theory to show that the Brillouin gain-induced dispersion causes the mode-pulling effect. The mode-pulling effect suppresses the SBL beating signal to acoustic or ultrasound frequency. The low-frequency readout simplifies the requirement of the readout electronics. In addition, we show that dissipative coupling induces the locking zone and generates high harmonics in the SBL beating spectrum. The SBL beating signal captures the Sagnac rotation such that the Sagnac factor can be precisely measured. On the other hand, we investigate the drift mechanism caused by Kerr nonlinearity and temperature. We showed that these two effects are dominant limiting factors of the gyro performance. Based on our findings, we may design the active feedback control for high-performance gyroscopes in the future.

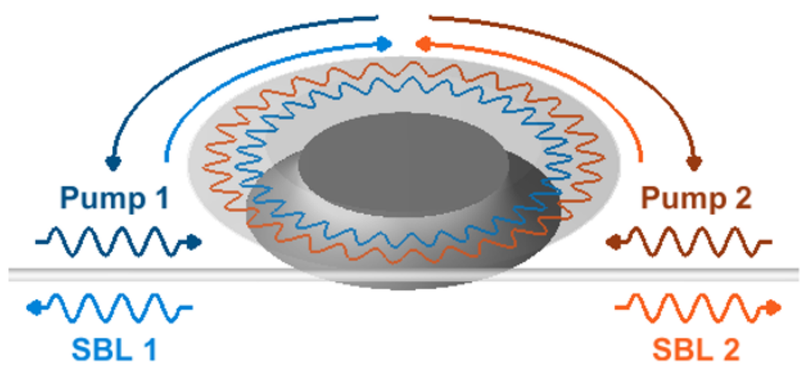

Figure 3.1: **Conceptual illustration of counter-pumped stimulated Brillouin laser.** When the microresonator is counter-pumped in the same cavity mode, each pump generates its own corresponding stimulated Brillouin lasers. Since the CW and CCW Brillouin gains do not interact with each other due to the phase matching condition, the counter-propagating SBLs are independent.

Part of this chapter was adapted from the paper, Y.-H. Lai, et al., “Earth rotation measured by a chip-scale Brillouin laser gyroscope,” arXiv preprint (2019).

3.1 Mode-pulling equation

In an ultra-high-Q microresonator, the stimulated Brillouin laser is generated and amplified when both the pump photons and the scattered Brillouin photons are stored in the resonator simultaneously. The phase matching conditions make the Brillouin gain directional, so the counter-propagating pumps excite their own corresponding SBLs independently (Figure 3.1). When the two pumps have a nonzero detuning frequency ($\Delta\nu_p$), the corresponding SBL frequencies are pulled apart as a result of Brillouin-induced dispersion. This pulling induces a splitting in the SBL beating frequency ($\Delta\nu_s$) that inhibits locking of the laser frequencies as a result of backscattering (Figure 3.2).

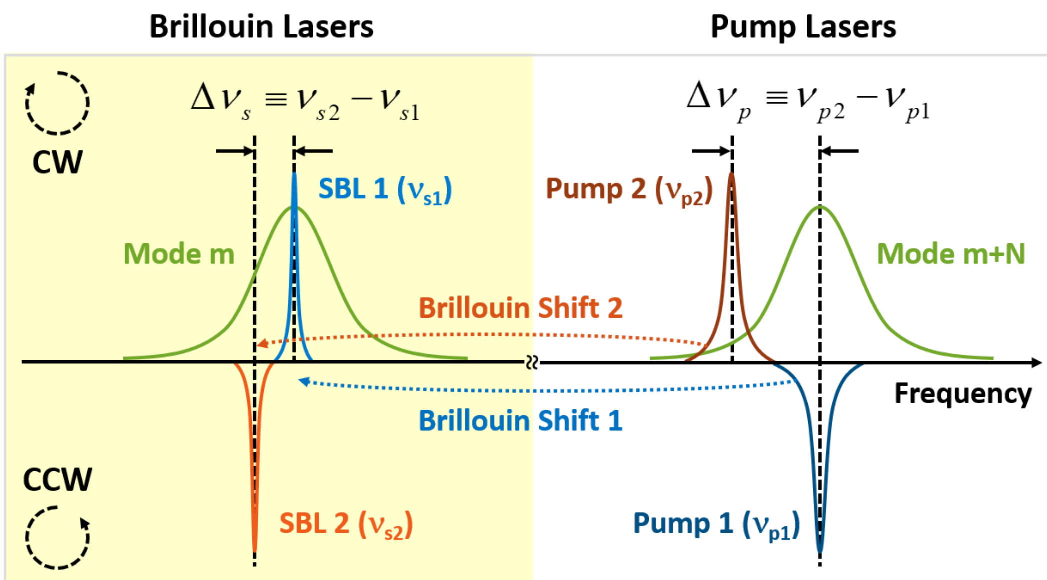

Figure 3.2: **The spectral diagram of the offset-counter-pumped SBL.** The pump detuning frequencies are precisely controlled and independently shifted. The nonzero pump detuning ($\Delta\nu_s$) unlocks the gyroscope through Brillouin-induced dispersion (mode pulling). The non-degenerate SBL beating frequency captures the Sagnac rotation. ($N = 6$ in a 36mm silica disk.)

We introduce the coupled mode theory to analyze the counter propagating SBLs. The equations in the cavity-mode rotating frame are:

$$\dot{\alpha_1} = \left[i\left(\omega_{s1} - \omega_0\right) - \frac{\gamma}{2} \right] \alpha_1 + g_1 \left|A_1\right|^2 \alpha_1 \tag{3.1}$$

$$\dot{\alpha_2} = \left[i\left(\omega_{s2} - \omega_0\right) - \frac{\gamma}{2} \right] \alpha_2 + g_2 \left|A_2\right|^2 \alpha_2, \tag{3.2}$$

where $A_{1,2}$ are the photon number amplitudes of the pumps, $\alpha_{1,2}$ the photon number amplitudes of the SBLs, γ the photon decay rate, $\omega_{p1,p2}$ the pump angular frequencies, $\omega_{s1,s2}$ the SBL angular frequencies, and ω_0 the center angular frequency of the SBL cavity mode. The SBL gain function[48] $g_{1,2}$ is defined as

$$g_{1,2} \equiv \frac{g_0}{1+\frac{2i\Delta\Omega_{1,2}}{\Gamma}} \tag{3.3}$$

$$\Delta\Omega_{1,2} \equiv \omega_{p1,p2} - \omega_{s1,s2} - \Omega_B, \tag{3.4}$$

where g_0 is the gain coefficient of SBL, Ω_B the angular frequency of the acoustic phonon, and Γ the angular bandwidth of the SBL gain. At steady state, $\dot{A}_{1,2} = \dot{\alpha}_{1,2} = 0$. Then, we get

$$i\left(\omega_{s1,s2} - \omega_0\right) - \frac{\gamma}{2} + \frac{g_0\left|A_{1,2}\right|^2}{1+\frac{4\Delta\Omega_{1,2}^2}{\Gamma^2}}\left(1 - \frac{2i\Delta\Omega_{1,2}}{\Gamma}\right) = 0 \tag{3.5}$$

Both the real parts and the imaginary parts are zero. Therefore, we get the clamping condition,

$$\frac{g_0\left|A_1\right|^2}{1+\frac{4\Delta\Omega_1^2}{\Gamma^2}} = \frac{g_0\left|A_2\right|^2}{1+\frac{4\Delta\Omega_2^2}{\Gamma^2}} = \frac{\gamma}{2}. \tag{3.6}$$

The imaginary parts become

$$\left(\omega_{s1,s2} - \omega_0\right) - \frac{\gamma\Delta\Omega_{1,2}}{\Gamma} = 0 \tag{3.7}$$

The difference between the two equations is

$$\Delta\omega_s = \frac{\gamma/\Gamma}{1+\gamma/\Gamma}\Delta\omega_p, \tag{3.8}$$

where $\Delta\omega_s \equiv \omega_{s2} - \omega_{s1}$ is the SBL beating angular frequency, and $\Delta\omega_p \equiv \omega_{p2} - \omega_{p1}$ is the pump detuning angular frequency. The dispersion from the SBL lasing process introduces a mode-pulling effect that pulls the SBLs toward to the Brillouin gain center. This effect reduces the SBL beating frequency relative to the pump detuning frequency by a mode pulling factor, $\frac{\gamma/\Gamma}{1+\gamma/\Gamma}$.

We estimate the SBL beating frequency by the mode-pulling equation 3.8 (Figure 3.3). The mode-pulling factor is a function of the resonator Q factor, and independent of the pump detuning frequency ($\Delta\nu_p \equiv \Delta\omega_p/2\pi$). If we assume the SBS gain bandwidth is 50 MHz, then the SBL beating frequency ($\Delta\nu_s \equiv \Delta\omega_s/2\pi$) is less than 100 kHz if the Q factor of the resonator is larger than 100 M. The dynamic range of the pump detuning ($\Delta\nu_{p\ \max} = \nu_p/Q$) is also a function of the Q factor and sets the upper limit of the rotation sensing.

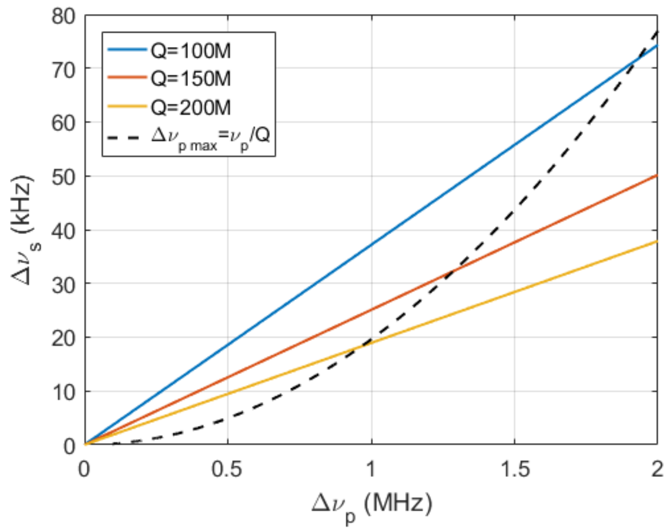

Figure 3.3: **Simulation of the mode pulling.** The SBL beating frequency is a linear function of the pump detuning frequency (color lines). Both the pulling factor (slopes of the color lines) and the dynamic range of the rotation sensing (Black dashed line) depend on the cavity linewidth. In this figure, we assume that the SBS gain bandwidth is 50 MHz, and the dynamic range of the rotation sensing is equal to the full-width-half-maximum of the cavity linewidth.

To verify the theory, we use the PDH locking to center-lock the first pump to the cavity center and sweep the frequency of the second pump to change the pump detuning. We measure the corresponding SBL beating frequency in the experiment. The wide sweeping shows the full dynamic range of the pump detuning in a 36mm disk sample ($Q \approx 130$ M, $\Gamma/2\pi \approx 30$ MHz). No beating is detected beyond this range. The data shows a nearly linear response of the mode pulling consistent with the theoretical prediction (Figure 3.4a). We further zoom in the near-zero detuning frequency region and observe the locking effect similar to the He-Ne ring laser gyroscope (Figure 3.4b). Similar results are observed among different modes, mode families and different sizes of samples. To capture the locking zone, we further consider dissipative coupling in the next section.

3.2 Dissipative coupling, Kerr nonlinearity, and Sagnac effect

In the counter-propagating SBLs, the SBL beating signal tracks the Sagnac rotation signal, and is affected by the dissipative coupling and the Kerr nonlinearty. To

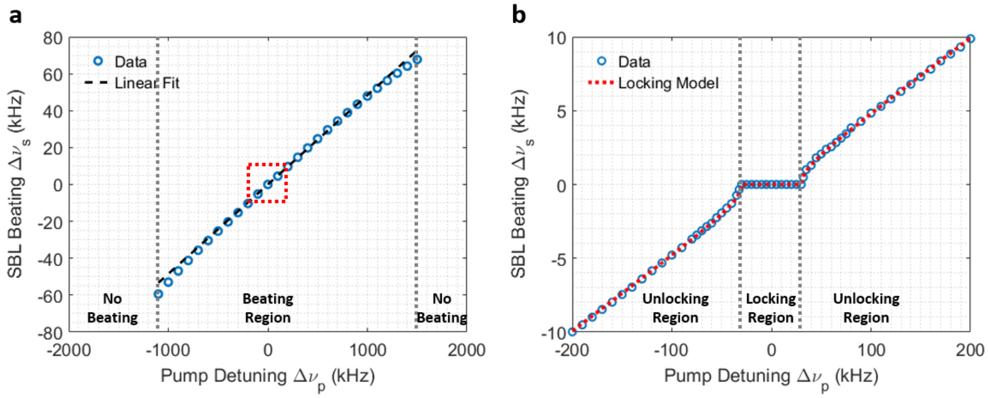

Figure 3.4: **Experiment of the mode pulling effect. a,** The full range of the SBL beating frequency versus pump detuning shows good linearity. **b,** A zoom-in of the red dotted box in part **a**. The lock region and unlock region are well-resolved. The resulting SBL beating signal is consistent with a model including the mode-pulling effect and the dissipative coupling.

capture the physics, we add these terms into Eq. (3.1)-(3.2):

$$\begin{aligned} \dot{\alpha_1} &= \left[i\left(\omega_{s1}-\omega_0-\frac{\delta_\Omega}{2}\right)-\frac{\gamma}{2}\right]\alpha_1+g_1\left|A_1\right|^2\alpha_1 \\ &\quad +\kappa\alpha_2 e^{-i(\omega_{s2}-\omega_{s1})t}+i\eta\left(\left|\alpha_1\right|^2+2\left|\alpha_2\right|^2\right)\alpha_1 \qquad (3.9)\\ \dot{\alpha_2} &= \left[i\left(\omega_{s2}-\omega_0+\frac{\delta_\Omega}{2}\right)-\frac{\gamma}{2}\right]\alpha_2+g_2\left|A_2\right|^2\alpha_2 \\ &\quad +\kappa\alpha_1 e^{-i(\omega_{s1}-\omega_{s2})t}+i\eta\left(\left|\alpha_2\right|^2+2\left|\alpha_1\right|^2\right)\alpha_2, \qquad (3.10)\end{aligned}$$

where δ_Ω captures the Sagnac passive modal shift ($2\pi D/n_g\lambda$, where D is the resonator diameter, n_g the group refractive index, λ the light wavelength), and κ captures the dissipative coupling rate. The η is defined as the nonlinear angular frequency shift per photon and can be calculated by[15]

$$\eta = \frac{n_2\hbar\omega^2 c}{n_0^2 V}, \tag{3.11}$$

where n_2 is the nonlinear refractive index, n_0 the material refractive index, V the mode volume, ω the angular frequency of light, and c the speed of light.

We use the clamping condition in Eq. (3.6), and treat the Sagnac shift, dissipative coupling, and Kerr shift as perturbations around steady-state. (In Chapter V, we will show the clamping condition is exact with the coupling.) Equations (3.9)-(3.10) become

$$i\left(\omega_{s1}-\omega_0-\frac{\delta_\Omega}{2}\right)-i\frac{\gamma\Delta\Omega_1}{\Gamma}+\kappa\frac{\alpha_2}{\alpha_1}e^{-i(\omega_{s2}-\omega_{s1})t}+i\eta\left(|\alpha_1|^2+2\,|\alpha_2|^2\right) \;=\; 0 \tag{3.12}$$

$$i\left(\omega_{s2}-\omega_0+\frac{\delta_\Omega}{2}\right)-i\frac{\gamma\Delta\Omega_2}{\Gamma}+\kappa\frac{\alpha_1}{\alpha_2}e^{-i(\omega_{s1}-\omega_{s2})t}+i\eta\left(|\alpha_2|^2+2\,|\alpha_1|^2\right) \;=\; 0. \tag{3.13}$$

We introduce the following definition:

$$q \;\equiv\; \left|\frac{\alpha_2}{\alpha_1}\right|_{t=0},\theta\equiv\theta_{s2}-\theta_{s1}\Rightarrow\frac{\alpha_2}{\alpha_1}=q\exp(i\theta) \tag{3.14}$$

$$\dot{\theta} \;=\; \frac{d}{dt}\left(\theta_{s2}-\theta_{s1}\right)=\omega_{s2}-\omega_{s1}=\Delta\omega_s. \tag{3.15}$$

where q is the amplitude ratio of the SBLs at a specific timing (constant), and $\theta_{s1,s2}$ are complex phases of the SBL fields capturing the phase and the small amplitude changes. The difference between Eq. (3.12) and Eq. (3.13) becomes an Adler equation[66],

$$\frac{d\theta}{dt}=\underbrace{\frac{1}{1+\gamma/\Gamma}\left[\frac{\gamma}{\Gamma}\Delta\omega_p-\delta_\Omega+\eta\left(|\alpha_2|^2-|\alpha_1|^2\right)\right]}_{\equiv a}-\underbrace{\frac{\kappa\left(q+\frac{1}{q}\right)}{1+\gamma/\Gamma}}_{\equiv b}\sin\theta-i\underbrace{\frac{\kappa\left(q-\frac{1}{q}\right)}{1+\gamma/\Gamma}}_{\equiv c}\cos\theta. \tag{3.16}$$

The analytical solution of $\theta(t)$ in the Adler equation is

$$\theta(t)=2\tan^{-1}\left[\frac{b+\omega_m\tan\left(\frac{1}{2}\omega_m t\right)}{a+ic}\right], \tag{3.17}$$

where $\omega_m\equiv\sqrt{a^2-b^2+c^2}$ is the fundamental beating angular frequency of the counter-propagating SBLs, such that

$$\omega_m=\frac{1}{1+\gamma/\Gamma}\sqrt{\left[\frac{\gamma}{\Gamma}\Delta\omega_p-\underbrace{\delta_\Omega}_{\text{Sagnac}}+\underbrace{\eta\left(|\alpha_2|^2-|\alpha_1|^2\right)}_{\text{Kerr}}\right]^2-\underbrace{4\kappa^2}_{\text{Coupling}}}. \tag{3.18}$$

Particularly, there is an offset frequency induced by the imbalance of the SBL powers. Specifically,

$$\delta_{\text{offset}} = \eta\left(|\alpha_2|^2 - |\alpha_1|^2\right) = \frac{\eta\Delta P_{\text{SBL}}}{\gamma_{ex}\hbar\omega}, \tag{3.19}$$

where $\Delta P_{\text{SBL}} = P_{\text{SBL2}} - P_{\text{SBL1}}$ are the output power difference of the SBLs, and γ_{ex} is the photon decay rate to the external output.

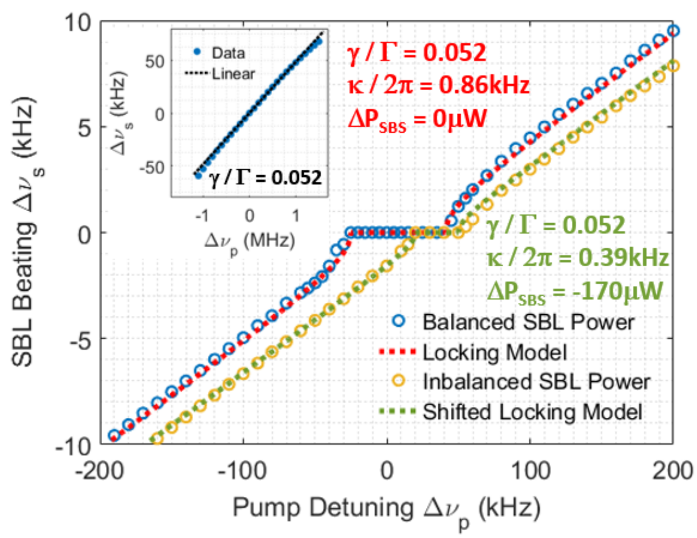

Figure 3.5: **Mode pulling, dissipative coupling, and Kerr Effect.** Red curve: Dissipative coupling locks counter-propagating SBLs when pump detuning is small. Large pump detuning unlocks the SBLs. Green curve: The imbalance of the SBL powers shifts the center of the locking zone by the Kerr nonlinearity. Nonzero SBL beating signal can exist even though the pumps are degenerate. ($\Delta P_{\text{SBL}} = -170\mu$W. The theoretical and experimental pump detuning offsets are 27kHz and 28kHz, respectively.) Inset: The full span of the SBL beating frequency versus the pump detuning. The mode-pulling response fits the linear model. The small curvature comes from the Kerr nonlinearity under different detuning.

In Figure 3.5, we center the locking zone by balancing the SBL powers. When the two SBL powers are imbalanced ($\Delta P_{\text{SBL}} \neq 0$), the Kerr effect imposes a nonlinear phase shift through self-phase-modulation and cross-phase-modulation on each SBL, and further changes the center of the locking zone. In the extreme case, the SBL beating frequency exists ($\Delta\nu_s \neq 0$) even when the pumps are degenerate ($\Delta\nu_p = 0$). In addition, changing the pump detuning modifies the pump2 power coupled into the resonator and the corresponding SBL2 power. The SBL2 power deviation causes a slight bending in the large detuning data.

Assuming $n_2 \approx 2.7 \times 10^{-20}\text{m}^2/\text{W}$, $n_0 = 1.45$, $V = 10^7\mu\text{m}^3$ (mode volume in a 36mm-diameter disk), $\lambda = 1.55\mu$m, we get $\eta/2\pi \approx 10^{-5}$Hz. If $\gamma_{ex}/2\pi = 1.5$MHz

($Q_{ex} \approx 130$M), $\gamma/\Gamma = 0.052$, then $\delta_{\text{offset}}/2\pi\Delta P_{\text{SBL}} \approx 8$Hz/$\mu$W. This value agrees with the experiment.

Please note that when $\omega_m^2 < 0$, the SBLs lock with each other, and the Sagnac rotation cannot be tracked properly. In this case, the gyroscope is in the locking zone. In contrast, when $\omega_m^2 > 0$, the instantaneous SBL beating frequency changes with time and induces high harmonic components in the beating spectrum.

3.3 High harmonic contents in the SBL beating spectrum

We examine a simplified Adler equation by assuming the power is balanced (q=1). We also assume no rotation for simplicity. The Adler equation becomes

$$\frac{d\theta}{dt} = \frac{\gamma/\Gamma}{1+\gamma/\Gamma}\Delta\omega_p - \frac{2\kappa}{1+\gamma/\Gamma}\sin\theta = a - b\sin\theta, \tag{3.20}$$

and the solution is

$$\theta(t) = 2\tan^{-1}\left[\frac{b + \omega_m \tan\left(\frac{1}{2}\omega_m t\right)}{a}\right], \tag{3.21}$$

where $\omega_m = \sqrt{a^2 - b^2}$. We can get the instantaneous beating frequency by differentiating Eq.(3.21).

$$\Delta\nu_s(t) = \frac{1}{2\pi}\frac{d\theta(t)}{dt} = \frac{\omega_m^2/2\pi}{a + \frac{b^2}{a}\cos(\omega_m t) + \frac{b\omega_m}{a}\sin(\omega_m t)} \tag{3.22}$$

To simulate the effect of the Schawlow-Townes linewidth, we add a phase noise term, $\theta_{\text{ST}}(t)$ into the phase term in Eq. (3.22). The phase noise term is simulated by the following method:

1. We generate a set of random numbers R_i by the normalized Cauchy distribution,
$$L(x) = \frac{1}{\pi\left(1 + x^2\right)}. \tag{3.23}$$
2. We calculate the accumulated phase noise by
$$\theta_{\text{ST}}(t) = \lim_{\Delta t_{\text{step}}\to 0}\sum_{i=0}^{t/\Delta t_{\text{step}}} \Delta t_{\text{step}} \times R_i \times \Delta\nu_{\text{ST}}/2. \tag{3.24}$$
3. The simulated instantaneous beating frequency becomes
$$\Delta\nu_s(t) = \frac{\omega_m^2/2\pi}{a + \frac{b^2}{a}\cos(\omega_m t + \theta_{\text{ST}}(t)) + \frac{b\omega_m}{a}\sin(\omega_m t + \theta_{\text{ST}}(t))} + \nu_n(t), \tag{3.25}$$
where $\nu_n(t)$ is the white frequency noise in the spectrum.

4. We calculate the frequency spectrum by FFT with proper amplitude normalization,

$$F_s(f) = \mathrm{FFT}\left\{\Delta\nu_s(t)\right\}. \tag{3.26}$$

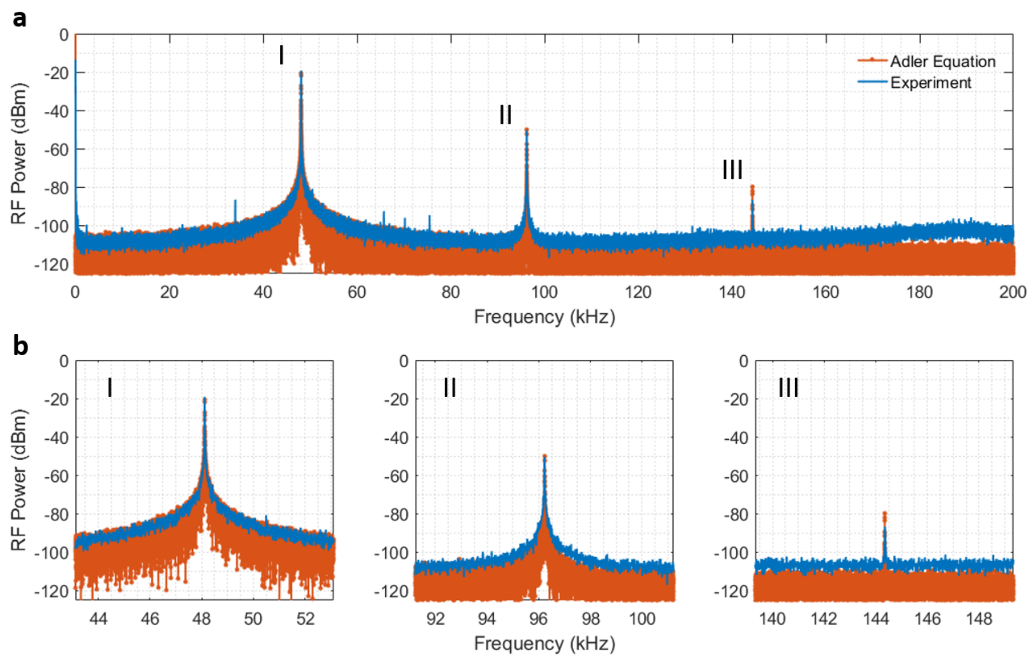

Figure 3.6: **The SBL beating baseband spectrum. a,** The spectrum simulated by the Adler equation and the experimental baseband signal. The high harmonics in the baseband comes from the high harmonics of the Adler solution. The Schawlow-Townes 3dB linewidth of the fundamental mode is 0.9 Hz. The coupling parameters ($\kappa/2\pi$ = 1.6 kHz) and the fundamental frequency ($\omega_m/2\pi$ = 48.2 kHz) are measured by the experiment. The PDH loop gain causes the small wide bump in the experimental noise level. **b,** The zoom-in of each order of harmonics. The simulated spectrum (upper envelope) agrees with the experiment.

In Figure 3.6, we compare the result between the simulation and the experiment spectrum recorded by an ESA. The Schawlow-Townes 3dB linewidth ($\Delta\nu_{\mathrm{ST}}$ = 0.9 Hz), dissipative coupling rate ($\kappa/2\pi$ = 1.6 kHz), and fundamental beating frequency (ω_m = 48.2 kHz) are measured from the experiment. Putting these parameters into the simulation, the simulated spectral components of the instantaneous beating frequency agree with the experiment. The result indicates that the high harmonic components in the baseband originate from the perturbation of the dissipative coupling near the locking zone. The Schawlow-Townes noise limits the noise level in the SBL beating spectrum.

Currently, we consider the model under fixed temperature. In reality, the room temperature and system temperature change over time so the SBL beating frequency drifts in the long term.

3.4 Frequency dithering and temperature dependency

We use frequency dithering to further investigate the drift source in the resonator. If we assume that dissipative coupling and Kerr nonlinearity are negligible, then the Eq. (3.22) becomes:

$$\begin{aligned}\Delta\nu_s &= \frac{\gamma/\Gamma}{1+\gamma/\Gamma}\Delta\nu_p - \frac{1}{1+\gamma/\Gamma}\frac{D}{n_g\lambda}\Omega &(3.27)\\ &\equiv \frac{X(T)}{1+X(T)}\Delta\nu_p - \frac{1}{1+X(T)}Y(T)\Omega, &(3.28)\end{aligned}$$

where $X(T) \equiv \gamma/\Gamma$, $Y(T) \equiv D/n_g\lambda$, $\Delta\nu_s \equiv \Delta\omega_s/2\pi$, and $\Delta\nu_p \equiv \Delta\omega_p/2\pi$. When the small rotation exists, the readout frequency at high edge ($\Delta\nu_{s+}$) and low edge ($\Delta\nu_{s-}$) from the counter is:

$$\begin{aligned}\Delta\nu_{s+} &= \left|\frac{X(T)}{1+X(T)}\Delta\nu_{p+} - \frac{1}{1+X(T)}Y(T)\Omega\right|, \quad \Delta\nu_{p+} > 0, &(3.29)\\ \Delta\nu_{s-} &= \left|\frac{X(T)}{1+X(T)}\Delta\nu_{p-} - \frac{1}{1+X(T)}Y(T)\Omega\right|, \quad \Delta\nu_{p-} < 0. &(3.30)\end{aligned}$$

If we dither the pump detuning frequency by continuously flipping the sign of the detuning, the frequency difference becomes

$$\begin{aligned}\Delta\nu_{sd} &= \Delta\nu_{s+} - \Delta\nu_{s-} = \frac{X(T)}{1+X(T)}\left(\Delta\nu_{p+} + \Delta\nu_{p-}\right) - \frac{2}{1+X(T)}Y(T)\Omega\\ &\underbrace{\approx}_{X(T)\ll 1} \underbrace{X(T)}_{\frac{dX}{dT}\approx 10^{-2}\text{–}10^{-3}}\left(\Delta\nu_{p+} + \Delta\nu_{p-}\right) - 2\underbrace{Y(T)}_{\frac{dY}{dT}\approx 10^{-5}}\Omega. &(3.31)\end{aligned}$$

This equation gives us two insights. First, the frequency shift induced by the rotation is doubled (Figure 3.7). Second, if we set the pump detuning frequencies at high edge and at low edge to be equal but with opposite signs, then the temperature dependency from the mode-pulling factor is eliminated. With the dithering, the temperature-induced drift in the readout is suppressed (Figure 3.8).

We further consider the Kerr nonlinearity:

$$\begin{aligned}\Delta\nu_s &= \frac{\gamma/\Gamma}{1+\gamma/\Gamma}\Delta\nu_p - \frac{1}{1+\gamma/\Gamma}\frac{D}{n_g\lambda}\Omega + \frac{1}{1+\gamma/\Gamma}\frac{\eta\Delta P_{\mathrm{SBL}}}{2\pi\gamma_{ex}\hbar\omega} &(3.32)\\ &\equiv \frac{X(T)}{1+X(T)}\Delta\nu_p - \frac{1}{1+X(T)}Y(T)\Omega + \frac{1}{1+X(T)}Z(T)\Delta P_{SBL}. &(3.33)\end{aligned}$$

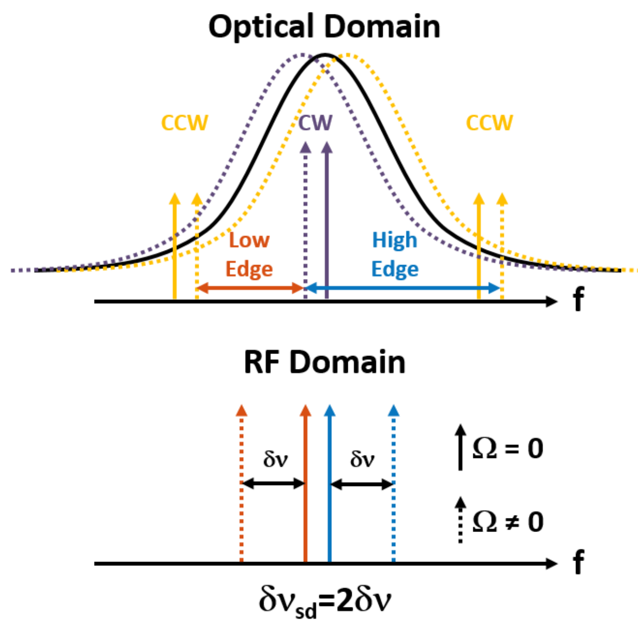

Figure 3.7: **Frequency dithering diagram.** When the sign of the pump detuning frequency (high edge: $\Delta\nu_p > 0$, low edge: $\Delta\nu_p < 0$) is modulated by a dithering frequency (f_d), the gyro readouts have opposite responses to the external rotation. By calculating the frequency difference of the SBL beating signal ($\Delta\nu_{sd} = \Delta\nu_{s+} - \Delta\nu_{s-}$), we double the sensitivity of the gyro.

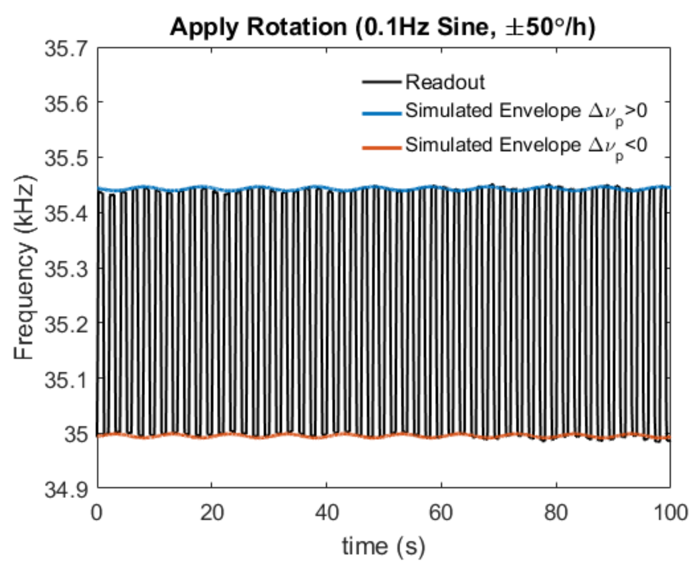

Figure 3.8: **Rotation response of frequency dithering.** In the experiment, we set $\Delta\nu_{p+} = -\Delta\nu_{p-} = 500$ kHz. The frequency difference comes from the imbalance of SBL powers. When an external sinusoidal rotation is applied (modulation frequency = 0.1 Hz, $\Omega_{\text{pk}} = 50°/\text{h}$, $f_d = 500$ mHz), the envelopes of the high and low edges capture the opposite frequency shift. The simulated envelopes from the Sagnac theory agree with the experiment.

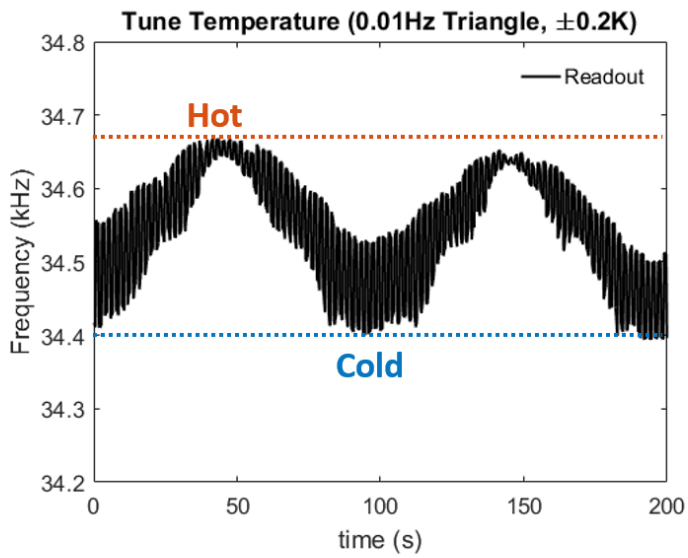

Figure 3.9: **Temperature dependency of frequency dithering.** When we applied a slow triangular modulation on the sample temperature ($\Delta T = 0.4$ K), both the difference frequency and the common frequency of the dithered signal change. The experimental value is close to the theoretical estimation. The common mode frequency drift primarily comes from the change of the pulling factor. The differential frequency drift mainly comes from the change of the SBL powers. The modal temperature drift should be controlled below 2 mK so the readout signal has sub-Hz stability.

By calculating the difference frequency ($\Delta\nu_{sd}$) and common frequency ($\Delta\nu_{sc}$) and by assuming $X(T) \ll 1$, we get:

$$\begin{aligned}
\Delta\nu_{sd} &= \Delta\nu_{s+} - \Delta\nu_{s-} \\
&\approx X(T)\left(\Delta\nu_{p+} + \Delta\nu_{p-}\right) - 2Y(T)\Omega + Z(T)\left(\Delta P_{\mathrm{SBL}+} + \Delta P_{\mathrm{SBL}-}\right) \\
&\underbrace{\approx}_{\Delta\nu_{p+}=-\Delta\nu_{p-}} -2Y(T)\Omega + Z(T)\left(\Delta P_{\mathrm{SBL}+} + \Delta P_{\mathrm{SBL}-}\right) \qquad (3.34)
\end{aligned}$$

$$\begin{aligned}
\Delta\nu_{sc} &= \left(\Delta\nu_{s+} + \Delta\nu_{s-}\right)/2 \\
&\approx X(T)\left(\Delta\nu_{p+} - \Delta\nu_{p-}\right)/2 + Z(T)\left(\Delta P_{\mathrm{SBL}+} - \Delta P_{\mathrm{SBL}-}\right)/2. \\
&\underbrace{\approx}_{\Delta P_{\mathrm{SBL}+}\approx\Delta P_{\mathrm{SBL}-}} X(T)\left(\Delta\nu_{p+} - \Delta\nu_{p-}\right)/2. \qquad (3.35)
\end{aligned}$$

Therefore, we separate the drift source by the dithering. The common frequency captures the temperature dependency of the mode-pulling factor, and the difference frequency captures the temperature dependency of the Kerr effect. In our experiment, we use FSK to generate $\Delta\nu_{p\pm} = \pm 500$ kHz. We get $d\Delta\nu_{sc}/dT = 0.5$ Hz/mK, and $d\Delta\nu_{sd}/dT = 0.3$ Hz/mK (Figure 3.9). The experiment agrees with the theory ($d\Delta\nu_{sc\ \mathrm{theory}}/dT \approx 0.5$ Hz/mK, $d\Delta\nu_{sd\ \mathrm{theory}}/dT \approx 0.2$ Hz/mK).

3.5 Backaction of the cascaded Brillouin laser

The thermal fluctuation limits the absolute frequency of the SBL lasers, such that the advantage of the ultra-narrow-linewidth is washed out. That is, the long term stability is not preserved. To minimize the temperature drift, controlling the modal temperature becomes indispensable.

Here we show a way to control the modal temperate by introducing the cascaded Brillouin backaction. The SBL absolute frequency is affected by the absorption induced dispersion. The magnitude and sign of this dispersion are sensitive to the modal temperature (Figure 3.10). By applying a small power modulation on the cascaded SBL, we create a dithered signal which serves as a sensitive indicator of the modal temperature. Then, the modal temperature of the sample is precisely controlled by an LED. This temperature feedback scheme has stability around mK level in the long term.

Below we derive the temperature dependency of the frequency shift in the power-dithered cascaded SBL. In the cavity-mode rotating frame, we write the pump, SBL, and cascaded SBL in the following form,

$$\begin{aligned}
\dot{A}_1 &= \left[i\left(\omega_p-\omega_0\right)-\frac{\gamma}{2}\right]A_1 - g_1^*\left|\alpha_1\right|^2 A_1 + \sqrt{\kappa_{ex}}S_1, && (3.36)\\
\dot{\alpha}_1 &= \left[i\left(\omega_s-\omega_1\right)-\frac{\gamma}{2}\right]\alpha_1 + g_1\left|A_1\right|^2\alpha_1 - g_2^*\left|\beta_1\right|^2\alpha_1, && (3.37)\\
\dot{\beta}_1 &= \left[i\left(\omega_c-\omega_2\right)-\frac{\gamma}{2}\right]\beta_1 + g_2\left|\alpha_1\right|^2\beta_1, && (3.38)
\end{aligned}$$

where A_1, α_1, β_1 are the normalized photon number amplitudes of the pump, SBL, cascaded SBL, respectively. The ω_p, ω_s, and ω_c are the lasing angular frequencies, and the ω_0, ω_1, ω_2 are the cavity angular frequencies. The $g_{1,2}$ are the Brillouin gains, which are defined by

$$\begin{aligned}
g_{1,2} &= \frac{g_0}{1+\frac{2i\Delta\Omega_{1,2}}{\Gamma}}, && (3.39)\\
\Delta\Omega_1 &= \omega_p-\omega_s-\Omega_1, && (3.40)\\
\Delta\Omega_2 &= \omega_s-\omega_c-\Omega_2, && (3.41)\\
\Omega_B &\equiv \Omega_1 \approx \Omega_2, && (3.42)
\end{aligned}$$

where Ω_B is the Brillouin shift, which is equal to $4\pi n c_s/\lambda_p$ (n the refractive index, c_s the speed of sound in silica, and λ_p the pump wavelength). In addition, the g_0 is the peak of the Brillouin gain, κ_{ex} is the external coupling coefficient, and S_1 is the normalized external pump photon number.

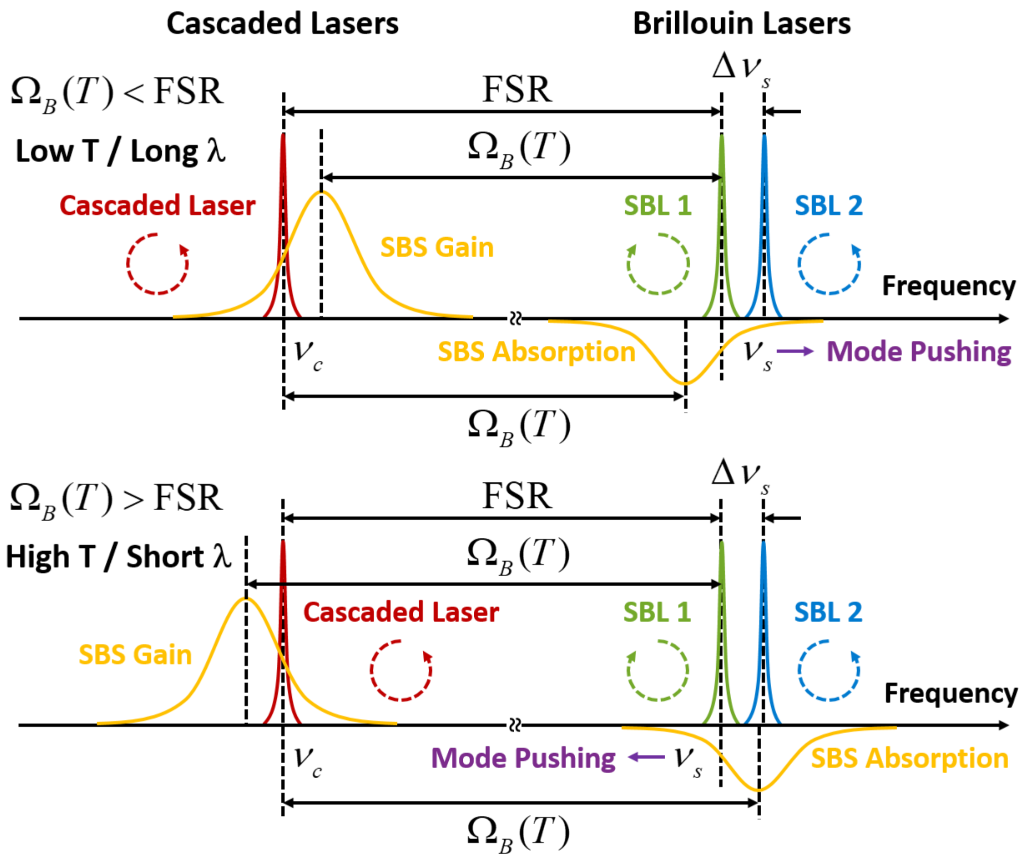

Figure 3.10: **The backaction induced by the cascaded Brillouin laser.** **a,** When the FSR is larger than the Brillouin shift (Ω_B), the cascaded laser induces a backaction on the SBL1. The backaction originates from the dispersion of the absorption (mode-pushing effect) proportional to the cascaded laser power. The beating frequency of the counter-propagating SBLs decreases when the cascaded laser power increases. **b,** When the FSR is smaller than the Brillouin shift, the mode pushing changes the SBL1 frequency to the opposite direction. The beating frequency of the counter-propagating SBLs increases when cascaded laser power increases. In both cases, the SBL2 frequency is not affected by the mode-pushing effect because the Brillouin absorption is directional. Therefore, the SBL2 becomes a reference to measure the shift of SBL1. The dual-SBL beating frequency tracks the temperature dependency of the backaction under the cascaded power dithering.

At steady-state of the cascaded lasing, if we assume the mismatch between the free spectral range and the Brillouin shift is sufficiently small ($\Delta\Omega_i \ll \Gamma$), we can simplify the equations as follows:

The real parts and imaginary parts of Eq.(3.37-3.38) are

$$g_0\left(|A_1|^2 - |\beta_1|^2\right) = g_0\,|\alpha_1|^2 = \frac{\gamma}{2}, \tag{3.43}$$

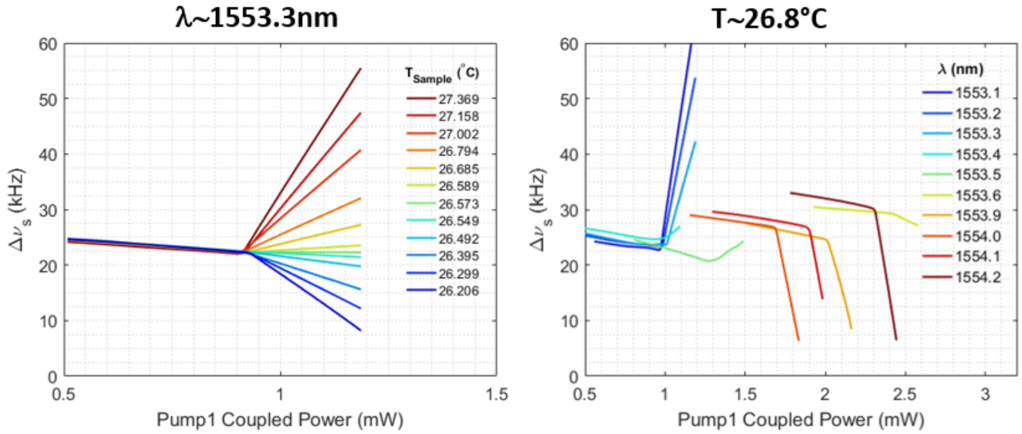

Figure 3.11: **Experiment of the cascaded Brillouin laser backaction. a,** The temperature dependency of the backaction. We fix the cavity mode and tune the sample temperature. Without the cascaded laser, the beating frequency slightly reduces when the SBL1 power increases due to the Kerr effect ($\Delta\nu_p > 0$ in this case). When the cascaded laser is generated, the absorption-induced-backaction further changes the beating frequency, which is proportional to the cascaded laser power. The magnitude and sign of the backaction depend on the temperature, so the SBL beating frequency becomes a modal temperature indicator when we fixed the pump power. ($d\Delta\nu_s/dT$ = 13 Hz/mK at 1 mW coupled pump power.) **b,** The wavelength dependency of the backaction. We fix the temperature and change the cavity mode. The backaction changes the sign and magnitude as the prediction when we sweep the wavelength. At different wavelengths, the modal interaction changes the threshold of the cascaded laser.

$$\omega_s - \omega_1 = \frac{2g_0}{\Gamma}\left(|A_1|^2 \Delta\Omega_1 + |\beta_1|^2 \Delta\Omega_2\right) \tag{3.44}$$

$$\omega_c - \omega_2 = \frac{2g_0}{\Gamma}|\alpha_1|^2 \Delta\Omega_2. \tag{3.45}$$

Using Eq.(3.43) to remove $|\alpha_1|^2$ and $|\beta_1|^2$, we get

$$\omega_s = \omega_1 + \frac{2g_0}{\Gamma}|A_1|^2 \underbrace{(\Delta\Omega_1 + \Delta\Omega_2)}_{\omega_p - \omega_c - 2\Omega_B} - \frac{\gamma}{\Gamma}\Delta\Omega_2, \tag{3.46}$$

$$\omega_c = \frac{\omega_2 + \frac{\gamma}{\Gamma}(\omega_s - \Omega_B)}{1 + \frac{\gamma}{\Gamma}}.. \tag{3.47}$$

Assuming $P = \hbar\omega_p\gamma_{ex}|A_1|^2$, and we know that ω_1, ω_2, ω_p, Ω_B are independent of power, we have,

$$\frac{d\omega_c}{dP} = \frac{\gamma/\Gamma}{1+\gamma/\Gamma}\frac{d\omega_s}{dP}, \tag{3.48}$$

$$\frac{d\omega_s}{dP} = \frac{2g_0}{\hbar\omega_p\gamma_{ex}\Gamma}\frac{\omega_p - \omega_c - 2\Omega_B}{1 + \frac{\gamma/\Gamma}{1+\gamma/\Gamma} + \frac{2g_0 P}{\hbar\omega_p\gamma_{ex}\Gamma}\frac{\gamma/\Gamma}{1+\gamma/\Gamma}}. \tag{3.49}$$

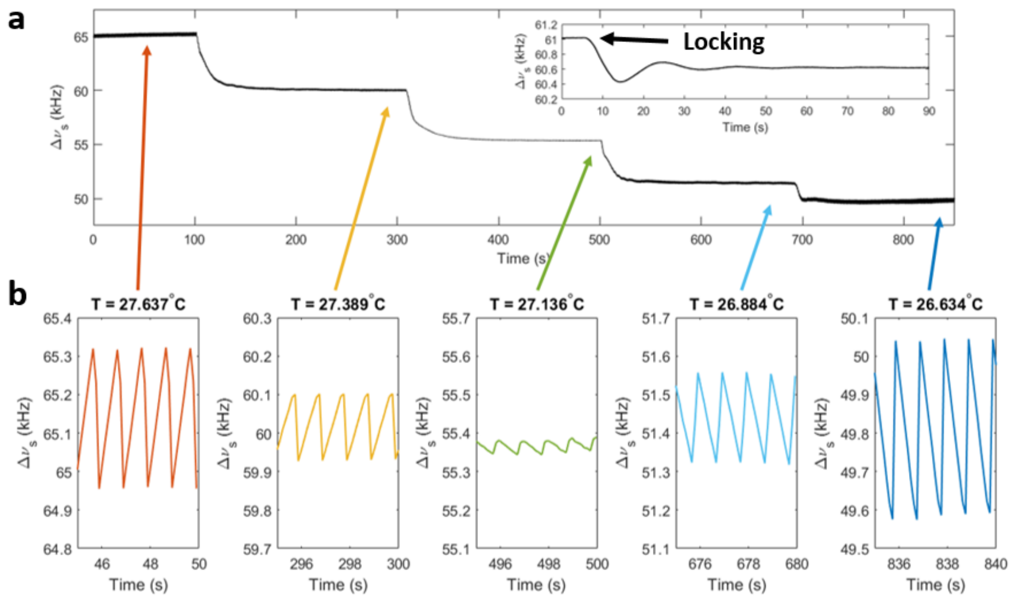

Figure 3.12: **Thermal tuning of the backaction under pump power dithering. a,** The tuning curve of the dual-SBL beating frequency under cascaded laser backaction with a small power dithering. The SBL beating frequency is sensitive to the temperature due to the existence of the backaction. **b,** The polarity and amplitude of the frequency shift depending on the temperature when a small saw-tooth signal modulates the pump power. The power dithering provides a small-signal temperature indicator for the feedback. **Inset**, the system is temperature stabilized by a 1W LED and TEC by using the dithered amplitude of the SBL beating frequency shift as a feedback signal. The long term drift is suppressed with a time constant around 10 seconds. The short term fluctuation (around second-level) becomes larger due to the slow thermal response. Fast thermal control is needed to suppress the drift below 10 seconds.

Near the threshold, we can take $2g_0 |A_1|^2 = \gamma$. Eq. (3.49) becomes

$$\frac{d\omega_s}{dP} = \frac{1}{1+\gamma/\Gamma}\frac{2g_0}{\hbar\omega_p\gamma_{ex}\Gamma}\left(\omega_p - \omega_c - 2\Omega_B\right). \tag{3.50}$$

If we consider the temperature dependency of the lasing mode near the threshold, and $\gamma/\Gamma \ll 1$, we have

$$\frac{\partial^2\omega_s}{\partial P\partial T} \approx \frac{-4g_0}{\hbar\omega_p\gamma_{ex}\Gamma}\left(\frac{d\Delta\omega_B}{dT} - \frac{d\Omega_B}{dT}\right), \tag{3.51}$$

$$\frac{d\Delta\omega_B}{dT} = \left(-\frac{1}{n}\frac{dn}{dT} - \alpha_L\right)\Delta\omega_B, \tag{3.52}$$

where $\Delta\omega_B = \omega_p - \omega_s \approx \omega_s - \omega_c \approx \omega_0 - \omega_1$. For the silica glass, $\alpha = 0.51 \times 10^{-6}/K$ and $dn/dT = 11.6 \times 10^{-6}/K$. Putting the values into the equation ($g_0/2\pi$ = 3 mHz, $\Gamma/2\pi$ = 30 MHz, $\gamma_{ex}/2\pi$ = 2 MHz, $\omega_p/2\pi$ = 193 THz, $d\Omega_B/dT = 2\pi \times 1$ MHz/K,

$d\Delta\omega_B/dT = 2\pi \times 100$ kHz/K), we get the theoretical estimation, 250 kHz/(K.mW). According to the experiment (Figure 3.11), this value is around 140kHz/(K.mW), which is deviated by a factor of 2. This deviation comes from two factors. First, the accuracy of the estimated g_0 and Ω_B is limited. Second, the conversion efficiency from the pump power to the cascaded SBL power is not ideal.

To estimate g_0 (in the unit of rad/s), we use the following equations[47]:

$$g_0 \approx \frac{\hbar\omega^3}{P_{\text{clamp}} Q_T Q_E} \tag{3.53}$$

$$\approx \frac{4\pi\Delta\nu_{\text{clamp}}}{n_T}, \tag{3.54}$$

where P_{clamp} is the clamping power of SBL without cascade, Q_T (Q_E) the total (external) quality factor, $\Delta\nu_{\text{clamp}}$ the full-width-half-maximum of the linewidth under clamping, n_T the thermal quanta of the phonon.

We further use power dithering to generate the temperature indicator (Figure 3.12). The polarity and amplitude of the indicator is resolved by a slow saw-tooth power dithering. Furthermore, the fast sinusoidal power dithering ($f_d = 200 - 500$ Hz) generates a temperature-dependent feedback signal by a locking amplifier. Using a servo to control the 1W LED and TEC, we stabilize the long term modal temperature (> 10 seconds) to several-mK level. Currently, the thermal response is slow, so the short term (second-level) fluctuation becomes larger. A fast actuator is needed to stabilize the short term thermal drift further.

3.6 Conclusion

We investigate the physics of the counter-pumped stimulated Brillouin laser (CP-SBL), and our model captures the mode-pulling effect, dissipative coupling, Kerr nonlinearity, and Sagnac shift. The resulting Adler equation recovers the high harmonic contents in the beating spectrum. In addition, we use frequency dithering to double the sensitivity of the rotation and identify the drift sources. Also, we use the backaction of the cascaded Brillouin laser to generate a temperature indicator by power dithering. By using power feedback, the long term temperature is actively stabilized. With the theoretical model developed in this section, we demonstrate the performance of Sagnac sensing by the CP-SBL gyroscope in the next chapter.

Chapter 4

COUNTER-PUMPED BRILLOUIN LASER GYROSCOPE

Counter-propagating lightwaves within a closed rotating loop experience different round-trip propagation times as a result of the Sagnac effect. This time difference can be precisely measured using optical interference. Moreover, it can be greatly increased by creating very long real or effective path lengths, as is possible using an optical fiber or optical resonators. Modern optical gyroscopes use this favorable combination of sensitive time difference measurement with low-optical-loss path length enhancement to realize accurate rotation measurement. The transfer of this powerful discrete technology to a solid state chip-based form has received considerable attention for some time. Such chip-based Sagnac gyroscopes could potentially offer high performance in an inherently rugged structure. They would also enable a more scalable manufacturing process as enjoyed by micro-electrical-mechanical gyroscopes that are used widely in consumer products. However, until quite recently, monolithic gyroscopes have been limited in performance on account of the lack of waveguide and large-scale optical resonators with a sufficiently low optical loss. The development of monolithic waveguide and resonator platforms with over a 100-fold reduction in optical loss has started to change this situation. Analogs of fiber-optic, passive-resonant and ring-laser gyroscopes in compact and often monolithic form have been reported. In this work, we report a monolithic ring laser gyroscope using counter-propagating Brillouin lasers. The device performance is explored, including measurement of the Earth's rotation rate.

Unlike an earlier chip-based Brillouin laser gyroscope which operated in cascaded mode[12], the current device operates in a near-degenerate fashion similar to commercial ring laser gyroscopes. This scheme is advantageous for signal processing and ultimate system simplicity as the readout is around audio rates as opposed to microwave X-band rates. However, in this configuration, the device also becomes susceptible to a back-scatter induced locking effect that is well known in commercial ring-laser gyroscope systems. In commercial systems, a mechanical dithering approach is used to break the locking effect. In the current work, we demonstrate a solid-state unlocking approach that relies upon the physics of the underlying

This chapter was adapted from the paper, Y.-H. Lai, et al., "Earth rotation measured by a chip-scale Brillouin laser gyroscope," arXiv preprint (2019).

Brillouin process. This unlocking approach leverages the Brillouin phase matching condition and related pulling phenomena in a new way to induce dispersion that is distinct for the clockwise and counter-clockwise Brillouin laser waves. Beyond a critical level of Brillouin-induced dispersion, the system is unlocked and gyroscope operation is possible.

4.1 Offset-counter-pumping experiment

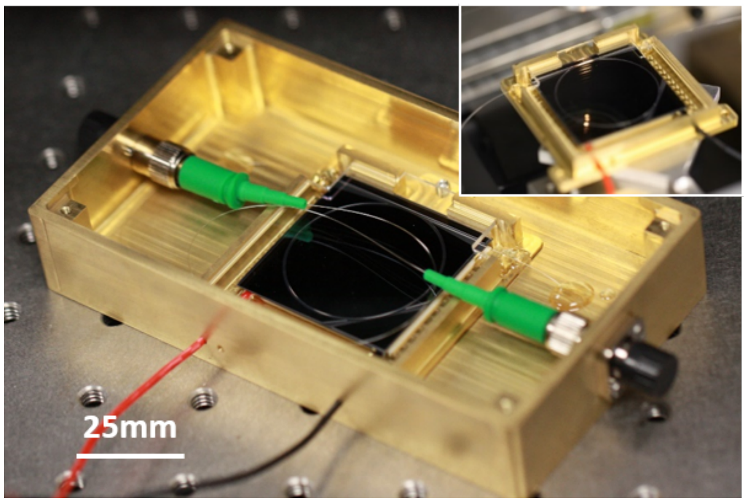

Figure 4.1: **Packaged 36mm-diameter silica resonator.** The 36mm wedge silica resonator was coupled with a polarization-maintained fiber taper waveguide and packaged in a brass package to minimize the thermal fluctuation, acoustic noise, and air flow. A TEC is attached beneath the sample so the temperature can be controlled. **Inset:** The silica resonator is attached with the fiber taper and characterized before packaging. (Photo: Yu-Hung Lai)

To make the gyroscope, we first fabricate a silica wedge resonator on a silicon chip by oxidation, lithography, HF wet-etching, and XeF_2 dry-etching[67]. Then, a phase-maintained fiber taper waveguide[59, 60, 68] is coupled with the resonator and packaged together in a brass box (Figure 4.1). The optical resonator has a loaded-quality-factor above 100 M, and the FSR is 1.808 GHz for a 36.0 mm-diameter resonator.

To counter-pump the gyroscope, we use an external-cavity diode laser (ECDL) amplified by an erbium-doped fiber amplifier (EDFA). The laser is split into two pumps and frequency shifted by acoustic-optical modulators (AOMs) independently. The first pump is phase modulated to create a Pound-Drever-Hall error signal for center-locking to the cavity mode[69]. The second pump has a pump detuning frequency ($\Delta\nu_p$) relative to the first pump. Both pumps are actively stabilized to minimize the power drift. Then, the counter-propagating pumps excite their own corresponding SBLs in the resonator. The SBLs recombined on a photodetector (PD) to generate an SBL beating frequency ($\Delta\nu_s$) at audio frequency. In addition, the copropagating pump and SBL beat on a high-speed PD to generate pump-SBL beating at microwave frequency. The readout signals are recorded by an electrical spectrum analyzer (ESA) or by a frequency counter (FC). Sometimes an additional optical spectrum analyzer (OSA) is added in the optical line to resolve the pump powers and SBL powers. The whole modulation system is enclosed within a shielded environmental chamber to passively suppress the temperature drift (Figure 4.2).

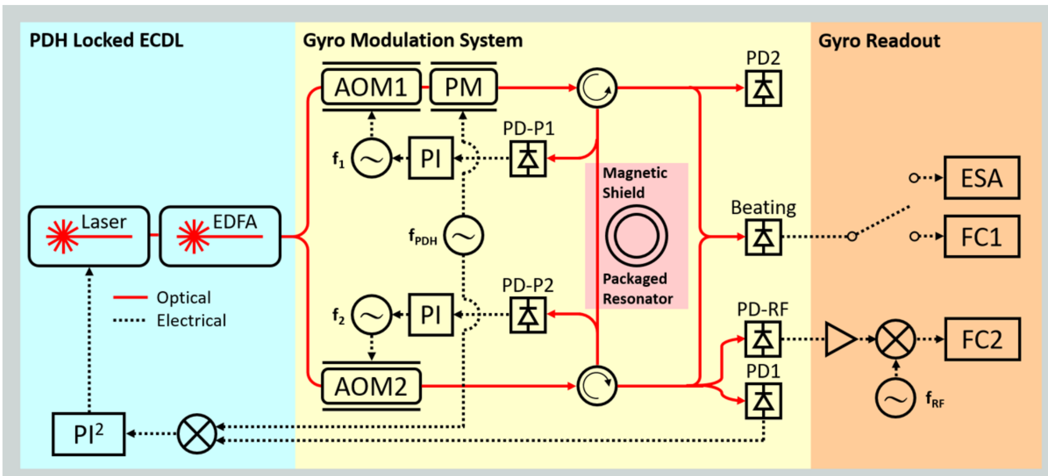

Figure 4.2: **Offset-counter-pumped SBL gyro system.** The ECDL amplified by the EDFA is PDH-locked to the microcavity. The independent AOMs control the pump detuning frequency, and actively stabilize both pump powers. The gyroscope package is enclosed in a high-permeability magnetic shield to remove potential magneto-optical Faraday-effect induced nonreciprocity[70, 71]. The whole gyro modulation system is enclosed in an environmental chamber to minimize the temperature drift. The readout signals are monitored by PDs, and examined by the FC and ESA. PM: phase modulator, PI: proportional-integral servo, RF: radio frequency.

The full model of the SBL beating frequency under rotation is

$$\Delta\nu_s = \frac{1}{1+\gamma/\Gamma}\sqrt{\left[\frac{\gamma}{\Gamma}\Delta\nu_p - \frac{D\Omega}{n_g\lambda} + \frac{\eta\Delta P_{\mathrm{SBL}}\lambda}{2\pi\gamma_{ex}hc}\right]^2 - 4\left(\frac{\kappa}{2\pi}\right)^2}, \tag{4.1}$$

where $\Delta\nu_s$ is the fundamental SBL beating frequency, $\Delta\nu_p$ the pump detuning frequency, $\gamma/2\pi$ the cavity linewidth, $\Gamma/2\pi$ the SBS gain bandwidth, $\eta/2\pi$ the nonlinear frequency shift per photon, $\gamma_{ex}/2\pi$ the photon decay rate to the output, and $\kappa/2\pi$ the dissipative coupling rate. All units are in Hertz. In addition, D is the disk diameter, n_g is the passive modal group refractive index, λ is the SBL wavelength, Ω is the rotation angular velocity, ΔP_{SBL} is the output SBL power difference measured by OSA, h is the Planck's constant, and c is the speed of light.

4.2 Sinusoidal rotation measurement

To demonstrate the capability of the gyroscope, we operate the gyro far away from the locking zone ($\Delta\nu_p\gamma/\Gamma \gg \kappa/2\pi$) to minimize the interaction from the dissipative coupling. We also balance the SBL powers by centering the locking zone ($\Delta P_{\text{SBL}} \to 0$). When we apply a small sinusoidal rotation to the gyroscope, the gyro readout becomes

$$\Delta\nu_s \approx \frac{1}{1+\gamma/\Gamma}\left(\frac{\gamma}{\Gamma}\Delta\nu_p - \frac{D\Omega}{n_g\lambda}\right). \tag{4.2}$$

The Sagnac factor is calculated by

$$S \equiv \left|\frac{d\Delta\nu_s}{d\Omega}\right| = \frac{1}{1+\gamma/\Gamma}\frac{D}{n_g\lambda}. \tag{4.3}$$

The Sagnac factor of the counter-pumped Brillouin laser gyroscope is similar to its passive counterpart, resonator micro-optical gyroscope (RMOG), but has an additional mode-pulling correction term, $1/(1+\gamma/\Gamma)$.

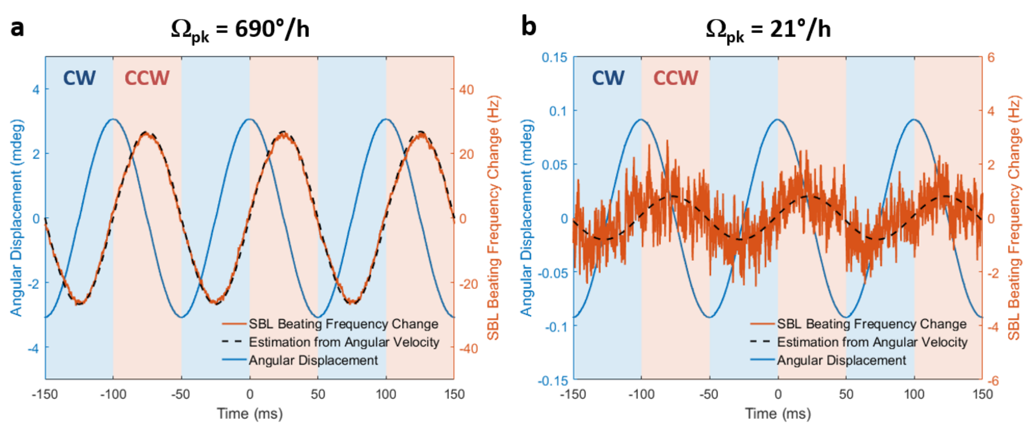

Figure 4.3: **Sinusoidal rotation response of an 18mm gyro.** We use a piezo-electric stage to apply 10 Hz sinusoidal angular modulation on the gyro package. The rotation amplitudes are 690°/h and 21°/h, respectively. There is a 90° phase shift between the angular displacement (blue trace) and the gyro readout, which tracks the angular velocity (red trace). The experiment agrees with the corrected Sagnac theory (black dashed curve) in Eq. (4.3). The traces are averaged by 240 seconds.

In the experiment, we fix one end of the gyro package at a pivot point and put the other end on a PZT stage. Then, we apply a small sinusoidal rotation displacement on the gyro package and check the gyro readout simultaneously. Both the rotation vector and the gyro surface vector are parallel, so the external rotation is fully coupled to the gyroscope.

We first verify the gyro readout signal from the time domain. We use a voltage-controlled oscillator (VCO) to track the frequency readout and use the oscilloscope to measure the SBL beating frequency change in an 18mm gyro (Figure 4.3). The gyro tracks the angular velocity so there is a 90° phase shift between the angular displacement and the gyro readout. The frequency shift agrees with the prediction calculated in Eq. (4.2).

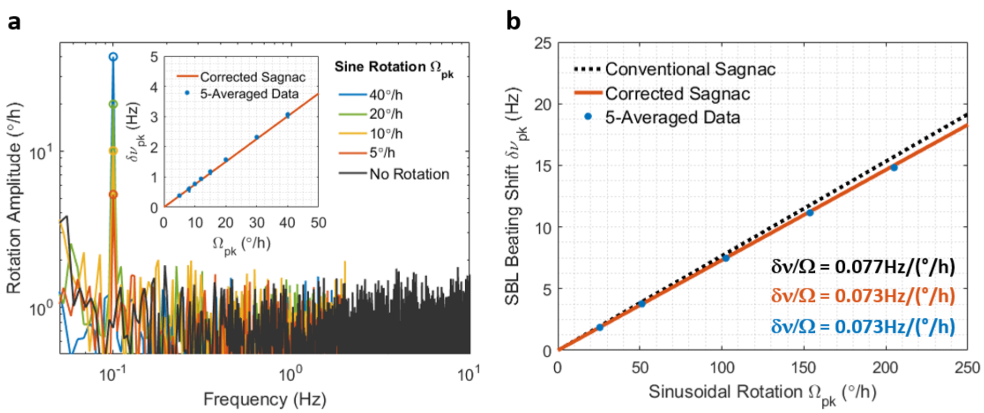

Figure 4.4: **Sensitivity and Sagnac factor of a 36mm gyro. a,** The fast-Fourier-transform (FFT) spectrum of the gyro readouts after 200 seconds of measurements. The sinusoidal rotation amplitude is clearly captured by the modulation peak at 100 mHz. The circles indicate the peak position. The white noise level spans from 0.08 to 10 Hz. Inset: The amplitude of the frequency shift to the external sinusoidal rotation. Red line: the corrected Sagnac factor predicted by the theory. Blue dots: the 5-measurement average. The error bars capture the standard deviations. **b,** The quantitative verification of the Sagnac correction factor. The mode-pulling effect in the SBL process induces a small dispersion such that the Sagnac factor in an active resonator (red line and blue dots) is smaller than the Sagnac factor in a passive resonator (black dotted line). The pump detuning frequency $\Delta\nu_p = 1$ MHz is much larger than the dissipative coupling rate, so the coupling effect is negligible. The rotation modulation frequency is 500.0mHz. The error bar is smaller than the dot size.

Next, we check the sensitivity limit of the gyro from the frequency domain. We apply 100 mHz pure sinusoidal rotation on a 36mm gyro and record the data by the frequency counter. The gyro signal is resolved from the fast-Fourier transform (FFT) spectrum. The spectra with peak rotation rate from 5 to 40°/h are captured (Figure 4.4a). The reference signal also shows a white noise level from 0.08 to 10Hz. The relation between the applied rotation amplitude and the peak frequency shift of the gyro readout agrees with our model.

Last, we verified the existence of the mode-pulling correction factor in the Sagnac factor in Eq. (4.3). We applied a large sinusoidal rotation to measure the Sagnac factor against the theories (Figure 4.4b). In the experiment, the corrected Sagnac factor in an active SBL gyro is smaller than the conventional Sagnac factor of a passive RMOG gyro by an additional mode-pulling correction factor. The mode-pulling correction factor can be viewed as the dispersion contribution from the SBS gain to the passive modal group refractive index. According to Eq. (4.3), the estimated passive modal refractive index $n_g = 1.47 \pm 0.01$, which is consistent with the value calculated from the cold-cavity FSR, $n_{g(\mathrm{FSR})} = 1.466 \pm 0.004$.

Both the Sagnac factors of the SBL gyro and the RMOG gyro preserve a group refractive index term. This group refractive index term, however, is not present in an interferometric optical gyroscope.

4.3 Schawlow-Townes linewidth, size effect, and drift reduction

In this section, we check the performance of the counter-pumped SBL gyroscope.

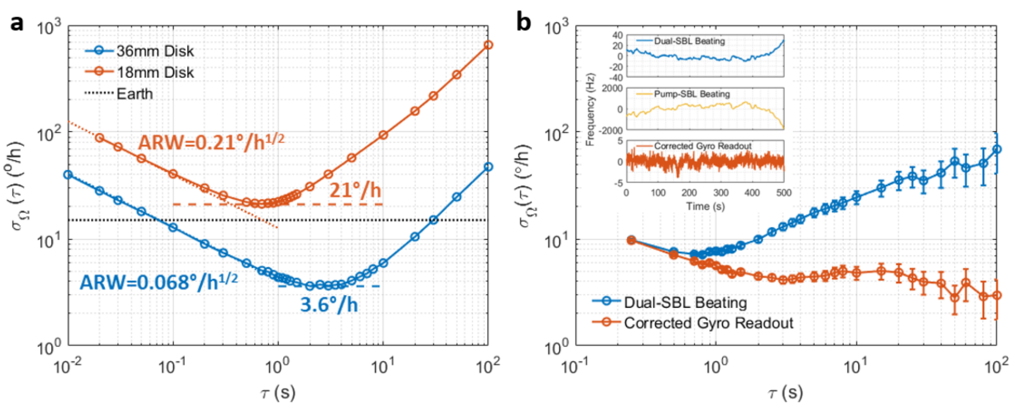

Figure 4.5: **Size effect and drift compensation. a,** Allan deviations of 18mm- and 36mm-gyroscope. Doubling the size of the gyroscope has a three-fold improvement: first, the minimal Schawlow-Townes linewidth is reduced; second, the Sagnac factor doubles; third, the bias drift is suppressed due to the larger mode volume. The overall performance of the gyroscope is boosted by at least 5×. ARW: angular random walk. **b,** In the 36mm-diameter gyroscope, we calculate the Allan deviations of the SBL beating frequency and the corrected gyro readout. The corrected gyro readout is post-processed by removing the pump-SBL beating correlated part from the SBL beating frequency. Since the pump-SBL beating tracks the modal temperature of the SBL modes, the long term drift is suppressed after the compensation algorithm. The error bars show the standard deviation. Inset: the frequency drift traces in the time domain.

Schawlow-Townes linewidth

In a 36mm-diameter gyroscope, the saturated SBL beating linewidth is less than a Hertz. The narrow linewidth is caused by two reasons. First, the intrinsic SBL linewidth is Schawlow-Townes noise limited[48]

$$\Delta\nu_{ST} = \frac{\hbar\omega^3}{4\pi P_{\mathrm{SBL}} Q_T Q_E}(n_T + N_T + 1) \tag{4.4}$$

where the $\Delta\nu_{ST}$ is the Schawlow-Townes linewidth of the SBL, n_T the thermal quanta of phonons, N_T the thermal quanta of SBL photons, ω the angular frequency of the SBL, P_{SBL} the SBL power, Q_T and Q_E the total and external Q factors. If we assume the laser wavelength is 1.55μm, $P_{\mathrm{SBL}} = 1$ mW, $Q_T \approx Q_E \approx 130$ M, and the resonator is at room temperature ($T = 300$ K, $n_T = 578$, $N_T \ll 1$), then $\Delta\nu_{ST} = 0.5$ Hz. Second, the counter-propagating SBLs circulate in the same cavity mode, so most of the common noise is canceled by the beating process. The common drift from the external fluctuations is suppressed, so the bias drift of the gyro readout is low.

Size effect

We characterize the gyro performance by calculating the Allan deviation of the gyro readout. The Allan deviation is calculated by

$$\sigma_\nu(\tau) \equiv \sqrt{\frac{1}{2(M-1)}\sum_{i=1}^{M-1}(\nu_{i+1}-\nu_i)^2} \equiv S \times \sigma_\Omega(\tau), \tag{4.5}$$

where ν_i is the measured frequency at each timestamp, τ the gate time, and M the number of sampling points subject to τ, and S the Sagnac factor. The error bars show the standard deviations of the measured Allan deviations at corresponding gate time.

We check the performance of the 18mm and 36mm gyro (Figure 4.5a). The left part of the traces has a slope equal to $-1/2$. This part is the angular random walk (ARW) dominant region, and the gyro readout is improved by longer averaging time. The center part of the traces has a slope equal to 0. The value of the lowest point is called bias drift, which is the limit of achievable sensitivity by averaging. The right part of the traces has a slope equal to 1. The slope is called ramp coefficient, which is dominated by the linear thermal drift. In this region, the long averaging diverges. Suppressing the drift source in the system is the key to improve the gyro performance.

Furthermore, doubling the size of the gyro enables an overall improvement of the performance. This improvement is caused by three reasons. First, the saturated Schawlow-Townes linewidth (before cascaded lasing) is narrower in a larger gyro, so the frequency sensitivity is enhanced. Second, doubling the physical dimension doubles the Sagnac factor. Third, other drift sources (e.g. power and temperature) are suppressed because the mode volume is larger. The 36mm gyro has ARW at $0.068°/\sqrt{\mathrm{h}}$ and the bias drift at $3.6°/\mathrm{h}$.

Drift reduction algorithm

To further suppress the drift, we use pump-SBL beating frequency to track the drift of the SBL modal temperature and removes the correlated components from the dual-SBL beating frequency by post-processing. The correlation removal algorithm calculates the corrected gyro readout by the following process:

1. Both the linear frequency drift and mean frequency in the dual-SBL beating and pump-SBL beating are removed (blue and yellow traces in the inset of Figure 4.5b).

2. The algorithm calculates the correlation factor between the dual-SBL beating and pump-SBL beating from the time domain trace.

3. The correlation part of the pump-SBL beating is removed from the dual-SBL beating by minimizing the standard deviation of the gyro readout signal (red trace in the inset of Figure 4.5b).

We confirm that the rotation signal only presents in the dual-SBL beating and doesn't exist in the pump-SBL beating by monitoring the traces with an external sinusoidal rotation $\Omega_{\mathrm{pk}} > 800°/\mathrm{h}$. Therefore, this method fully preserves the original rotation signal and suppresses the long-term drift. After post-processing, the Allan deviation becomes flat beyond 100 seconds (Figure 4.5b).

As an aside, the temperature and the Kerr nonlinearity-induced drift are both observed in the gyro readout. The temperature drift is suppressed by the passive insulation. The Kerr nonlinearity induced drift is minimized by actively stabilizing both pump powers, and by centering the locking zone to balance the SBL powers.

4.4 Earth's rotation measurement

Figure 4.6 shows the conceptual illustration of the Earth's rotation measurement by a resonator laser gyroscope. When the gyroscope is toward North and South, the effective cavity round-trips seen by the clockwise (CW) and counterclockwise (CCW) lights are different due to the Earth rotation. This round-trip difference

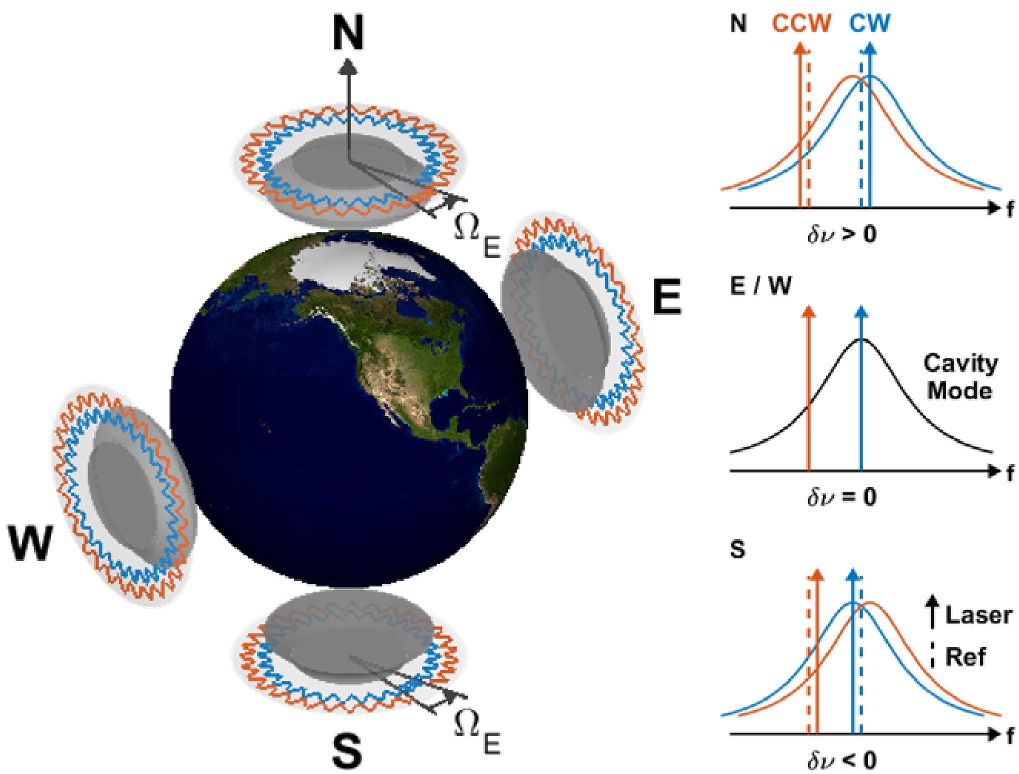

Figure 4.6: **The Earth's rotation measured by the resonator laser gyroscope.** The Earth's rotation is detected from the laser beating frequency change ($\delta\nu$) when the gyroscope is switching back and forth between North and South. There is no Earth rotation induced Sagnac shift if the gyroscope is toward East and West. Solid curve: cavity mode. Solid arrow: laser mode with Sagnac shift. Dashed line: laser mode without rotation. CW: clockwise. CCW: counterclockwise.

causes the frequency splitting of the passive cavity modes, and the corresponding laser frequencies are shifted accordingly. When the counter-propagating lasers have an offset, both the magnitude and direction of the rotation are resolved by tracking the beating frequency change, $\delta\nu$. In contrast, no rotation couples into the gyroscope toward East and West, so the beating frequency change is zero.

Measuring the Earth's rotation is a milestone for gyroscope development, not only because the measurement proves the sensitivity of the gyroscope, but also because the system drift is suppressed to a certain level such that the gyro shows the potential for a field test and North-finding. In our experiment, the full gyro system is installed on top of an automated air-bearing rotation stage (Figure 4.7). The rotation stage is installed firmly with a vibration absorbing pad on the ground to minimize the vibration noise and rotates freely on the horizontal surface. The gyro surface is vertically aligned (tilt angle $< 0.1^\circ$) to minimize the stage rotation induced signal.

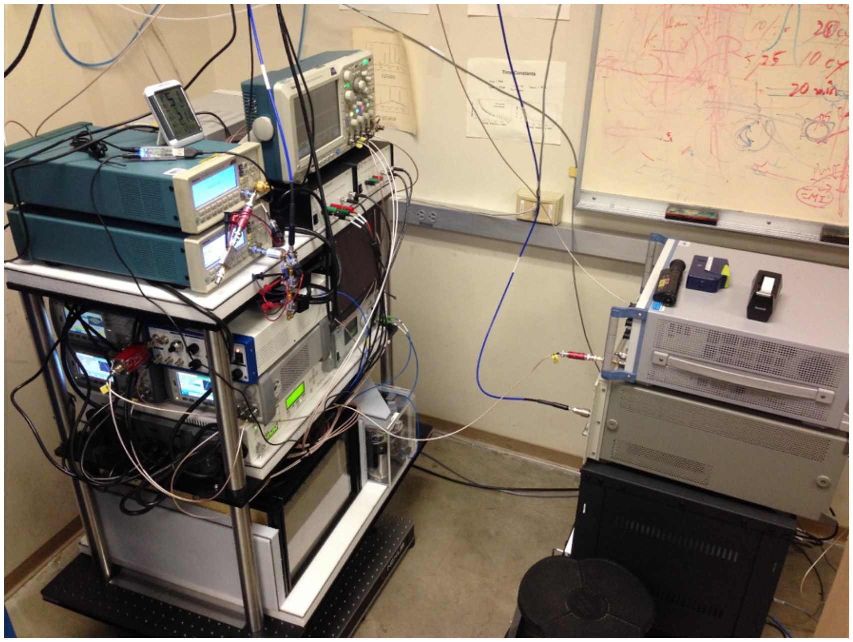

Figure 4.7: **Full rotation system.** To measure the Earth's rotation, we install the full system on an automatic air-bearing stage. The packaged gyro is installed in a damped and shielded environmental chamber. The gyro axis is well-aligned so the coupling from the stage rotation is minimized. Also, the whole system is well-balanced to minimize wobbling. During measurement, the stage rotates toward specified directions and then stabilizes until the next cycle begins. We retrieve the stabilized data for analysis. (Photo: Yu-Hung Lai)

The system is balanced to minimize wobbling during rotation. The gyro orientation is flipped by 180° every 60 seconds. In the first 15 seconds, the full system rotates. In the following of 45 seconds, the system stops moving and is stabilized. We retrieve 30 seconds of data from each stabilized session, and run the drift reduction algorithm for the overall trace. Then, the shifts of the gyro readout at different orientations are measured.

When the orientation of the gyroscope changes from North to South locally, the gyro axis and Earth axis have an angle equal to the latitude (34.1° at Caltech). The frequency shifts are normalized into the measured Earth rotation rates with latitude correction. Furthermore, we switch the sign of the detuning, such that the polarity of the frequency shifts reverses according to our model. We compare the North-South data and East-West data to check the validity of the measurement. Each data set is measured in a single trace without interruption.

The results show the opposite polarity in the North-South measurement, and the near zero response in the East-West measurement (Figure 4.8). According to the rate change measured in the experiment, the averaged Earth's rotation vector is

$15 \pm 10°/h$ toward true North, which is consistent with the prediction. The current precision is limited by the sensitivity and drift of the gyroscope. This is the first time in history that the Earth's rotation is measured by a chip-based optical gyroscope.

4.5 Conclusion

We measure the Earth's rotation by flipping a chip-based microresonator Brillouin laser gyroscope between North and South. The sensitivity and bias drift of the gyroscope are sufficiently low such that the rotation below Earth's rate is resolved. In the future, suppressing the cascaded lasing to reduce the Schawlow-Townes linewidth may further improve the sensitivity of the gyroscope. Actively stabilizing the modal temperature may further reduce the thermal drift. This gyroscope paves the way towards an all-optical inertial guidance system that is both rugged and whose manufacturing process is scalable.

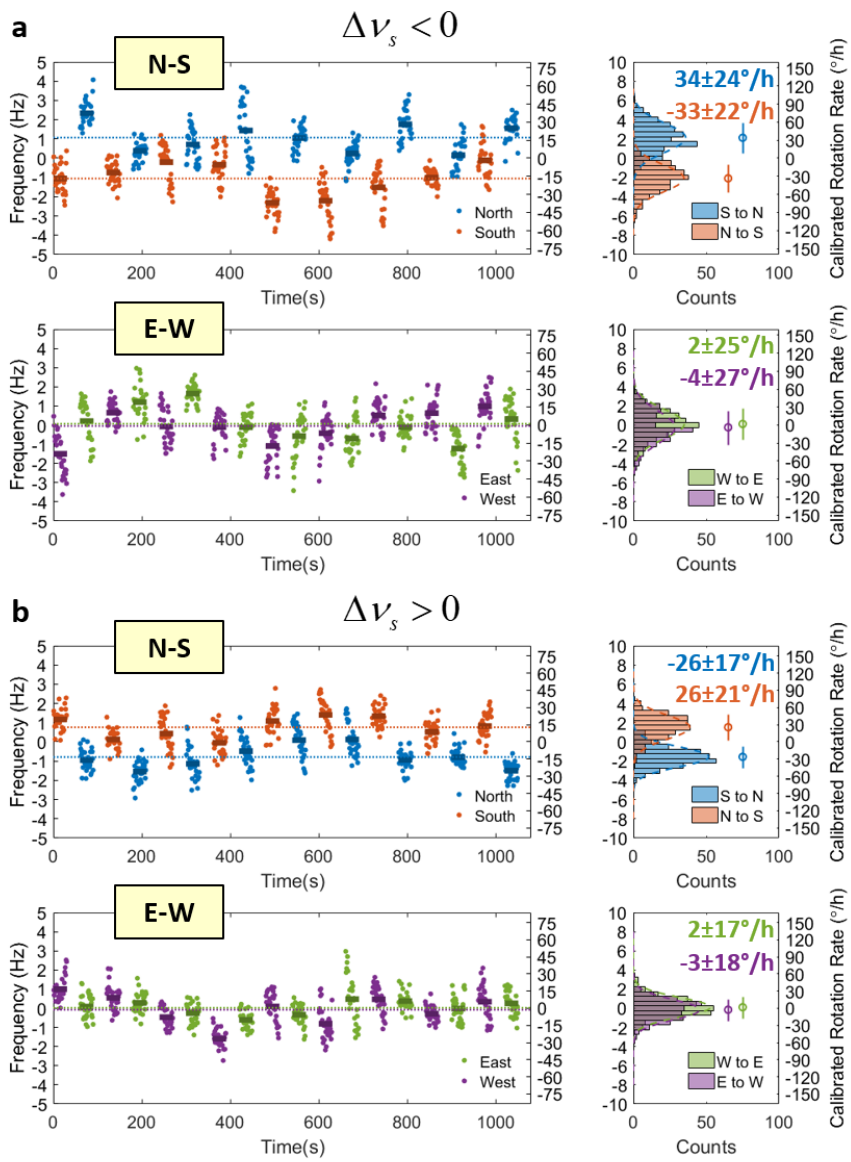

Figure 4.8: **The Earth's rotation measurements.** **a,** The North-South measurement (top) and the East-West measurement (bottom) with negative pump detuning ($\Delta\nu_p, \Delta\nu_s < 0$). The Earth rotation is captured in the North-South measurement, while the East-West measurement has near zero response. Both measurements have similar residual long term drift. **b,** The Earth measurement with positive pump detuning ($\Delta\nu_p, \Delta\nu_s > 0$). Switching the relative frequency of the CW and CCW lights changes the sign of the Sagnac shift as predicted. (Dots/Thick lines/Dotted line: the 1s-averages/30s-averages/full-average of the gyro readout in each direction. The left axis shows the gyro readout in the frequency shift. The right axis is the rotation velocity normalized by the latitude correction and the corrected Sagnac factor.) **Left Panels:** The statistics of frequency changes of switching the gyro orientation. Each count is calculated by the 1s-average frequency change between consecutive cycles. (Bars: the histogram of frequency change of 1s-averages. Dashed curve: the Gaussian envelope. The error bar shows the standard deviation.)

Chapter 5

EXCEPTIONAL POINT ENHANCED SAGNAC EFFECT

Exceptional points (EPs) are special spectral degeneracies of non-Hermitian Hamiltonians governing the dynamics of open systems. At the EP, two or more eigenvalues and the corresponding eigenstates coalesce [72–74]. Here we introduce a physical system for the study of non-Hermitian physics and nonlinear optics with precise control. Because this system dissipatively couples counter-propagating lightwaves in a single high-optical-Q resonator, it also functions as a sensitive gyroscope for measurement of rotations. As a result, our system is used to test the recent prediction of the EP-enhanced Sagnac effect [75, 76]. We are able to observe a Sagnac scale factor boost by over 4× by measuring the rotations applied to the resonator. Moreover, the amount of boost can be controlled by adjustment of system bias relative to the EP, and modeling confirms the measured enhancement. Besides verifying EP physics in a new system and application area, this work has practical importance for enhancement of optical gyroscope performance.

5.1 Introduction of exceptional point

The use of optical microresonators as sensors is being studied across a wide range of applications including biomolecule [77–79] and nanoparticle detection [80], temperature measurement [81], and rotation measurement [12, 13, 15–17]. A new approach to enhance their sensitivity uses the physics of exceptional points [75, 76, 82, 82–86]. Traditionally, a perturbation to an optical microresonator (or to its reference frame as in the case of a gyroscope) introduces a linewidth change, a frequency shift, or a resonance frequency splitting that monotonically changes with the strength of the perturbation. However, exceptional points alter this situation by introducing of a square-root dependence into the Sagnac scale factor that can boost the sensor response [82].

In this work, we experimentally and theoretically demonstrate the existence of EPs in a microresonator system controlled and probed using the Brillouin process [28]. As shown in Figure 5.1a, state vectors of the system are clockwise and counter-clockwise lightwaves, and phase matching of two independently tuned pump waves

This chapter was adapted from the paper, Y.-H. Lai, et al., “Enhanced sensitivity operation of an optical gyroscope near an exceptional point,” arXiv:1901.08217 (2019).

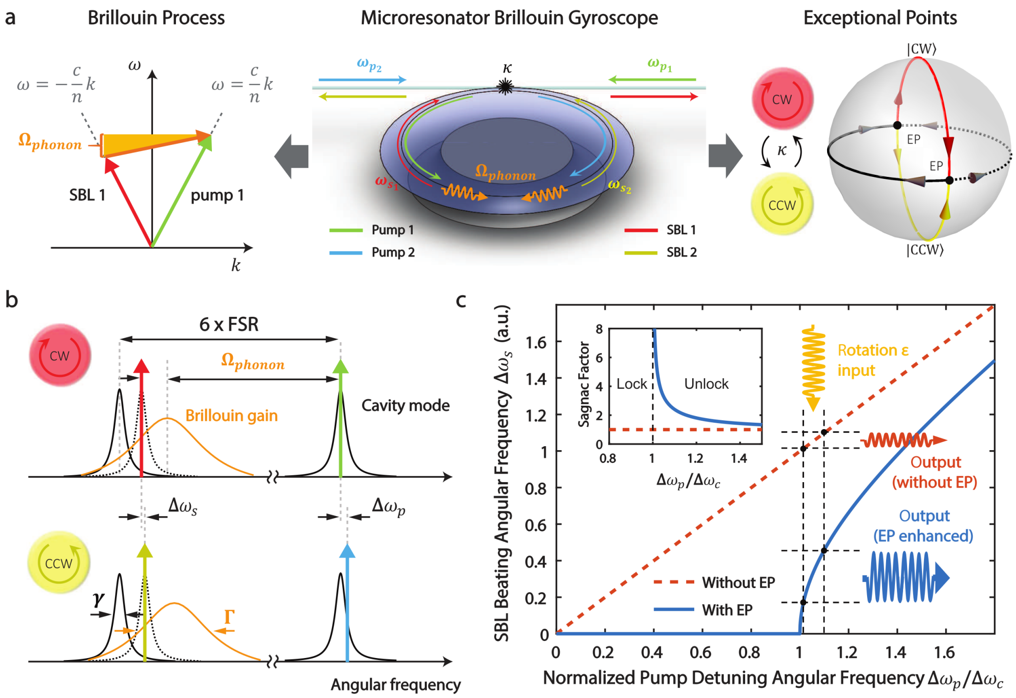

Figure 5.1: **Brillouin control of state vectors in a non Hermitian system. a,** The dual-stimulated Brillouin laser process in a microresonator. Center: The green (blue) solid curve represents pump 1 (pump 2) with angular frequency ω_{p_1} (ω_{p_2}) and the red (yellow) solid curve represents SBL 1 (SBL 2) with angular frequency ω_{s_1} (ω_{s_2}). The orange wavy line represents the acoustic phonons with angular frequency Ω_{phonon}. Left: The Brillouin energy and the momentum conservation constraints (phase matching) are illustrated for the scattering of a pump wave into a Stokes wave. Right: CW and CCW modes experience dissipative coupling at rate κ. This coupling creates eigenmodes that map to a Bloch sphere containing dual EPs (black dots). The trajectories on the Bloch sphere show the evolution of two eigenmodes (red for SBL1 and yellow for SBL2) under Brillouin control when the pump detuning decreases from $+\infty$ to $-\infty$. The low-loss and high-loss eigenmodes inside the locking zone are plotted in solid and dashed black curves, respectively. **b,** Efficient laser action requires that each Stokes mode (black with linewidth γ and separated from the pump by a multiple of the cavity FSR) lies within the Brillouin gain band (orange with linewidth Γ) which, through the phase matching condition, is shifted relative to the pump by $\Omega_{\text{phonon}} = 4\pi n c_s/\lambda_p$ (refractive index n, speed of sound in silica c_s and pump wavelength λ_p). In this work, the FSR is ~1.8 GHz so that 6×FSR approximately matched the Brillouin shift. Dispersion from the Brillouin gain pulls the Stokes lasing modes by different amounts towards the gain center on account of the difference $\Delta\omega_p$ in pump angular frequencies. **c,** The blue solid curve (red dashed curve) shows the dependence of the dual-SBL beating angular frequency $\Delta\omega_s$ versus the normalized pump detuning frequency $\Delta\omega_p/\Delta\omega_c$ for $\kappa \neq 0$ ($\kappa = 0$) as per Eq. 5.4. The yellow wavy arrow represents the input rotation signal, while the blue solid and red dotted wavy arrows represent the output signal with and without EP, respectively. The inset shows the $\kappa \neq 0$ Sagnac factor normalized to the $\kappa = 0$ Sagnac factor, indicating the enhancement near the EP.

to these waves allows for separate control of their optical gain and dispersion for precise manipulation of system state on the Bloch sphere. Moreover, the phase-matching condition allows this control of the two state vectors to occur within a single resonator. Brillouin scattering causes a pump photon with frequency ω_{p_j} to scatter from a co-propagating acoustic phonon with frequency Ω_{phonon} into a backward-propagating Stokes photon with frequency ω_{s_j}. In the context of a resonator (and as illustrated in Figure 5.1b), the associated phase matching condition requires that the Brillouin shift frequency (Ω_{phonon}) is close in value to a multiple of the resonator free-spectral-range (FSR). This phase matching condition is readily achieved by microfabrication control of resonator diameter and in effect locates a resonator mode (the Stokes mode) within the Brillouin gain spectrum for efficient stimulated Brillouin laser (SBL) action [48, 67]. Counter-pumping is performed on the same resonant mode number (m) so that laser action on two counter-propagating Stokes waves also occurs on one mode number (set to m-6 in this measurement).

To better reveal the non-Hermitian physics of this system, consider the equation of motion which reads $id\Psi/dt = H_0\Psi$ where $\Psi = (\alpha_1, \alpha_2)^T$ is the column vector for the two laser modes and H_0 is the non-Hermitian Hamiltonian governing the time evolution:

$$H_0 = \begin{pmatrix} \omega_0 + i\left(g_1|A_1|^2 - \gamma/2\right) & i\kappa \\ i\kappa & \omega_0 + i\left(g_2|A_2|^2 - \gamma/2\right) \end{pmatrix} \tag{5.1}$$

In this expression, α_1 (A_1) and α_2 (A_2) represent the photon-number-normalized amplitudes of the CW and CCW SBL (pump) modes, respectively. ω_0 is the unpumped frequency of the Stokes' cavity mode, and γ is the cavity damping rate. $g_j = g_0/(1 + 2i\Delta\Omega_j/\Gamma)$ ($j = 1, 2$) represents the Brillouin gain factor where g_0 is the gain coefficient, Γ is the gain bandwidth, and $\Delta\Omega_j = \omega_{p_j} - \omega_s - \Omega_{\text{phonon}}$ is the frequency mismatch with ω_s the Stokes frequency, ω_{p_j} ($j = 1, 2$) the pump frequency, and Ω_{phonon} the Brillouin shift [48]. The real part of the Brillouin gain factor leads to amplification of the Stokes mode, while the imaginary part is responsible for the mode-pulling effect. κ is the dissipative coupling rate between two SBL modes.

In the absence of backscattering ($\kappa = 0$), the CW and CCW SBL processes are independent because the Brillouin gain is intrinsically directional as a result of the phase-matching condition (Figure 5.1a). The steady-state lasing condition requires the power loss rate γ to be balanced by the Brillouin gain, which leads to the clamping condition of the pump powers $|A_j|^2 = \gamma(1 + 4\Delta\Omega_j^2/\Gamma^2)/2g_0$ [48]. As shown in the Methods, these conditions remain valid for nonzero dissipative backscattering ($\kappa \neq 0$) within the regime where EP-enhanced rotation measurement is performed (the unlocked regime defined below). As a result, Eq. (5.1) simplifies above laser threshold to the following form:

$$H_0 = \begin{pmatrix} \omega_0 + \frac{\gamma}{\Gamma}\Delta\Omega_1 & i\kappa \\ i\kappa & \omega_0 + \frac{\gamma}{\Gamma}\Delta\Omega_2 \end{pmatrix} \tag{5.2}$$

With the introduction of κ, the lasing system exhibits a frequency locking-unlocking transition when varying the pump detuning frequency. The locking regime is known in ring laser gyroscopes to create a sensing dead band for rotations [3]. In the frequency unlocked regime, the two lasing modes oscillate with distinct angular frequencies ω_{s+} and ω_{s-}, which are the eigenvalues of the Hamiltonian (Eq. (5.2)).

$$\omega_{s\pm} - \omega_r = \frac{\gamma/2\Gamma}{1+\gamma/\Gamma}\left(\Delta\omega_p \pm \sqrt{\Delta\omega_p^2 - \Delta\omega_c^2}\right) \tag{5.3}$$

where $\omega_r \equiv \omega_0 + \gamma(\omega_{p_1} - \Omega_{\text{phonon}})/\Gamma$ and $\Delta\omega_c \equiv 2\Gamma\kappa/\gamma$ is defined as a critical pump frequency detuning where the system state is at an EP. In deriving this result, it is important to note that the Hamiltonian (Eq. (5.2)) depends weakly upon its own eigenvalues through the appearance of $\Delta\Omega_1$ and $\Delta\Omega_2$ (see derivation in Methods). The SBL beating frequency is readily extracted by taking the difference of the above eigenfrequencies, $\Delta\omega_s \equiv |\omega_{s+} - \omega_{s-}|$:

$$\Delta\omega_s = \frac{\gamma/\Gamma}{1+\gamma/\Gamma}\sqrt{\Delta\omega_p^2 - \Delta\omega_c^2} \tag{5.4}$$

This equation is plotted in Figure 5.1c. The dissipative coupling between the clockwise (CW) and counterclockwise (CCW) lasing modes induces second-order EPs at critical pump-detuning frequencies $|\Delta\omega_p| = \Delta\omega_c$ where the eigenfrequencies as well as the eigenmodes coalesce. For pump detuning $|\Delta\omega_p| > \Delta\omega_c$ the eigenfrequencies bifurcate and the eigenmodes are an unbalanced hybridization of CW and CCW modes. For pump detuning $|\Delta\omega_p| < \Delta\omega_c$ the eigenfrequencies (real part of the eigenvalues) are equal but have different loss rates.

5.2 Enhancement near the exceptional point

To verify the EP physics predicted above, a high-quality-factor ($Q \approx 10^8$) silica wedge resonator [67] is counter-pumped as shown in Figure 5.1a at distinct frequencies determined by radio-frequency modulation of a single laser (~1552.5 nm). Coupling into the resonator is realized from both ends of a fiber taper [59, 87].

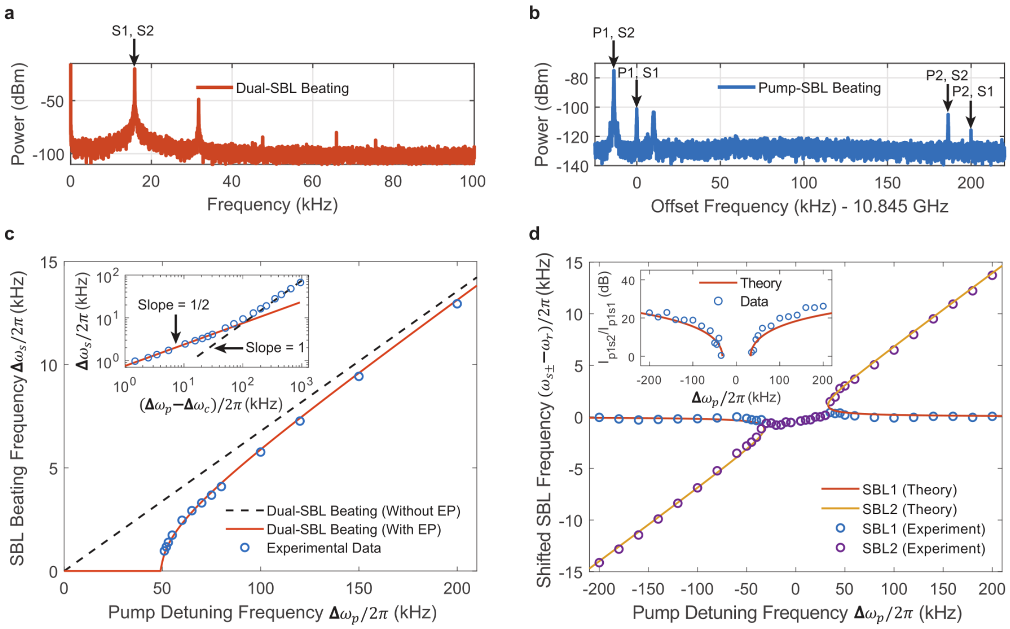

Figure 5.2: **Measurement of the eigenmode properties. a,** Typical measured dual-SBL beating spectrum. **b,** Typical pump-SBL beating spectrum with frequency axis shifted approximately 10.845 GHz to center the pump1-SBL1 beating peak. The individual pump-SBL beating peaks are identified. **c,** Measured dual-SBL beating frequency versus pump detuning frequency (blue circles). Red solid curve is fitting ($\gamma/\Gamma = 0.073$ and $\kappa = 1.80$kHz) and black dotted line corresponds to $\kappa = 0$ ($\gamma/\Gamma = 0.073$). The data have a slope 1/2 (slope 1) near (away from) the EP in the log-log plot provided in the inset. This data used another mode with a larger κ compared to panel **d**. **d,** Measured shifted frequencies of the two SBLs $(\omega_{s\pm} - \omega_r)/2\pi$ versus pump detuning frequency. Theoretical values of $(\omega_{s+} - \omega_r)/2\pi$ and $(\omega_{s-} - \omega_r)/2\pi$ with $\gamma/\Gamma = 0.076$ and $\kappa = 1.23$kHz are plotted as red and yellow lines, respectively. The experimental data of the shifted SBL1 (SBL2) frequency is shown as blue (purple) circles. The inset shows the measured power ratio of CCW components of the lasing modes (blue circles) obtained by analysis of spectral components in panel **b** and agrees reasonably well with the theoretical prediction (red solid curve).

One of the pump frequencies is Pound-Drever-Hall locked to a resonator mode by feedback control to the laser. The second pump frequency is then tuned for state vector control. The two pump powers are stabilized via power feedback. An electrical spectrum analyzer was used to measure the photo-detected dual-SBL beating frequency $\Delta\omega_s/2\pi$ (Figure 5.2a) and the SBL-pump beating frequency (Figure 5.2b). Plots of these frequencies versus the pump frequency detuning are given in Figure 5.2c and Figure 5.2d. Comparisons with Eq. (5.3) and Eq. (5.4) are provided and are in good agreement with measurement. Moreover, the ratio of the CCW components in the eigenmodes was measured from the intensity of the CCW-pump beating with the SBL signals (see Method for analysis) and is plotted as the inset of Figure 5.2d. There is a reasonable agreement between the model and measurement. Within the locked regime, only one Stokes mode is lasing, so this measurement is no longer possible.

When the resonator experiences an angular rotation rate Ω (positive for CW direction), the Sagnac effect further lifts the degeneracy of the CW and CCW modes by shifting the CW and CCW mode frequencies by $\Delta\omega_{\text{Sagnac}} = \mp 2\pi D\Omega/n_g\lambda$ where D is the resonator diameter, n_g is the group index of the passive cavity mode, and λ is the laser wavelength [12]. This modifies the SBL beating frequency as follows:

$$\Delta\omega_s = \frac{\gamma/\Gamma}{1+\gamma/\Gamma}\sqrt{\left(\Delta\omega_p - \Gamma\Delta\omega_{\text{Sagnac}}/\gamma\right)^2 - \Delta\omega_c^2} \tag{5.5}$$

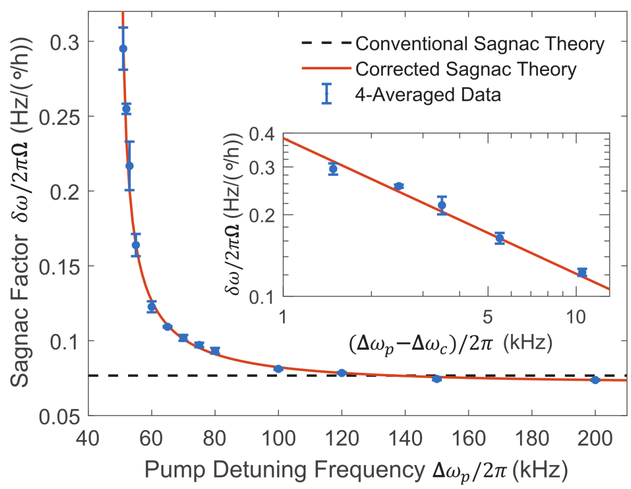

Figure 5.3: **Measured Sagnac scale factor $S(\Delta\omega_p)$ compared with model.** The blue dots are data (each point is an average of four measurements) while the red curve is the theoretical prediction using Eq. (5.6). The mode-pulling factor $1/(1+\gamma/\Gamma)$ slightly reduces the Sagnac factor at large pump detuning. The black dashed line gives the conventional (non EP-enhanced) Sagnac factor. The inset shows a log-log plot of 5 data points near the EP with a slope of -1/2, further verifying that the Sagnac factor enhancement is proportional to $(\Delta\omega_p - \Delta\omega_c)^{-1/2}$.

Accordingly, the counter-pumped Brillouin system can serve as a gyroscope for measuring the rotation signal Ω by monitoring the dual-SBL beating $\Delta\omega_s$. For comparison with measurements below, the Sagnac scale factor S is calculated as the derivative of the SBL splitting frequency with respect to the applied rotation rate amplitude Ω:

$$S = \left.\frac{\partial\Delta\omega_s}{\partial\Omega}\right|_{\Omega=0} = \frac{2\pi}{1+\gamma/\Gamma}\frac{\Delta\omega_p}{\sqrt{\Delta\omega_p^2 - \Delta\omega_c^2}}\frac{D}{n_g\lambda} \tag{5.6}$$

where a linear response requires $\Gamma\Delta\omega_{\text{Sagnac}}/\gamma \ll \Delta\omega_p$. In this equation, the coefficient $1/(1+\gamma/\Gamma)$ is a correction from the mode-pulling effect, and the factor

$\Delta\omega_p/\sqrt{\Delta\omega_p^2 - \Delta\omega_c^2}$ is the enhancement caused by the square-root dependence at the EP. This enhancement originates from the steep slope of the response curve near the EP (Figure 5.1c) so that the Sagnac scale factor surpasses the conventional value.

To measure rotations and verify the EP enhancement, the resonator was packaged in a small metal box with one edge hinged and the opposing end attached to a PZT stage in a manner similar to that used in ref. [12]. As an aside, that reference used a single pump in a cascaded SBL arrangement for rotation sensing. Such an arrangement, however, excludes EP physical effects because the underlying states occur on distinct cavity longitudinal modes. To create a precise rotation, a sinusoidal oscillation was generated by the PZT at a 1 Hz rate with a fixed amplitude (equivalent to 410 deg/h). The resulting time-varying dual-SBL beating frequency was recorded using a frequency counter, and the amplitude of the modulated frequency was extracted by applying a fast-Fourier transform to the counter signal. Frequency modulation amplitudes were recorded at a series of pump frequency detunings. The resulting Sagnac scale factor (i.e., the SBL difference frequency modulation amplitude divided by the applied rotation-rate amplitude) is plotted in Figure 5.3. A boosted Sagnac scale factor by up to 4× compared to the non-EP-enhanced case is observed when operating close to the EP (i.e., near the critical detuning frequency). There is good agreement between Eq. (5.6) and the measurement as shown in Figure 5.3.

While the Sagnac scale factor is observed to increase near the exceptional point, fluctuation mechanisms also exert a greater impact on the measurement leading to relatively larger error bars. At present, these are the result of technical noise contributions associated with thermal and pumping power fluctuations. The consideration of fundamental limits to sensor signal-to-noise near an exceptional point is a very recent area of theoretical study [88]. With a reduction of technical sources of noise in the present system, it should be possible to explore this issue.

5.3 Methods: Detailed derivation related to EP physics

Origin of the dissipative coupling

In a standing-wave mode basis, the optical loss induced by the fiber taper or any other spatially localized absorption or dissipative scattering element will be different for each mode and can be captured by the following contribution to the Hamiltonian:

$$H_{\text{taper}} = \begin{pmatrix} -i\gamma_1 & 0 \\ 0 & -i\gamma_2 \end{pmatrix}. \tag{5.7}$$

Changing to a traveling wave basis (CW and CCW) by using the relation $|\Phi_\pm\rangle = (|\mathrm{CW}\rangle \pm |\mathrm{CCW}\rangle/\sqrt{2}$ gives the following Hamiltonian in the new basis,

$$H_{\mathrm{taper}} = \begin{pmatrix} -i\gamma_{\mathrm{common}} & 0 \\ 0 & -i\gamma_{\mathrm{common}} \end{pmatrix} + \begin{pmatrix} 0 & i\kappa \\ i\kappa & 0 \end{pmatrix} \tag{5.8}$$

where $\gamma_{\mathrm{common}} = (\gamma_1 + \gamma_2)/2$ and $\kappa = (\gamma_1 - \gamma_2)/2$. The first term is the common loss (out-coupling loss of the taper) while the second term is the dissipative backscattering in Eq. (5.1).

Validity of clamping condition

Note that the Hamiltonian in Eq. (5.1) depends on its eigenvalues ω_{s_j} through the Brillouin gain factor $g_j = g_0/[1+2i(\omega_{p_j} - \Omega_{\mathrm{phonon}} - \omega_{s_j})/\Gamma]$. However, by separating the Brillouin gain factor into real part and imaginary part as follows:

$$\mathrm{Re}(g_j) = \frac{g_0}{1 + 4\frac{(\omega_{p_j} - \Omega_{\mathrm{phonon}} - \omega_{s_j})^2}{\Gamma^2}} \tag{5.9}$$

$$\mathrm{Im}(g_j) = \mathrm{Re}(g_j)\left[1 - 2i\left(\omega_{p_j} - \Omega_{\mathrm{phonon}} - \omega_{s_j}\right)/\Gamma\right] \tag{5.10}$$

it can be seen that for mode pulling that is small compared to the cavity linewidth (which is the case in this work), ω_{s_j} can be replaced by ω_0 in the denominators of Eq. (5.9) and Eq. (5.10), leaving the eigenvalue dependence only in the dispersive term (numerator). Furthermore, by defining normalized quantities:

$$I_j \equiv \frac{\mathrm{Re}(g_j)|A_j|^2}{\gamma/2}, \quad k \equiv \frac{\kappa}{\gamma/2}, \quad n_{pj} \equiv \frac{\omega_{p_j} - \Omega_{\mathrm{phonon}}}{\gamma/2}, \quad x \equiv \frac{\omega_s}{\gamma/2}, \quad x_0 \equiv \frac{\omega_0}{\gamma/2}, \quad r \equiv \frac{\gamma}{\Gamma},$$

the Hamiltonian reduces to:

$$\tilde{H}_0 \equiv \frac{H_0}{\gamma/2} = x_0\mathbb{I} + \begin{pmatrix} i(I_1 - 1) + rI_1(n_{p1} - x) & ik \\ ik & i(I_2 - 1) + rI_2(n_{p2} - x) \end{pmatrix}. \tag{5.11}$$

The eigenvalues $x_\pm$ can be solved from $\det(\tilde{H}_0 - x\mathbb{I}) = Ax^2 + Bx + C = 0$ where

$$\begin{aligned} A &= (1 + I_1 r)(1 + I_2 r), \\ B &= 2i - 2x_0 - (I_1 + I_2)(i - ir + x_0 r) - r(I_1 n_{p1} + I_2 n_{p2}) + I_1 I_2[2i + (n_{p1} + n_{p2})r], \\ C &= k^2 + (-i + x_0)^2 + (-i + x_0)[I_1(i + n_{p1}r) + I_2(i + n_{p2}r)] + I_1 I_2(i + n_{p1}r)(i + n_{p2}r). \end{aligned}$$

Because the two eigenvalues $x_\pm = (-B \pm \sqrt{B^2 - 4AC})/2$ should both be real (i.e., above laser threshold operation), the following equations can be derived from $\mathrm{Im}(x_\pm) = 0$,

$$\mathrm{Im}(B^2 - 4AC) = 2r(r+1)(I_1 - I_2)[I_1 I_2 r(n_{p1} - n_{p2}) + I_1(np_1 - x_0) + I_2(x_0 - n_{p2})] = 0 \tag{5.12}$$

$$\mathrm{Im}(B) = 2rI_1I_2 + (I_1 + I_2)(1 - r) - 2 = 0 \tag{5.13}$$

It can be obtained from Eq. (5.12) that $I_1 = I_2$. Inserting this result into Eq. (5.13) gives $I_1 = I_2 = 1$ yielding $|A_j|^2 = \gamma(1 + 4\Delta\Omega_j^2/\Gamma^2)/2g_0$ where $\Delta\Omega_j = \omega_{p_j} - \Omega_{\mathrm{phonon}} - \omega_{s_j}$. These are also the $\kappa = 0$ gain clamping conditions used to simplify the Hamiltonian to the form given in Eq. (5.2). Numerical solution of the eigenvalue equation confirms that this result holds for the unlocked regime. On the other hand, numerical solution also shows that in the locked regime, only one eigenvalue can be real for any combination of pumping powers (i.e., only one mode lases in the locked regime). Moreover, low and high loss eigenvalues exist so that one mode has a lower threshold pumping power. An equal pump power solution ($I_1 = I_2$) is still possible for laser action, but this condition is no longer unique.

Characterization of eigenmodes

The eigenmodes of Eq. (5.2) are:

$$|\Psi_+\rangle = \frac{1}{N}\begin{pmatrix} -i \\ \left[\Delta\omega_p/\Delta\omega_c + \sqrt{\left(\Delta\omega_p/\Delta\omega_c\right)^2 - 1}\right] \end{pmatrix} \tag{5.14}$$

$$|\Psi_-\rangle = \frac{1}{N}\begin{pmatrix} \left[\Delta\omega_p/\Delta\omega_c + \sqrt{\left(\Delta\omega_p/\Delta\omega_c\right)^2 - 1}\right] \\ i \end{pmatrix} \tag{5.15}$$

where N is normalization. These lasing eigenmodes are valid in the uncoupled regime of operation ($\left|\Delta\omega_p\right| > \Delta\omega_c$) and are hybrid modes of the original CW and CCW modes. To make the data plot within the inset of Figure 5.2d the laser output in the CCW direction (combination of two laser Stokes waves) was monitored. This combined CCW field is given by:

$$|\mathrm{CCW}\rangle = \frac{1}{N'}\left\{\left[\Delta\omega_p/\Delta\omega_c + \sqrt{\left(\Delta\omega_p/\Delta\omega_c\right)^2 - 1}\right]|\Psi_-\rangle - i\,|\Psi_+\rangle\right\} \tag{5.16}$$

Where N' is another normalization. The ratio of powers of the components was determined by heterodyning this field with a CCW pump field and then measuring the respective Pump-SBL$_{1,2}$ beat components on an electrical spectrum analyzer.

The ratio of the powers in these beat frequency components is the ratio of the powers in the CCW Stokes' waves components:

$$\frac{I_{s2}}{I_{s1}} = \left| \left|\Delta\omega_p/\Delta\omega_c\right| + \sqrt{\left(\Delta\omega_p/\Delta\omega_c\right)^2 - 1} \right|^2 \tag{5.17}$$

which directly follows from Eq. (5.16).

It is also interesting to note that in the locked regime ($\left|\Delta\omega_p\right| / \Delta\omega_c < 1$) numerical solution shows that eigenvector solutions having an equal admixture of CW and CCW waves occur when $I_1 = I_2$, but at distinctly different threshold power levels (i.e., the two states have different loss rates). Moreover, this pumping combination is not unique so lasing solutions featuring an unbalanced admixture of CW and CCW states are also possible. The (locked regime) equatorial trajectories shown in Figure 5.1 represent the low and high loss $I_1 = I_2$ trajectories (i.e., equal CW and CCW admixture).

As an aside, the measurement in Figure 5.2c and Figure 5.2d use the beat note spectra in Figure 5.2a and Figure 5.2b. There are additional lines in these spectra that are believed to originate from nonlinear mixing in the Brillouin interaction (a third order nonlinear interaction). This four-wave-mixing process becomes more significant near the EP where the CW and CCW modes strongly interact with each other. It impacts the intensity of the beating lines but leaves their frequencies intact. As a result, data for the eigenmode components slightly fluctuate around the theoretical value while the data of the pump-SBL and dual-SBL frequencies fit well with the theory (see Figure 5.2c and d).

Kerr-induced shift

The Kerr effect shifts the resonance frequency by adding the following term into the Hamiltonian:

$$H_{\text{Kerr}} = \begin{pmatrix} -\eta\left(|\alpha_1|^2 + 2\,|\alpha_2|^2\right) & 0 \\ 0 & -\eta\left(2\,|\alpha_1|^2 + |\alpha_2|^2\right) \end{pmatrix} \tag{5.18}$$

where $\eta = n_2\hbar\omega^2 c/Vn_0^2$ is the single photon induced nonlinear angular frequency shift. The corrected beating frequency (without rotation) reads:

$$\Delta\omega_s = \frac{1}{1+\gamma/\Gamma}\sqrt{\left[\frac{\gamma}{\Gamma}\Delta\omega_p + \eta\left(|\alpha_2|^2 - |\alpha_1|^2\right)\right]^2 - 4\kappa^2} \tag{5.19}$$

The correction from the Kerr effect is therefore equivalent to shifting $\Delta\omega_p$ by angular frequency $\eta\Gamma(|\alpha_2|^2 - |\alpha_1|^2)/\gamma$. In the experiment, this Kerr shift was minimized by centering the locking zone at zero pump detuning by adjusting the two pump powers. After that, the pump powers were locked so that the two SBL powers were balanced. The subsequent pump detuning changes required to make the measurement affected the SBL power, but only negligibly. Specifically, the Kerr shift is around 10s of Hz after a pump detuning change by 200kHz. This is negligible in comparison to the Stokes frequency separation changes measured in Figure 5.2c and Figure 5.2d. Moreover, the dithering measurement in Figure 5.3 was insensitive to these constant Kerr-induced shifts since it measured the amplitude of a sinusoidal rotation.

5.4 Conclusion

In summary, phase matching of Brillouin gain and dispersion in a microresonator system has been shown to provide precise control of clockwise and counter-clockwise laser modes near an exceptional point. This control and the inherent high relative stability of the laser modes makes the possible observation of the EP-enhanced Sagnac effect. By measurement of rotations with an approximate amplitude of one revolution per hour, it was possible to observe boosts to the Sagnac scale factor by up to 4× near the EP. This work, therefore, provides a new platform for studying EPs in a nonlinear optical system while also demonstrating a potential path for improvement of rotation measurement sensitivity.

Chapter 6

FIBER TAPER CHARACTERIZATION BY OPTICAL BACKSCATTERING REFLECTOMETRY

Abstract

Fiber tapers provide a way to rapidly measure the spectra of many types of optical microcavities. Proper fabrication of the taper ensures that its width varies sufficiently slowly (adiabatically) along the length of the taper so as to maintain single spatial mode propagation. This is usually accomplished by monitoring the spectral transmission through the taper. In addition to this characterization method, it is also helpful to know the taper width versus length. By developing a model of optical backscattering within the fiber taper, it is possible to use backscatter measurements to characterize the taper width versus length. The model uses the concept of a local taper numerical aperture to accurately account for varying backscatter collection along the length of the taper. In addition to taper profile information, the backscatter reflectometry method delineates locations along the taper where fluctuations in fiber core refractive index, cladding refractive index, and taper surface roughness each provide the dominant source of backscattering. Rayleigh backscattering coefficients are also extracted by fitting the data with the model and are consistent with the fiber manufacturer's datasheet. The optical backscattering reflectometer is also used to observe defects resulting from microcracks and surface contamination. All of this information can be obtained before the taper is removed from its fabrication apparatus. The backscattering method should also prove useful for characterization of nanofibers.

Introduction

Over the last decade, a remarkably wide range of new research areas and applications has emerged that relies upon high-quality-factor optical microcavities [22, 23]. These include frequency microcombs [36, 37] including soliton mode-locked microcombs [38–40], nonlinear parametric and stimulated oscillators [25–27, 30], harmonic generation[41], Brillouin signal processing [28] and cooling [29], cavity optomechanics [31–35], studies of physical symmetry [42, 43], cavity

This chapter was adapted from the paper, Y.-H. Lai, et al., "Fiber taper characterization by optical backscattering reflectometry," Opt. Express **25** (2017).

quantum electrodynamics [44, 45], sensing [77–80], optical gyroscopes [12, 15], and reference cavities [49, 50, 89]. Rapid prototyping and testing of both discrete and monolithic resonators in the laboratory frequently make use of fiber tapers for optical coupling [59, 87, 90]. Beyond rapid testing, this method provides controllable loading of the resonator by variation of a coupling air gap [87], which is often essential to understand performance optimization. Tapers are also intrinsically fiber compatible so that their interface with pump lasers, detectors and, spectrometers is straightforward. Outside of their use in microresonator research, fiber tapers and the closely-related optical nanofiber are applied to trap atoms [91, 92], for supercontinuum generation [93, 94], and in sensing applications [95, 96]. The methods developed here should also prove useful in these applications.

A properly fabricated fiber taper can readily achieve both critical and over-coupled operation with high ideality [59, 87, 97, 98]. Ideal tapers have two key features. First, they are nearly single mode near the region at which optical coupling to the resonator will occur. Second, they maintain propagation in a single spatial mode as the fiber profile is reduced from a width of 125 microns (for SMF-28 fiber) to a width of around 1 micron. This latter adiabatic condition requires that the taper width varies slowly along its length [99, 100]. The adiabatic condition can be tested by measuring coupling ideality [59] or monitoring the spectral transmission through the taper [87, 98].

This work studies the application of optical backscatter reflectometry (OBR) to characterize the width versus length of fiber tapers. Instead of using an optical microscope (limited spatial resolution) or a scanning electron microscope (potential taper damage risk) for point-wise profile examination, it is shown that modeling combined with the OBR data can extract the taper profile with good accuracy (within 20% of the width profile obtained by measurement using an SEM). The OBR data also provide information on imperfections along the taper. Significantly, the method is nondestructive and can be applied while the taper is within its fabrication assembly. It is therefore useful when developing a taper pulling schedule, when using a new fiber type for taper fabrication, in verifying taper pulling reproducibility, and for identification of defects and contamination. It is possible to discern distinct regions where the optical mode propagates primarily within the fiber core, the fiber cladding, and finally the taper waist region. Rayleigh scattering coefficients are also extracted using the backscattering model [101, 102] and the inferred values are consistent with the scattering coefficients of the fibers.

In the following sections, example OBR measurements are presented and compared with the corresponding taper width versus length profiles obtained by scanning electron microscopy. The model used to infer taper profile information from backscatter data is then developed. Finally, the model is applied in combination with OBR data to study several tapers.

6.1 Taper fabrication and backscattering reflectometry

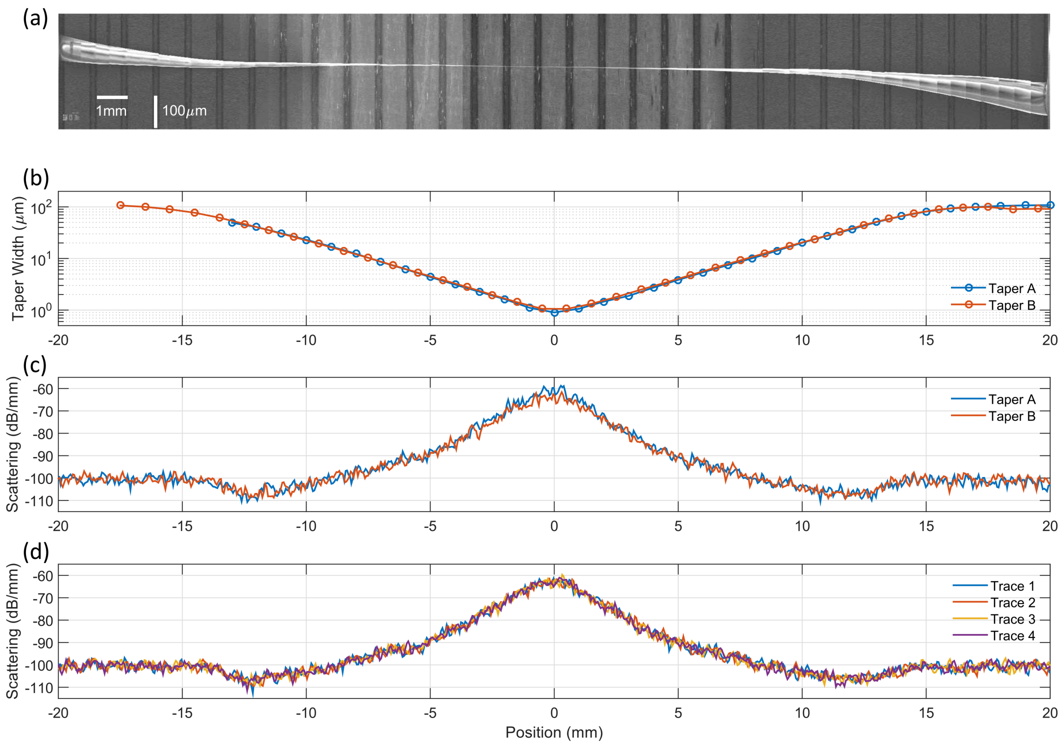

Figure 6.1: **Taper width versus position measurement and OBR measurement. a,** A composite image is presented for a fiber taper. The image was produced by stitching together a series of scanning electron microscope (SEM) images as described in the text. The black vertical lines in the image are 1 mm tick marks on a metal ruler and provide a reference used to construct the image. The scale factors for the vertical and horizontal axes are different and are provided in the legend. **b,** Width versus position profiles measured on two different tapers are presented. The tapers were fabricated under the same conditions and measured using the SEM method in panel **a**. **c,** OBR data for the two tapers in panel **b**. The consistency between taper profiles and scattering traces verifies the reproducibility of the fabrication system. **d,** Four sets of OBR data taken using one taper illustrate the consistency of the OBR measurement.

To fabricate a taper, the plastic jacket is removed along a section of SMF-28 fiber, and the two ends of the exposed glass fiber are attached to fiber holders in a chuck. The holders are free to slide under the control of motorized translation stages. The exposed fiber is heated with a ceramic microheater, and the motorized stages gradually pull the fiber at a speed of approximately 0.2 millimeters per second. The taper waist width is adjusted by either changing the pulling length or by varying the temperature of the microheater. After fabrication, the taper is left in its fabrication apparatus, and backscatter characterization is performed at room temperature.

A scanning electron microscope (SEM) is used to image the taper profile as shown in Figure 6.1a. The image is a composite of a series of scans. The vertical and horizontal scales in the image are different (see scale bars in legend). To construct the image, a fiber taper is mounted on a metal ruler with 1 mm tick spacings. The ruler then functions as a reference to combine the SEM images together. Using such images recorded for two tapers, width versus position plots were constructed in Figure 6.1b. The plots closely match and verify the reproducibility of the taper fabrication system. The vertical scale is logarithmic and also shows that (away from the taper waist region) the taper width varies exponentially over a wide range of the taper length. This behavior is expected on account of a well-defined softened region of glass produced by the heater [98]. The narrow region of the taper has a length of only a few millimeters in the present work. However, the backscatter method should also be able to characterize structures having longer waist regions.

Backscatter reflectometry was performed using a LUNA OBR 4400. This instrument measures backscatter strength versus position using the frequency domain method. Optical frequency domain reflectometry uses swept-frequency coherent interferometry to measure a device under test [103–106]. In the instrument, the laser center wavelength is nominally 1566 nm, and the laser sweeping bandwidth is 88 nm. The highest spatial resolution setting along the propagation direction is 10 microns. OBR sweep signals are presented in Figure 6.1c, measured using the two tapers from Figure 6.1b. The signals show a high level of consistency. In addition, four OBR sweep traces performed on a single taper are shown in Figure 6.1d to verify the repeatability of the OBR measurement.

6.2 Scattering modeling and simulation

Refractive-index fluctuations in the glass [107–109] and surface-roughness scattering in the taper waist region are the dominant sources of scattering. The resulting backscattered light must be collected by the fiber waveguide so as to be guided to the OBR instrument. The collection efficiency for this process has been analyzed for single-mode optical fiber [101] and depends upon the local mode field diameter. Fiber waveguides with smaller mode field diameters are more efficient in collecting the backscattered light, because they have a larger numerical aperture. The taper adiabaticity condition makes it possible to introduce a local backscatter collection efficiency (effectively, there is a local numerical aperture). The collection efficiency results originally developed for standard optical fiber can then be applied to a fiber taper where the mode field diameter is slowly varying.

To further explore the backscattering process, the simulated intensity profile of an HE_{11} mode [110] along a taper is provided in Figure 6.2. Comparing the profile with the measured backscatter data in Figure 6.1c, the initial backscatter level in Figure 6.1c is determined by the refractive index fluctuations of the SMF-28 fiber core region. As the core tapers down in width, there is an initial reduction in the backscattering level that accompanies the expansion of the optical mode into the surrounding glass cladding region. This reduction is expected on account of the reduced optical backscattering collection efficiency with increasing mode field diameter (i.e., reduced local numerical aperture). Then, when the taper width is less than 50 microns, increasing confinement provided by the glass-air interface boosts the backscattering collection efficiency. Since the mode field now extends well outside of the fiber core, the backscattering signal in this region is dominated by refractive index fluctuations within the fiber cladding. Finally, when the taper width is around 3-4 microns, the glass-air interface scattering becomes dominant. Despite the relatively small cross-sectional area presented by surface roughness fluctuations in comparison to the cladding density fluctuations, the large difference in the refractive index of air and dielectric increases the strength of the surface scattering [111, 112]. To connect backscattering power to taper width versus position, it is in principle possible to construct a look-up table based on taper calibrations. However, a model of backscattering has several advantages over such an empirical method. First, the model provides a physical understanding of the behavior observed in the taper backscattering signal. Second, it provides quantitative values for Rayleigh scattering coefficients associated with core, cladding, and surface scattering. Finally, these Rayleigh coefficients provide reference data that serve to monitor the taper fabrication process over time (e.g., surface smoothness of the waist region).

The above physical picture of scattering motivates a model for normalized backscatter power per unit length. The contributions to backscattering from the core, cladding and taper surface are described by three terms in Eq. (6.1) below. Details on the derivation are provided in Section 6.4.

$$\frac{1}{P_{\text{in}}}\frac{dP_{\text{OBR}}(w(z))}{dz} = \alpha_{\text{core}}\sigma_{\text{core}}(w(z)) + \alpha_{\text{clad}}\sigma_{\text{clad}}(w(z)) + \beta\eta(w(z)) \tag{6.1}$$

where P_{in} is the total input power to the taper and $dP_{\text{OBR}}(w(z))/dz$ is the backscattered power per unit length at taper position z with $w(z)$ the width of the taper at position z. α_{core} and α_{clad} are the Rayleigh scattering coefficients in the core and cladding regions, respectively. β is the Rayleigh surface scattering coefficient at the taper-air interface (see Section 6.4). These parameters are determined by fitting to the OBR data. σ_{core} and σ_{clad} are related to backscattering contributions in the core and in the cladding respectively. η is related to backscattering contributions at the taper glass-air interface. These parameters account for cross-sectional variations of the core, cladding, and surface as well as the local coupling efficiency of the scattered light into the taper guided mode. Their forms follow from the analysis for backscattering in standard optical fiber [101]:

$$\sigma_{\text{core, clad}} \equiv \frac{3\lambda^2}{8\pi n^2}\frac{\int_{\text{core, clad}} |\vec{E}(\vec{r})|^4 dS}{\left(\int_{\text{all}} |\vec{E}(\vec{r})|^2 dS\right)^2} \tag{6.2}$$

$$\eta \equiv \frac{3\lambda^2}{8\pi n^2}\frac{\oint_{\text{interface}} |\vec{E}(\vec{r})|^4 dl}{\left(\int_{\text{all}} |\vec{E}(\vec{r})|^2 dS\right)^2} \tag{6.3}$$

where each integration is performed at a specific width $w(z)$ along the fiber taper. λ is the center wavelength of the OBR laser scan, and n is the fiber refractive index (small differences in core and cladding regions are neglected). The analysis leading to these forms is provided in Section 6.4. A key assumption made in the analysis is that powers from distinct, random scatterers are added to compute the total scattered power. This is equivalent to assuming that the correlation length for scattering centers is much smaller than the optical wavelength. A finite element solver is used to calculate σ_{core}, σ_{clad}, and η as a function of the taper width, w. The results are shown in Figure 6.3. Because, as noted above, the backscatter signal is generated using a wavelength sweep over 88 nm centered at 1566 nm, it is important to check the wavelength dependence of the parameters in Figure 6.3. It is found that there is a negligible variation in their values relative to the scale of signal variations in the measurement.

In the analysis, it is assumed that the taper maintains a circular cross section and that the ratio of core width to taper width is constant along the taper. Moreover,

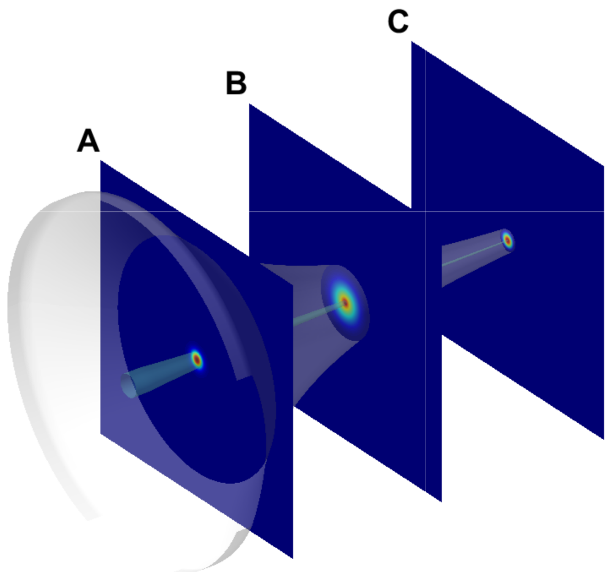

Figure 6.2: **Illustration showing a fiber taper with a mode profile superimposed.** The blue planes give the energy density profiles associated with the transverse polarization. Initially in region A, light is confined in the core region, and the fluctuations in the refractive index of the core dominate the scattering process. In region B, the taper width is reduced to tens of microns, and a substantial portion of the optical power is propagating within the cladding region. Here, the refractive-index fluctuations of the cladding dominate the scattering process. Region C occurs around the taper waist where the surrounding air functions as the cladding, and the taper surface roughness dominates the scattering process.

the statistical properties of the scatterers within the core and cladding regions are assumed to be uniform in each region. Also, scattering centers at the glass-air interface are assumed to be spatially uniform in their statistical properties. These assumptions mean that α_{core}, α_{clad}, and β are treated as constants and, based on the analysis [101, 102], are expected to be intensive quantities. Finally, an additional assumption is that the attenuation of the input power along the length of the taper is so weak that the propagating power along the length of the fiber taper can be treated as constant.

An additional effect must be added to the model on account of the effective index variation along the length of the fiber taper as its width varies. In performing a conversion of time delay into distance, the OBR system assumes that the effective index is a constant over the length of the optical fiber (in this case SMF-28). However, since the effective refractive index decreases as taper width decreases, light propagates faster within the taper region, and this causes the OBR to detect the signal earlier and thereby incorrectly compute a scattering location too close to the OBR instrument. Accordingly, a location z_{OBR} given by the following equation is

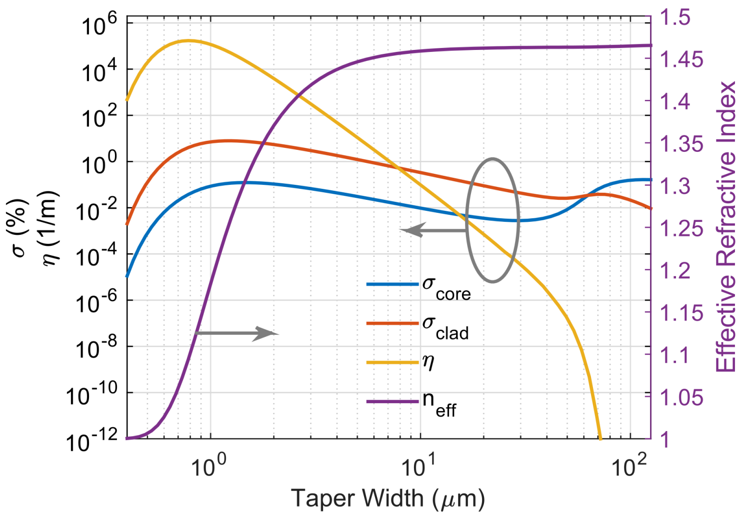

Figure 6.3: **Calculation of the parameters σ_{core}, σ_{clad} and η in Eq. (6.1) versus the taper width w.** The calculations used a finite element method solver. The effective index, n_{eff}, is also presented. For the narrowest taper widths n_{eff} approaches unity, the index of air, while at the largest widths it has the index of the SMF-28 fiber used to prepare the fiber taper. The wavelength assumed is 1566 nm and SMF-28 parameters are: $w_{\text{clad}} = 125\mu$m, $w_{\text{core}} = 8.2\mu$m, $n_{\text{core}} = 1.4682$, $n_{\text{clad}} = 1.4631$.

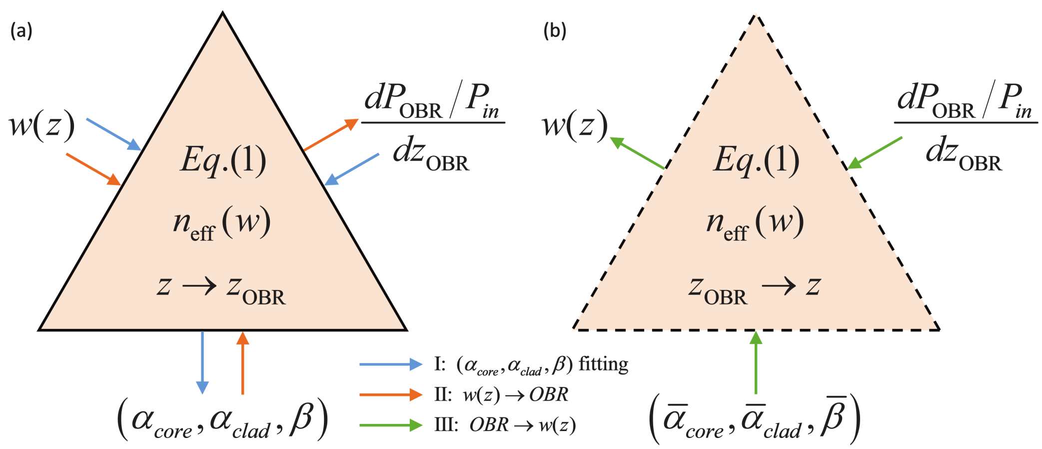

Figure 6.4: **Flow charts illustrating three distinct taper-related calculations that are possible. a,** Calculation I (blue): a known taper profile is combined with OBR data to determine fitting parameters ($\alpha_{\text{core}}, \alpha_{\text{clad}}, \beta$). Calculation II (orange): a known taper profile is combined with average fitting parameters ($\bar{\alpha}_{\text{core}}, \bar{\alpha}_{\text{clad}}, \bar{\beta}$) to predict an OBR signal. **b,** Calculation III: an OBR signal is combined with average fitting parameters ($\bar{\alpha}_{\text{core}}, \bar{\alpha}_{\text{clad}}, \bar{\beta}$) to determine a taper profile. This particular measurement is performed in a piecewise fashion on regions where the OBR signal monotonically varies with taper length.

computed by the instrument,

$$\int_0^z n_{\text{eff}}(w(z'))dz' = n_{\text{OBR}} z_{\text{OBR}} \tag{6.4}$$

where $n_{\text{eff}}(w(z))$ is the taper effective index at location z, and n_{OBR} is the effective index assumed by the OBR instrument. Given a taper profile $w(z)$ and using the $n_{\text{eff}}(w)$ from Figure 6.3, it is possible to convert z into z_{OBR} ($z \to z_{\text{OBR}}$) using the above equation. Also, because the OBR signal is a relative scattering per unit length in z_{OBR} units, the form of the left-hand side of Eq. (6.1) in units measured by the OBR instrument is the following:

$$\frac{dP_{\text{OBR}}}{dz} = \frac{dP_{\text{OBR}}}{dz_{\text{OBR}}}\frac{dz_{\text{OBR}}}{dz} = n_{\text{corr}}(w)\frac{dP_{\text{OBR}}}{dz_{\text{OBR}}} \tag{6.5}$$

where the corrected refractive index factor is defined as,

$$n_{\text{corr}}(w) = \frac{n_{\text{eff}}(w)}{n_{\text{OBR}}} \tag{6.6}$$

Therefore, in calculating the instrument measured OBR signal, both the position correction provided by Eq. (6.4) and the scaling correction of Eq. (6.1) given in Eq. (6.5) must be used.

Eqs. (6.1)-(6.6) allow three distinct calculations to be performed that are illustrated schematically in the Figure 6.4 flow charts.

Calculation I [blue arrows in Figure 6.4a]: This calculation computes the $(\alpha_{\text{core}}, \alpha_{\text{clad}}, \beta)$ scattering coefficients. A taper profile is measured ($w(z)$) and used to calculate n_{eff}, σ_{core}, σ_{clad}, and η as a function of z by applying results in Figure 6.3. These results are used to map z into z_{OBR} using Eq. (6.4). Equation (6.1) (in the measured z_{OBR}-units provided by Eq. (6.5)) is then fit to the experimental backscatter data. The result of this fitting is a set of $(\alpha_{\text{core}}, \alpha_{\text{clad}}, \beta)$ constants. To ensure consistent values for $(\alpha_{\text{core}}, \alpha_{\text{clad}}, \beta)$ the fiber type used to fabricate the taper should not be varied. Also, although the taper profile can be varied, such things as the annealing schedule and furnace temperature should be maintained constant so as to ensure similar density fluctuations in the glass [113, 114].

Calculation II [orange arrows in Figure 6.4a]: This calculation uses a measured taper profile and existing $(\alpha_{\text{core}}, \alpha_{\text{clad}}, \beta)$ coefficients to predict an OBR trace for a given taper. A taper profile is first measured ($w(z)$) and used to calculate n_{eff}, σ_{core}, σ_{clad} and η as a function of z by applying the results in Figure 6.3. Conversion of $z \to z_{\text{OBR}}$ is performed as in Calculation I. These results are then combined with the existing $(\alpha_{\text{core}}, \alpha_{\text{clad}}, \beta)$ constants to predict an optical backscatter signal using Eq. (6.1). Averaged constants $(\bar{\alpha}_{\text{core}}, \bar{\alpha}_{\text{clad}}, \bar{\beta})$ obtained by measuring several tapers can be used to improve accuracy.

Calculation III [green arrows in Figure 6.4b]: A third calculation is to determine an unknown taper profile, $w(z)$, from OBR data and averaged scattering coefficients ($\bar{\alpha}_{\text{core}}, \bar{\alpha}_{\text{clad}}, \bar{\beta}$) obtained using other tapers having different profiles. Because the taper width is not a one-to-one function of the OBR signal as shown in Figure 6.1b and 6.1c, it is convenient to perform this calculation in a piecewise fashion within specific taper regions where the OBR signal varies monotonically with length. A taper whose profile ($w(z)$) is to be determined is characterized to obtain its OBR signal versus z_{OBR}. When restricted to the piecewise regions noted above, each OBR data point maps uniquely into a w value using Eq. (6.1) (corrected using the scaling in Eq. (6.5)) in conjunction with Figure 6.3. This establishes the function $w(z_{\text{OBR}})$ since the OBR instrument provides the OBR signal versus z_{OBR}. Using Eq. (6.4), it follows,

$$\frac{dz_{\text{OBR}}}{dz} = n_{\text{corr}}(w(z_{\text{OBR}})) \tag{6.7}$$

from which the conversion of OBR position to actual position ($z_{\text{OBR}} \to z$) can be computed as the following integral,

$$z = \int_0^{z_{\text{OBR}}} \frac{dz'_{\text{OBR}}}{n_{\text{corr}}(w(z'_{\text{OBR}}))} \tag{6.8}$$

This, in turn, allows $w(z_{\text{OBR}})$ to be converted into the actual taper profile $w(z)$. For tapers having widths < 800nm, the taper waist region must be separated in the piecewise analysis since the OBR signal once again becomes multi-valued (see σ_{core}, σ_{clad}, and η curves in Figure 6.3).

6.3 Experiment results

Table 6.1: Rayleigh Scattering Coefficients of SMF-28 Tapers Pulled at 1660°C

Taper Number	Waist Width (μm)	α_{core} (10^{-6}/m)	α_{clad} (10^{-6}/m)	β (10^{-9})
1a	0.49	45.2	81.3	4.39
2a	0.90	51.2	75.0	3.69
3a	1.02	40.9	87.1	3.94
4a	1.05	37.1	90.8	3.46
5a	1.34	49.2	95.2	3.47
6a	1.74	45.5	67.4	4.85
Average		45 ± 5 (11%)	83 ± 10 (12%)	4.0 ± 0.6 (15%)

Determination of taper Rayleigh scattering coefficients ($\alpha_{\text{core}}, \alpha_{\text{clad}}, \beta$)

The coefficients ($\alpha_{\text{core}}, \alpha_{\text{clad}}, \beta$) provide information on refractive index fluctuations in the core, cladding, and interface regions. The coefficients can in principle depend

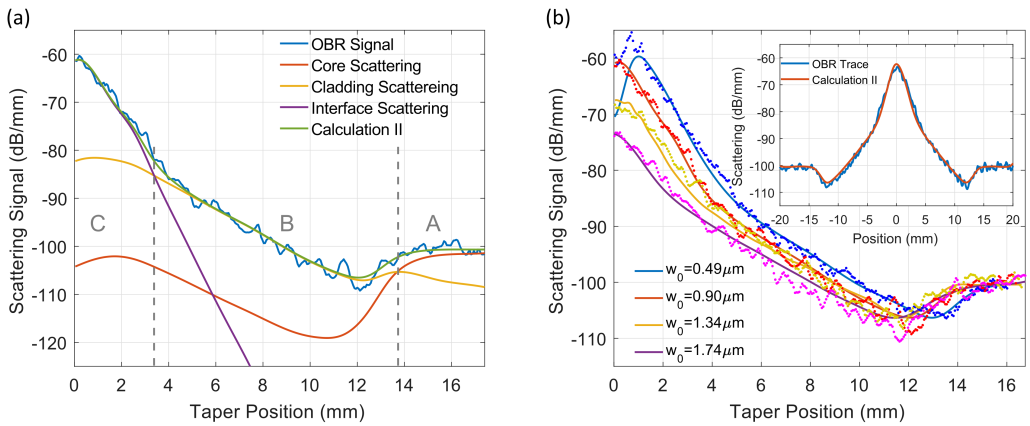

Figure 6.5: **Predicted OBR signal is compared with actual OBR data. a,** OBR data from taper 2a in Table 6.1 is plotted versus taper position relative to the taper waist at one end of the taper. The data are compared with the prediction based on Calculation II using the average parameters in Table 6.1. Also shown are the contributions from the three scattering mechanisms in Eq. (6.1). A, B, and C intervals delineated by the dashed vertical lines (see Figure 6.2) give regions in which each mechanism provides the dominant contribution to total scattering. **b,** Averaged parameters from measurements on the 6 tapers in Table 6.1 are used to predict the OBR signal measurements (dots) from four tapers (Table 6.1) by using Calculation II (solid curves). Taper waist widths are provided in the legend. Note that for the smallest taper width, 0.49 μm, the model successfully predicts the reduction in the OBR scattering at the taper waist qualitatively. Inset: OBR trace over the full length of taper 4a is compared with the prediction using Calculation II.

upon the oven temperature and annealing applied during taper fabrication. Assuming that oven temperature and annealing are not varied, it should not be necessary to remeasure these parameters. In a first test, six tapers were prepared using SMF-28 optical fiber by pulling at 1660°C. The oven temperature was inferred from the manufacturer datasheet and drive current. A range of waist widths was intentionally produced by adjusting the pulling distance for each taper. OBR data was first measured for each taper. After this, the taper profiles, $w(z)$, were measured using an SEM as described in Figure 6.1. A weighted-least-squares fitting of Eq. (6.1) (corrected to z_{OBR} units) to the OBR data is then performed to extract (α_{core}, α_{clad}, β) for each taper using Calculation I. The fitting results are provided in Table 6.1.

Determination of the optical backscatter signal from w(z)

As a test of the Calculation II method to predict OBR signals from a set of parameters, the averaged fitting parameters are calculated in the last row of Table 6.1 and used to compute the backscatter signal from Eq. (6.1) for four tapers (1a, 2a, 5a and 6a in Table 6.1). The computed results for a single taper are shown in Figure 6.5a. The separate contributions to the overall scattering power from the three underlying

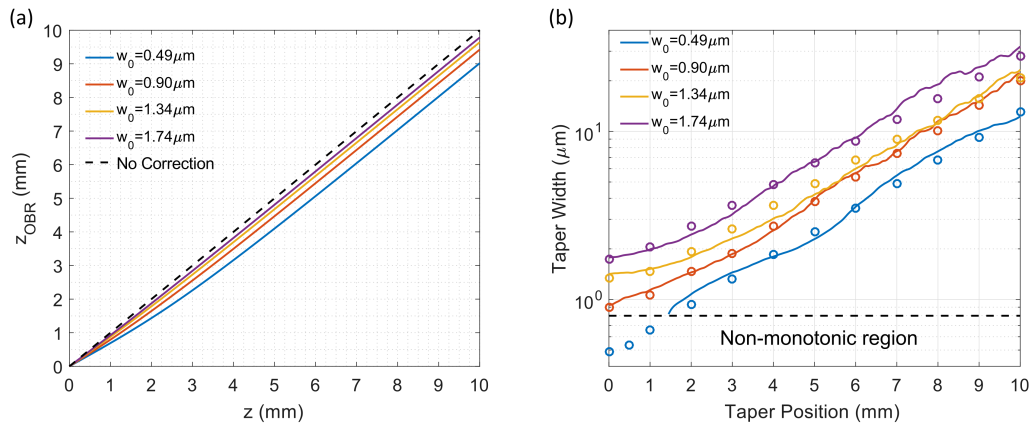

Figure 6.6: **Effective refractive index and taper width reconstruction a,** The position z_{OBR} calculated from Eq. (6.4) plotted versus position z for tapers 1a, 2a, 5a, 6a in Table 6.1. Zero on both axes corresponds to the taper center. The calculated OBR position error ranges from 0.13 mm ($w_0 = 1.74\mu$m) to 0.57 mm ($w_0 = 0.49\mu$m) after 2 mm of light propagation and is caused by the varying effective index along the taper. The legend gives the taper waist width and the black dashed line is the case $z_{\mathrm{OBR}} = z$. **b,** The taper width versus position as determined from the OBR signal using Calculation III is plotted for four tapers from Table 6.1 (solid curves). The circles are the taper profiles measured using an SEM. The taper waist widths are provided in the legend.

contributions are also plotted. In Figure 6.5b, the computed results for the four tapers are presented. The agreement between the predicted OBR signal and the measured signal is reasonable. It is interesting to note that the reduction in the backscatter signal at the waist of the narrowest taper is correctly predicted by the model using the single set of averaged fitting parameters. For the narrowest waist width measured, the glass-air interface scattering drops around this region because of increased propagation in the air.

z_{OBR} is plotted versus z in Figure 6.6a to illustrate the impact of the varying effective index on the scattering location as inferred by the OBR instrument. The maximum OBR position error (difference between propagation in tapered and untapered fiber) ranges from 0.13 mm ($w_0 = 1.74\mu$m) to 0.57 mm ($w_0 = 0.49\mu$m) after only 2 mm of light propagation.

Determination of w(z) from the optical backscatter signal

To determine the width versus position profile from the OBR signal trace, the OBR traces are numerically smoothed before analysis to reduce fluctuations. Using the Calculation III procedure, the taper width versus taper position profiles calculated for four of the tapers in Table 6.1 are presented in Figure 6.6b. While the entire taper could be analyzed, the results are presented for one side of the taper. The inferred taper profiles approximately follow an exponential variation with length. For comparison, the SEM-measured profiles of the four tapers are included as the circles. The agreement is good. The relative deviation between the taper profile estimated by OBR and that measured by an SEM is within 20%. A summary of the minimum taper waist widths as inferred from the OBR measurement and the directly measured waist widths using the SEM is provided in Table 6.2. Note that one taper is thin enough (0.49 μm) to exhibit non-monotonic OBR behavior near the taper center. Nonetheless, the taper profile is estimated correctly outside this region.

Table 6.2: Waist Width Comparison of Tapers Pulled at 1660°C

SEM Measurement (μm)	OBR Estimation (μm)	Relative Deviation
0.90	0.93	+3.3%
1.34	1.42	+6.0%
1.74	1.77	+1.7%

Variation of fiber type and pulling temperature

To study the effect of pulling temperature and fiber type on these procedures, three additional SMF-28 fiber tapers were prepared but with the oven temperature set to 1550°C. Also, three SM980 fiber tapers were prepared at this oven temperature. OBR and SEM measurements were performed, and Calculation I in Figure 6.4 was applied to determine the new Rayleigh coefficients ($\alpha_{\text{core}}, \alpha_{\text{clad}}, \beta$) shown in Table 6.3 (note: an SM980 calculation corresponding to Figure 6.3 for SMF-28 was also performed using SM980 fiber parameters: $w_{\text{clad}} = 125\mu\text{m}$, $w_{\text{core}} = 5.7\mu\text{m}$, $n_{\text{core}} = 1.4499$, $n_{\text{clad}} = 1.4440$). Comparing results for the SMF-28 fiber in Table 6.1 and Table 6.3, the coefficient $\bar{\alpha}_{\text{core}}$ is similar in value. On the other hand, when the pulling temperature is lower, the parameter $\bar{\alpha}_{\text{clad}}$ decreases about 40% and $\bar{\beta}$ decreases about 20%, suggesting that the lower temperature pulling reduced the refractive-index fluctuations and surface scattering in the taper. On the other hand, the values of the SMF-28 and SM980 coefficients $\bar{\alpha}_{\text{core}}$, $\bar{\alpha}_{\text{clad}}$ and $\bar{\beta}$ in Table 6.3 for tapers pulled at the same temperature are within the range of the experimental deviation. This is reasonable since the core and cladding compositions of the two fiber types are germanium-doped silica and pure silica, respectively. Their scattering properties should therefore be similar.

As a further test, the average coefficients ($\bar{\alpha}_{\text{core}}, \bar{\alpha}_{\text{clad}}, \bar{\beta}$) were used to determine

Table 6.3: Rayleigh Scattering Coefficients of Taper Types Pulled at 1550°C

SMF-28

Taper Number	Waist Width (μm)	α_{core} (10^{-6}/m)	α_{clad} (10^{-6}/m)	β (10^{-9})
1b	0.90	54.7	56.0	3.38
2b	1.25	39.0	49.1	2.96
3b	1.76	48.6	42.2	2.81
Average		48 ± 8 (17%)	49 ± 7 (14%)	3.0 ± 0.3 (10%)

SM980

Taper Number	Waist Width (μm)	α_{core} (10^{-6}/m)	α_{clad} (10^{-6}/m)	β (10^{-9})
1c	1.37	42.7	52.4	3.18
2c	1.62	36.9	54.3	2.90
3c	2.56	54.7	49.4	3.99
Average		45 ± 9 (20%)	52 ± 3 (6%)	3.4 ± 0.6 (18%)

the backscattering signals of these fibers (Calculation II). Also, Calculation III was applied to determine $w(z)$. The results are presented in Figure 6.7 with comparison to measurements. The relative deviation between the SEM measured and the OBR predicted taper profiles in Figure 6.7b and 6.7d is within 15%. It is interesting to note that the exponential profile observable in the tapers fabricated at higher temperature is not observed in the tapers fabricated at the lower temperature.

Other OBR taper measurements

It is interesting to compare the inferred Rayleigh scattering coefficients for the core and cladding regions of the taper with those computed for the core region of the original (unpulled) optical fiber. Also, because the dominant loss mechanism is expected to be scattering at the wavelengths measured, it is possible to infer a Rayleigh scattering parameter by using the fiber manufacturer's specified attenuation coefficient. This comparison is made in Table 6.4 and results are in fairly close agreement. Here, the Rayleigh coefficient is written as α' in dB/km attenuation units where $\alpha'(\text{dB/km}) = 10^4(\log_{10} e)\alpha(1/\text{m})$ [107], and α is the mks-units form in Eq. (6.1).

Beyond using the OBR analysis to predict the taper profile or to use a taper profile to predict OBR signals, the backscattering method also provides diagnostic information on taper defects such as what might be caused by dust or micro-cracks. As one example, two back-scattering traces are recorded using a dusty taper by recording

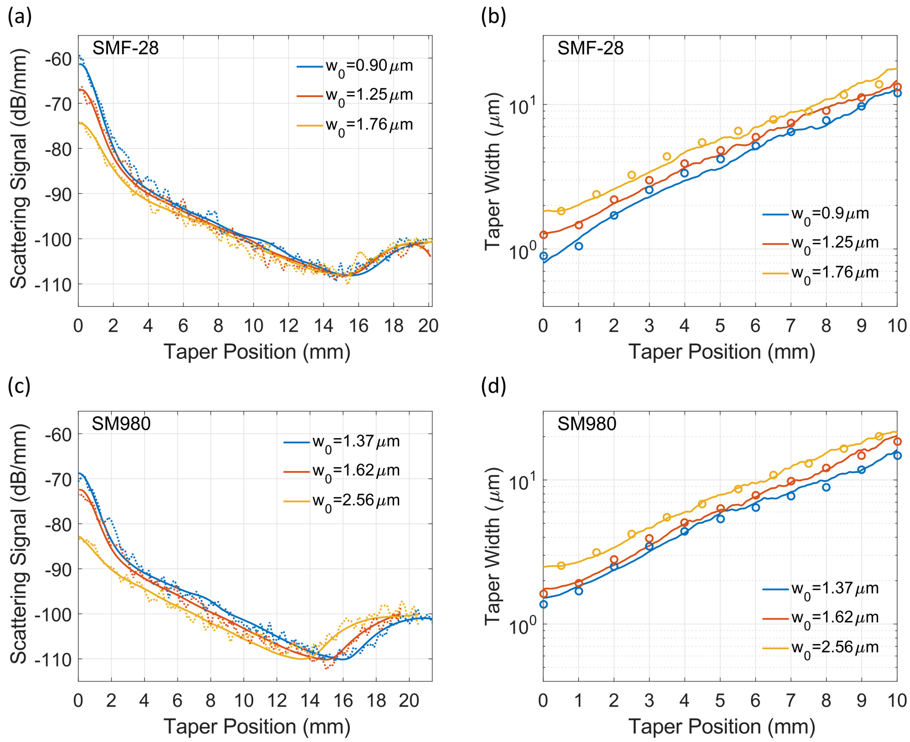

Figure 6.7: **Measured and predicted OBR signals and taper profiles for SMF-28 and SM980 tapers pulled at** 1550°**C. a,** SMF-28 OBR signal traces (dots) and the Calculation II prediction (solid curve). **b,** SMF-28 profiles measured by an SEM (circles) and profiles predicted using Calculation III (solid curves). **c,** SM980 OBR signal traces (dots) and the Calculation II prediction (solid curve). **d,** SM980 profiles measured by an SEM (circles) and profiles predicted using Calculation III (solid curves). Taper waist widths are given in the legend of each panel.

the OBR signal from opposite ends of the taper. The OBR traces in Figure 6.8a contain scattering features that mirror one another, indicating the presence of the dust particles. As another example, Figure 6.8b presents scans of a taper both before and after the appearance of what is believed to be a microcrack. The microcrack formed under application of tension to the taper and is accompanied by the appearance of a spike-like feature near the backscatter maximum. As further evidence of the microcrack, a bright scattering point is observed near the center of the taper when a white LED is shining on the taper region.

6.4 Derivation of Rayleigh scattering coefficient

For convenience, a short derivation of Eq. (6.1) is provided in this section based on the analysis in ref [102]. The taper-guided mode $\vec{E}_n(\vec{r})$ induces a polarization $\vec{P} = \Delta\epsilon(\vec{r})\vec{E}_n = 2\epsilon_o n \Delta n(\vec{r})\vec{E}_n$ (and a displacement current $\vec{J} = i\omega\vec{P}$) through refractive

Table 6.4: Taper Rayleigh Scattering Coefficients Comparison With Optical Fiber

Fiber Type (Temp.)	SMF-28 (1660°C)	SMF-28 (1550°C)	SM980 (1550°C)
α'_{core} (dB/km)	0.20 ± 0.02	0.21 ± 0.03	0.20 ± 0.04
α'_{clad} (dB/km)	0.36 ± 0.04	0.21 ± 0.03	0.23 ± 0.01
OBR Meas. (dB/km)	0.26 ± 0.01	0.23 ± 0.01	0.28 ± 0.01
Data Sheet (dB/km)	0.25	0.25	n.a.*

* Not provided by manufacturer.

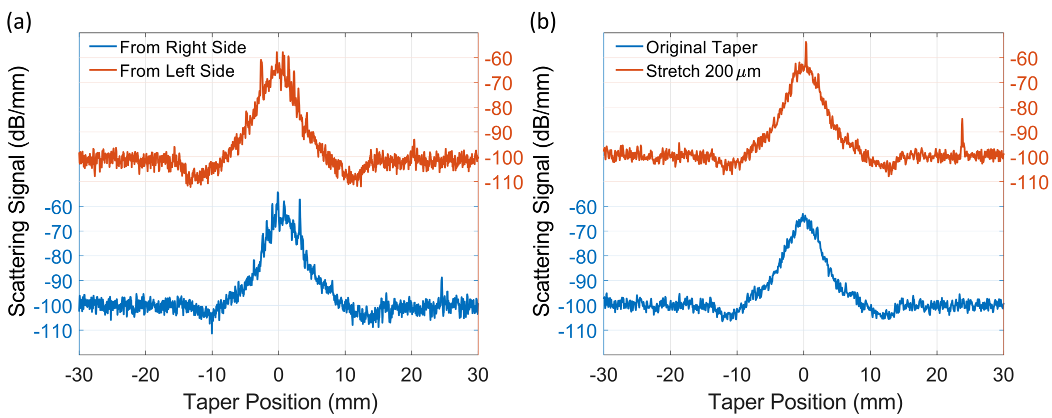

Figure 6.8: **OBR measurements of dust and microcracks. a,** Backscatter traces produced by coupling into the right and left ends of a taper are shown. Evidence of dust or defects on the taper appear as small spikes in the backscatter signal and, as expected, switch sides in the traces relative to the taper center. **b,** The lower trace shows an OBR trace without tension. The upper trace shows the scan when tension is increased to induce what is believed to be a microcrack.

index perturbations $\Delta n(\vec{r})$. $\Delta\epsilon(\vec{r})$ is the dielectric permittivity perturbations, ϵ_o is the vacuum permittivity, and n is the average dielectric refractive index. It is assumed that incident light is single frequency (harmonic time dependence). The fractional amplitude, A_n, of the propagating mode that scatters into the same spatial mode, but propagating in the backward direction, can be determined using the approach described in ref [102] and is given by the following expression,

$$A_n = \frac{-\int_V \vec{J} \cdot \vec{E}_n^* dV}{2\int_S \vec{E}_n \cdot \vec{H}_n^* dS} = \frac{-i\omega}{c} \frac{\int_V \Delta n(\vec{r})|\vec{E}_n(\vec{r})|^2 dV}{\int_{\text{all}} |\vec{E}_n(\vec{r})|^2 dS} \tag{6.9}$$

where $\vec{H}_n$ is the magnetic field, V is the scattering volume (taper volume) such that the volume differential dV can be expressed as $dV = dSdz$ where dS is the differential cross-sectional area and dz is the differential length along the taper axis. In addition, "all" indicates integration over the infinite cross sectional area.

The fraction of the scattered power that couples into the backward guided mode is the ensemble average of the magnitude-squared of Eq. (6.9). If P_{in} and P_s are the input power (assumed constant along the taper) and the backscattered power that is coupled into the guided taper mode, then they are accordingly related by,

$$P_s = \frac{\omega^2}{c^2} \frac{\int_{V'} \int_V |\vec{E}_n(\vec{r})|^2 \left\langle \Delta n(\vec{r}) \Delta n(\vec{r}') \right\rangle |\vec{E}_n(\vec{r}')|^2 dV dV'}{\left(\int_{\text{all}} |\vec{E}_n(\vec{r})|^2 dS\right) \left(\int_{\text{all}} |\vec{E}_n(\vec{r}')|^2 dS'\right)} P_{\text{in}} \tag{6.10}$$

The correlation length of the scattering centers is assumed to be much smaller than the scale of the wavelength. The correlation function of the refractive index fluctuation is therefore taken as proportional to a delta-function,

$$\left\langle \Delta n(\vec{r}) \Delta n(\vec{r}') \right\rangle \equiv \left\langle \Delta n^2 \right\rangle V_c \delta(\vec{r} - \vec{r}') \tag{6.11}$$

where V_c is the scattering volume[102]. This delta-function correlation eliminates one of the volume integrations in Eq. (6.10). Next, by introducing the infinitesimal power $dP_s(z)$ that is scattered from the volume with infinitesimal thickness, dz, the following equation results from Eq. (6.10) after simplification using Eq. (6.11),

$$dP_s(z) = \frac{\omega^2}{c^2} \left\langle \Delta n^2 \right\rangle V_c \frac{\int_S |\vec{E}_n(\vec{r})|^4 dS}{\left(\int_{\text{all}} |\vec{E}_n(\vec{r})|^2 dS\right)^2} P_{\text{in}} dz \tag{6.12}$$

In a statistically homogeneous scattering medium, the Rayleigh scattering coefficient, α, can be related to the refractive index fluctuation $\left\langle \Delta n^2 \right\rangle$ and average refractive index n [107] as follows,

$$\alpha = \frac{32\pi^3 n^2}{3\lambda^4} \left\langle \Delta n^2 \right\rangle V_c \tag{6.13}$$

Upon substitution in Eq. (6.12) this gives the result,

$$\frac{1}{P_{\text{in}}} \frac{dP_s(z)}{dz} = \frac{3\lambda^2}{8\pi n^2} \alpha \frac{\int_S |\vec{E}_n(\vec{r})|^4 dS}{\left(\int_{\text{all}} |\vec{E}_n(\vec{r})|^2 dS\right)^2} \tag{6.14}$$

By assuming there are distinct scattering regions (i.e., core, cladding, surface) with their own corresponding Rayleigh coefficients (α_i, $i \in \{\text{core, clad, ss}\}$), we replace the above single region result by a summation over the regional scattering contributions.

$$\frac{1}{P_{\text{in}}} \frac{dP_s(z)}{dz} = \frac{3\lambda^2}{8\pi n^2} \sum_i \alpha_i \frac{\int_{Si} |\vec{E}_n(\vec{r})|^4 dS}{\left(\int_{\text{all}} |\vec{E}_n(\vec{r})|^2 dS\right)^2} \equiv \sum_i \alpha_i \sigma_i \tag{6.15}$$

As an aside, it is a peculiar coincidence that the field integrals involved in σ_i bear a similarity to the effective area in nonlinear optics [115] despite the very different physical contexts. The surface scattering is assumed to be confined to within a small (compared to the wavelength) uniform thickness (Δt) such that a Rayleigh surface scattering coefficient (β) can be defined from the Rayleigh scattering coefficient within this surface volume (α_{ss}),

$$\frac{3\lambda^2}{8\pi n^2}\alpha_{\text{ss}}\frac{\int_{\text{ss}}|\vec{E}_n(\vec{r})|^4 dS}{\left(\int_{\text{all}}|\vec{E}_n(\vec{r})|^2 dS\right)^2} = \frac{3\lambda^2}{8\pi n^2}\,\alpha_{\text{ss}}\Delta t\frac{\oint_{\text{interface}}|\vec{E}_n(\vec{r})|^4 dl}{\left(\int_{\text{all}}|\vec{E}_n(\vec{r})|^2 dS\right)^2} \equiv \beta\eta \tag{6.16}$$

where,

$$\beta \equiv \alpha_{\text{ss}}\Delta t \tag{6.17}$$

6.5 Conclusion

When combined with modeling, optical backscatter reflectometry provides a way to characterize the width versus position profile of an optical fiber taper. The OBR signal, itself, also measures the mode evolution from fiber core to taper waveguiding as it propagates through the taper. The model developed to fit the data accounts for scattering mechanisms associated with the fiber core and cladding of the bulk silica glass as well as surface scattering along the narrow portions of the taper. It also includes the variation of backscatter coupling into the taper guided mode on account of the varying taper width. Rayleigh scattering coefficients for core, cladding, and taper surface were extracted by fitting the model with the OBR data. The experimentally-determined Rayleigh backscattering coefficients for the core and cladding are consistent with those inferred from attenuation data in the fiber manufacturer's datasheet. The OBR method of taper characterization is nondestructive and can be performed while the taper is within its fabrication system. Moreover, it can be used to measure defects and contamination. The method also provides a convenient way to calibrate a taper pulling recipe. The OBR characterization method developed here could be applied to analyze width variations in chip-integrated waveguides.

Chapter 7

SUMMARY AND CONCLUSION

In this thesis, we reviewed the basic concepts of the optical gyroscope, whisper gallery mode resonator, and Brillouin lasing process. By introducing the counter-propagating Brillouin lasers in a microresonator, we made a chip-based solid-state ring laser gyroscope. We further unlocked the gyroscope by the offset-counter-pumping, and measured the sinusoidal rotation rate as small as 5 °/h. The 36 mm disk gyroscope achieved a bias drift at 3.6 °/h. Furthermore, we measured the Earth's rotation by this gyroscope. This is the first time that the Earth's rotation is measured by a chip-based optical gyroscope.

In addition, we introduced the physics of the gyroscope, and showed how the mode-pulling, rotation, dissipative coupling, and Kerr nonlinearity affected the gyroscope operation. We further checked the enhancement near the exceptional point, and demonstrated a 4× boost of the Sagnac factor. We examined how the gyroscope readout is affected by the power and temperature drift, and showed the temperature feedback control by using the backaction of the cascaded Brillouin laser.

We demonstrated a prototype of the chip-based optical gyroscope, which can measure the Earth's rotation. In the future, we hope that the gyroscope could be fully integrated with photonics and electronics, so the robust system would be immune to the shock and resistant to the vibration noise, and could be further used for the aerospace applications.

Appendix A

DERIVATION OF THE SAGNAC FORMULA

In this appendix, we derive the Sagnac formulas of the fiber optical gyroscope and the ring laser gyroscope. To simplify the derivation in the classical region, here we assume that the velocity at any point of the gyroscope caused by the rotation is much smaller than the speed of light.

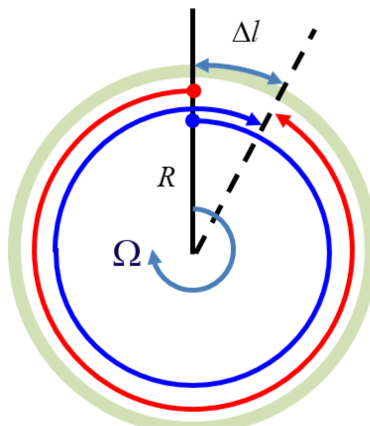

Figure A.1: **Model of the Sagnac effect.** When a free space loop is rotating, the CW and CCW lights travel back to the same point on the loop with a round trip path length difference, Δl. The radius of the loop is R, and the angular velocity is Ω.

A.1 Sagnac phase shift in the fiber optical gyroscope

Let us consider a closed loop in the free space with radius R and angular velocity Ω. When the loop is steady ($\Omega = 0$), both the lights have a round trip time:

$$\tau_r = \frac{2\pi R}{c}. \tag{A.1}$$

When the loop is rotating ($\Omega \neq 0$), the round trip path length difference, Δl, becomes:

$$\Delta l = \Omega R \tau_r. \tag{A.2}$$

The counter-propagating path length difference, ΔL, becomes:

$$\Delta L = L_{\mathrm{CW}} - L_{\mathrm{CCW}} = 2\Delta l = 2\Omega R \tau_r = \frac{4\pi\Omega R^2}{c}, \tag{A.3}$$

where c is the speed of light, and L_{CW} (L_{CCW}) is the CW (CCW) path length. Therefore, the round trip time difference between two lights, Δt, is

$$\Delta t = \frac{\Delta L}{c} = \frac{4\pi\Omega R^2}{c^2}. \tag{A.4}$$

We can measure this round trip time difference by using the interferometry, and readout the phase difference, $\Delta\phi$, as follows:

$$\Delta\phi = \Delta t \frac{2\pi c}{\lambda} = \frac{8\pi^2 R^2 \Omega}{c\lambda}, \tag{A.5}$$

where λ is the wavelength of light. Since the area of the gyroscope, A, is defined by $A \equiv \pi R^2$, the final equation is

$$\Delta\phi = \frac{8\pi A}{c\lambda}\Omega. \tag{A.6}$$

Next, let us consider a fiber optical gyroscope made from the dielectric medium with refractive index, n. At rest, the round trip time becomes $n\tau_r$ since the speed of light in the medium is c/n. The round trip path length difference under rotation becomes $n\Delta l$. The CW and CCW (free space) path lengths under rotation become:

$$L^*_{\mathrm{CW}} = 2\pi R + n\Delta l = 2\pi R + \frac{2\pi n \Omega R^2}{c} \tag{A.7}$$

$$L^*_{\mathrm{CCW}} = 2\pi R - n\Delta l = 2\pi R - \frac{2\pi n \Omega R^2}{c}. \tag{A.8}$$

When the medium is rotating, the speed of light is no longer the same due to the Fresnel-Fizeau drag [116]. The moving medium changes the speed of light in the CW and CCW directions:

$$v_{\mathrm{CW}} = \frac{c}{n} + \alpha_d \Omega R \tag{A.9}$$

$$v_{\mathrm{CCW}} = \frac{c}{n} - \alpha_d \Omega R, \tag{A.10}$$

where α_d is the Fresnel-Fizeau drag coefficient:

$$\alpha_d = 1 - n^{-2}. \tag{A.11}$$

The new round trip time difference between two lights, Δt^*, is

$$\Delta t^* = \frac{L^*_{\mathrm{CW}}}{v_{\mathrm{CW}}} - \frac{L^*_{\mathrm{CCW}}}{v_{\mathrm{CCW}}} = \frac{2\pi R + \frac{2\pi n \Omega R^2}{c}}{\frac{c}{n} + \alpha_d \Omega R} - \frac{2\pi R - \frac{2\pi n \Omega R^2}{c}}{\frac{c}{n} - \alpha_d \Omega R}. \tag{A.12}$$

We simplify the equation by assuming $c^2/n^2 \gg \alpha_d \Omega^2 R^2$:

$$\Delta t^* \approx \frac{4\pi R^2 n^2 \Omega (1 - \alpha_d)}{c^2} = \frac{4\pi \Omega R^2}{c^2} = \Delta t. \tag{A.13}$$

The phase difference keeps the same with the presence of medium:

$$\Delta\phi \approx \frac{8\pi A}{c\lambda}\Omega. \tag{A.14}$$

If we have N loops of fiber under arbitrary rotation, the final equation becomes:

$$\Delta\phi = \frac{8\pi N \mathbf{A} \cdot \Omega}{c\lambda}. \tag{A.15}$$

A.2 Sagnac frequency shift in the ring laser gyroscope

Now we derive the Sagnac formula in the ring laser gyroscope. When the resonator is steady, the mode frequency is calculated by

$$mc = \nu_m P, \tag{A.16}$$

where m is the modal number, c the speed of light, ν_m the modal resonant frequency, and P the optical path length of the mode. When the resonator is rotating, the resonant frequency is shifted due to the change of the optical path length:

$$\nu_{m,\mathrm{CW}} = \frac{mc}{P_{\mathrm{CW}}}, \tag{A.17}$$

$$\nu_{m,\mathrm{CCW}} = \frac{mc}{P_{\mathrm{CCW}}}, \tag{A.18}$$

where $\nu_{m,\mathrm{CW}}$ ($\nu_{m,\mathrm{CCW}}$) is the resonant frequency of the CW (CCW) mode, and P_{CW} (P_{CCW}) the optical path length of the CW (CCW) mode. Therefore, the frequency splitting under rotation, $\Delta\nu$, becomes [117]:

$$\Delta\nu = \nu_{m,\mathrm{CCW}} - \nu_{m,\mathrm{CW}} = mc\left(\frac{1}{P_{\mathrm{CCW}}} - \frac{1}{P_{\mathrm{CW}}}\right) \approx mc\frac{\Delta P}{P^2} = \nu_m\frac{\Delta P}{P}, \tag{A.19}$$

where ΔP is the round trip path length difference between CW and CCW modes. According to the Eq. (A.13), this path length difference is calculated by

$$\Delta P = c\Delta t^* \approx \frac{4\pi R^2\Omega}{c}. \tag{A.20}$$

In addition, in a circular ring resonator, the optical path length of the mode is defined by

$$P = 2\pi R n_g, \tag{A.21}$$

where n_g is the group velocity of the mode. Therefore, the frequency splitting of a ring laser gyroscope under rotation is

$$\Delta\nu = \nu_m\frac{2R\Omega}{n_g c} = \frac{D\Omega}{n_g\lambda}, \tag{A.22}$$

where D is the diameter of the resonator. We can write the formula in a general form:

$$\Delta\nu = \frac{4\mathbf{A}\cdot\Omega}{\lambda P}. \tag{A.23}$$

Appendix B

OTHER SYSTEM DIAGRAMS

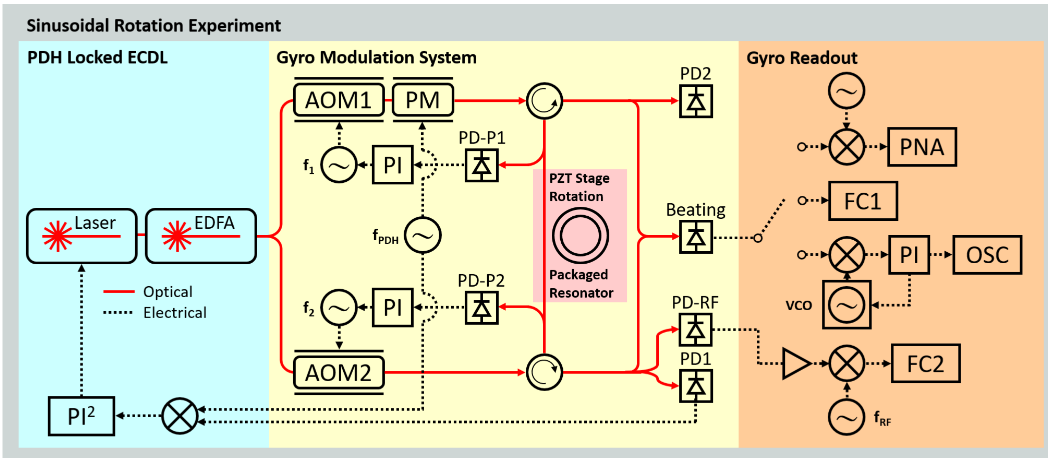

Figure B.1: **Sinusoidal rotation experiment.** The ECDL amplified by the EDFA is PDH-locked to the microcavity. The independent AOMs control the pump detuning frequency, and actively stabilize both pump powers. The gyroscope package is put on a piezo-electric stage with a sinusoidal displacement modulation. The whole gyro modulation system is enclosed in an environmental chamber to minimize the drift. The readout signals are monitored by photodetectors (PDs), and analyzed by the phase noise analyzer (PNA), frequency counter (FC), or oscilloscope (OSC). PM: phase modulator, PI: proportional-integral servo, RF: radio frequency, VCO: voltage controlled oscillator.

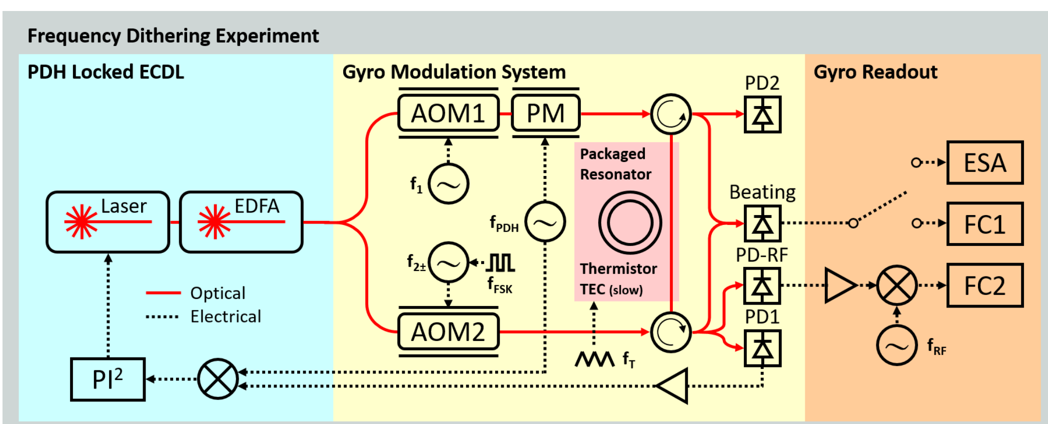

Figure B.2: **Frequency dithering experiment.** A frequency-shift keying (FSK) signal flips the pump detuning frequency periodically to generate dithering signal. The frequency dithering allows the tracking of common frequency and difference frequency in the readout. A slow triangular frequency can be added to the TEC to modulate the sample temperature so the thermal response of the SBL beating signal can be analyzed.

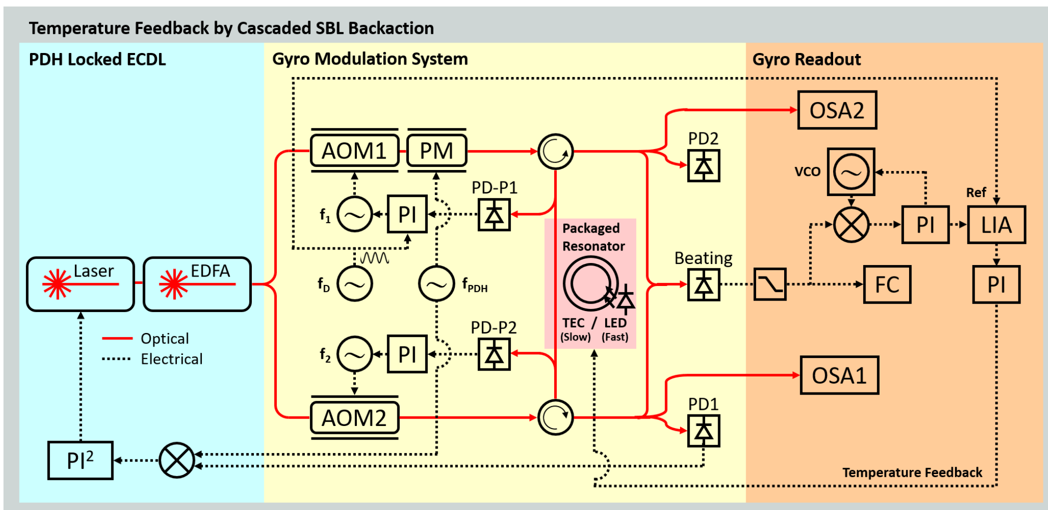

Figure B.3: **Temperature feedback by cascaded SBL backaction.** A sinusoidal power dithering is applied to the cascaded SBL power. The backaction of the cascaded SBL generates a frequency modulation on the SBL beating signal. The dithered SBL beating signal is converted to a voltage signal by a frequency tracking circuit. Then, the shift amplitude is resolved by a lock-in amplifier (LIA) to generate a feedback signal for the LED and TEC. The feedback suppresses the longterm temperature drift.

BIBLIOGRAPHY

[1] Post, E. J. Sagnac effect. *Rev. Mod. Phys.* **39**, 475–493 (1967).

[2] Armenise, M. N., Ciminelli, C., Dell'Olio, F. & Passaro, V. M. N. *Advances in Gyroscope Technologies* (Springer Science & Business Media, 2010).

[3] Chow, W. W. *et al.* The ring laser gyro. *Rev. Mod. Phys.* **57**, 61–104 (1985).

[4] Lefèvre, H. C. *The Fiber-Optic Gyroscope* (Artech House, 2014), 2nd edn.

[5] Udd, E. & Spillman Jr., W. B. *Fiber Optic Sensors* (John Wiley & Sons, 2011), 2nd edn.

[6] Burns, W. K. *Optical Fiber Rotation Sensing* (Academic Press, 1994).

[7] Passaro, V. M. N., Cuccovillo, A., Vaiani, L., De Carlo, M. & Campanella, C. E. Gyroscope technology and applications: A review in the industrial perspective. *Sensors* **17**, 2284 (2017).

[8] King, A. D. Inertial navigation – forty years of evolution. *GEC Rev.* **13**, 140–149 (1998).

[9] Barbour, N. Inertial navigation sensors. *NATO RTO Lecture Ser.* **116**, 1–24 (2004).

[10] Liu, K. *et al.* The development of micro-gyroscope technology. *J. Micromechanics Microengineering* **19**, 113001 (2009).

[11] Dell'Olio, F., Tatoli, T., Ciminelli, C. & Armenise, M. Recent advances in miniaturized optical gyroscopes. *JEOS:RP* **9**, 14013 (2014).

[12] Li, J., Suh, M.-G. & Vahala, K. J. Microresonator Brillouin gyroscope. *Optica* **4**, 346–348 (2017).

[13] Gundavarapu, S. *et al.* Sub-Hertz fundamental linewidth photonic integrated Brillouin laser. *Nat. Photon.* **13**, 60–67 (2019).

[14] Gundavarapu, S. *et al.* Interferometric optical gyroscope based on an integrated Si3N4 low-loss waveguide coil. *J. Light. Technol.* **36**, 1185–1191 (2018).

[15] Liang, W. *et al.* Resonant microphotonic gyroscope. *Optica* **4**, 114–117 (2017).

[16] Maayani, S. *et al.* Flying couplers above spinning resonators generate irreversible refraction. *Nature* **558**, 569–572 (2018).

[17] Khial, P. P., White, A. D. & Hajimiri, A. Nanophotonic optical gyroscope with reciprocal sensitivity enhancement. *Nat. Photon.* **12**, 671–675 (2018).

[18] Shahriar, M. S. *et al.* Ultrahigh enhancement in absolute and relative rotation sensing using fast and slow light. *Phys. Rev. A* **75**, 053807 (2007).

[19] Yariv, A., Xu, Y., Lee, R. K. & Scherer, A. Coupled-resonator optical waveguide: a proposal and analysis. *Opt. Lett.* **24**, 711–713 (1999).

[20] Heebner, J. E., Boyd, R. W. & Park, Q.-H. Scissor solitons and other novel propagation effects in microresonator-modified waveguides. *J. Opt. Soc. Am. B* **19**, 722–731 (2002).

[21] F.R.S., L. R. O. Cxii. the problem of the whispering gallery. *Philos. Mag.* **20**, 1001–1004 (1910).

[22] Vahala, K. J. Optical microcavities. *Nature* **424**, 839–846 (2003).

[23] Matsko, A. B. & Ilchenko, V. S. Optical resonators with whispering gallery modes I: Basics. *IEEE J. Sel. Top. Quant. Electron.* **12**, 3–14 (2006).

[24] Ilchenko, V. S. & Matsko, A. B. Optical resonators with whispering-gallery modes-part ii: applications. *IEEE J. Sel. Top. Quantum Electron.* **12**, 15–32 (2006).

[25] Tomes, M. & Carmon, T. Photonic micro-electromechanical systems vibrating at X-band (11-Ghz) rates. *Phys. Rev. Lett.* **102**, 113601 (2009).

[26] Grudinin, I. S., Matsko, A. B. & Maleki, L. Brillouin lasing with a CaF_2 whispering gallery mode resonator. *Phys. Rev. Lett.* **102**, 043902 (2009).

[27] Li, J., Lee, H. & Vahala, K. J. Microwave synthesizer using an on-chip Brillouin oscillator. *Nat. Commun.* **4**, 2097 (2013).

[28] Eggleton, B. J., Poulton, C. G. & Pant, R. Inducing and harnessing stimulated Brillouin scattering in photonic integrated circuits. *Adv. Opt. Photon.* **5**, 536–587 (2013).

[29] Bahl, G., Tomes, M., Marquardt, F. & Carmon, T. Observation of spontaneous Brillouin cooling. *Nat. Phys.* **8**, 203–207 (2012).

[30] Spillane, S. M., Kippenberg, T. J. & Vahala, K. J. Ultralow-threshold Raman laser using a spherical dielectric microcavity. *Optica* **415**, 621–623 (2002).

[31] Kippenberg, T. J. & Vahala, K. J. Cavity optomechanics: back-action at the mesoscale. *Science* **321**, 1172–1176 (2008).

[32] Eichenfield, M., Chan, J., Camacho, R., Vahala, K. J. & Painter, O. Optomechanical crystals. *Nature* **462**, 78–82 (2009).

[33] Grudinin, I. S., Lee, H., Painter, O. & Vahala, K. J. Phonon laser action in a tunable two-level system. *Phys. Rev. Lett.* **104**, 083901 (2010).

[34] Chan, J. *et al.* Laser cooling of a nanomechanical oscillator into its quantum ground state. *Nature* **478**, 89–92 (2011).

[35] Monifi, F. *et al.* Optomechanically induced stochastic resonance and chaos transfer between optical fields. *Nat. Photon.* **10**, 399–405 (2016).

[36] Kippenberg, T. J., Holzwarth, R. & Diddams, S. A. Microresonator-based optical frequency combs. *Science* **332**, 555–559 (2011).

[37] Del'Haye, P. *et al.* Optical frequency comb generation from a monolithic microresonator. *Nature* **450**, 1214–1217 (2007).

[38] Herr, T. *et al.* Temporal solitons in optical microresonators. *Nat. Photon.* **8**, 145–152 (2014).

[39] Brasch, V. *et al.* Photonic chip-based optical frequency comb using soliton Cherenkov radiation. *Science* **351**, 357–360 (2016).

[40] Yi, X., Yang, Q. F., Yang, K. Y., Suh, M. G. & Vahala, K. J. Soliton frequency comb at microwave rates in a high-Q silica microresonator. *Optica* **2**, 1078–1085 (2015).

[41] Carmon, T. & Vahala, K. J. Visible continuous emission from a silica microphotonic device by third-harmonic generation. *Nat. Phys.* **3**, 430–435 (2007).

[42] Peng, B. *et al.* Loss-induced suppression and revival of lasing. *Science* **346**, 328–332 (2014).

[43] Bino, L. D., Silver, J. M., Stebbings, S. L. & Del'Haye, P. Symmetry breaking of counter-propagating light in a nonlinear resonator. *Sci. Rep.* **7**, 43142 (2017).

[44] Aoki, T. *et al.* Observation of strong coupling between one atom and a monolithic microresonator. *Nature* **443**, 671–674 (2006).

[45] Srinivasan, K. & Painter, O. Linear and nonlinear optical spectroscopy of a strongly coupled microdisk-quantum dot system. *Nature* **450**, 862–865 (2007).

[46] Yang, K. Y. *et al.* Bridging ultrahigh-Q devices and photonic circuits. *Nat. Photon.* **12**, 297–302 (2018).

[47] Suh, M.-G., Yang, Q.-F. & Vahala, K. J. Phonon–limited–linewidth of Brillouin lasers at cryogenic temperatures. *Phys. Rev. Lett.* **119**, 143901 (2017).

[48] Li, J., Lee, H., Chen, T. & Vahala, K. J. Characterization of a high coherence, Brillouin microcavity laser on silicon. *Opt. Express* **20**, 20170–20180 (2012).

[49] Alnis, J. *et al.* Thermal-noise-limited crystalline whispering-gallery-mode resonator for laser stabilization. *Phys. Rev. A* **84**, 011804 (2011).

[50] Lee, H. *et al.* Spiral resonators for on-chip laser frequency stabilization. *Nat. Commun.* **4**, 2468 (2013).

[51] Spencer, D. T. *et al.* An optical-frequency synthesizer using integrated photonics. *Nature* **557**, 81–85 (2018).

[52] Suh, M.-G., Yang, Q.-F., Yang, K. Y., Yi, X. & Vahala, K. J. Microresonator soliton dual-comb spectroscopy. *Science* **354**, 600–603 (2016).

[53] Suh, M.-G. *et al.* Searching for exoplanets using a microresonator astrocomb. *Nat. Photon.* **13**, 25–30 (2019).

[54] Yang, Q.-F. *et al.* Vernier spectrometer using counterpropagating soliton microcombs. *Science* **363**, 965–968 (2019).

[55] Suh, M.-G. & Vahala, K. J. Soliton microcomb range measurement. *Science* **359**, 884–887 (2018).

[56] Trocha, P. *et al.* Ultrafast optical ranging using microresonator soliton frequency combs. *Science* **359**, 887–891 (2018).

[57] Bao, C., Suh, M.-G. & Vahala, K. J. Microresonator soliton dual-comb imaging. *arXiv:1809.09766* (2018).

[58] Newman, Z. L. *et al.* Photonic integration of an optical atomic clock. *arXiv:1811.00616* (2018).

[59] Spillane, S. M., Kippenberg, T. J., Painter, O. J. & Vahala, K. J. Ideality in a fiber-taper-coupled microresonator system for application to cavity quantum electrodynamics. *Phys. Rev. Lett.* **91**, 043902 (2003).

[60] Jung, Y., Brambilla, G. & Richardson, D. J. Polarization-maintaining optical microfiber. *Opt. Lett.* **35**, 2034–2036 (2010).

[61] Ippen, E. & Stolen, R. Stimulated Brillouin scattering in optical fibers. *Appl. Phys. Lett.* **21**, 539–541 (1972).

[62] Kobyakov, A., Sauer, M. & Chowdhury, D. Stimulated Brillouin scattering in optical fibers. *Adv. Opt. Photon.* **2**, 1–59 (2010).

[63] Otterstrom, N. T., Behunin, R. O., Kittlaus, E. A., Wang, Z. & Rakich, P. T. A silicon Brillouin laser. *Science* **360**, 1113–1116 (2018).

[64] Niklés, M., Thévenaz, L. & Robert, P. A. Brillouin gain spectrum characterization in single-mode optical fibers. *J. Lightwave Technol.* **15**, 1842–1851 (1997).

[65] Kim, J., Kuzyk, M. C., Han, K., Wang, H. & Bahl, G. Non-reciprocal Brillouin scattering induced transparency. *Nat. Phys.* **11**, 275–280 (2015).

[66] Adler, R. A study of locking phenomena in oscillators. *Proceedings of the IRE* **34**, 351–357 (1946).

[67] Lee, H. *et al.* Chemically etched ultrahigh-Q wedge-resonator on a silicon chip. *Nat. Photon.* **6**, 369–373 (2012).

[68] Lai, Y.-H., Yang, K. Y., Suh, M.-G. & Vahala, K. J. Fiber taper characterization by optical backscattering reflectometry. *Opt. Express* **25**, 22312–22327 (2017).

[69] Black, E. D. An introduction to Pound-Drever-Hall laser frequency stabilization. *Am. J. Phys.* **69**, 79–87 (2001).

[70] Hotate, K. & Tabe, K. Drift of an optical fiber gyroscope caused by the faraday effect: influence of the earth's magnetic field. *Appl. Opt.* **25**, 1086–1092 (1986).

[71] K., H. & Tabe, K. Drift of an optical fiber gyroscope caused by the faraday effect: Experiment. *J. Light. Technol.* **5**, 997–1001 (1987).

[72] El-Ganainy, R. *et al.* Non-Hermitian physics and PT symmetry. *Nat. Phys.* **14**, 11 (2018).

[73] Feng, L., El-Ganainy, R. & Ge, L. Non-Hermitian photonics based on parity-time symmetry. *Nat. Photon.* **11**, 752 (2017).

[74] Miri, M.-A. & Alù, A. Exceptional points in optics and photonics. *Science* **363**, eaar7709 (2019).

[75] Ren, J. *et al.* Ultrasensitive micro-scale parity-time-symmetric ring laser gyroscope. *Opt. Lett.* **42**, 1556–1559 (2017).

[76] Sunada, S. Large Sagnac frequency splitting in a ring resonator operating at an exceptional point. *Phys. Rev. A* **96**, 033842 (2017).

[77] Vollmer, F. & Arnold, S. Whispering-gallery-mode biosensing: label-free detection down to single molecules. *Nat. Methods* **5**, 591–596 (2008).

[78] Lu, T. *et al.* High sensitivity nanoparticle detection using optical microcavities. *Proc. Natl. Acad. Sci. U.S.A.* **108**, 5976–5979 (2011).

[79] Vollmer, F. & Yang, L. Review label-free detection with high-Q microcavities: a review of biosensing mechanisms for integrated devices. *Nanophotonics* **1**, 267–291 (2012).

[80] Zhu, J. *et al.* On-chip single nanoparticle detection and sizing by mode splitting in an ultrahigh-Q microresonator. *Nat. Photon.* **4**, 46–49 (2010).

[81] Xu, X., Jiang, X., Zhao, G. & Yang, L. Phone-sized whispering-gallery microresonator sensing system. *Opt. Express* **24**, 25905–25910 (2016).

[82] Wiersig, J. Sensors operating at exceptional points: General theory. *Phys. Rev. A* **93**, 033809 (2016).

[83] Wiersig, J. Enhancing the sensitivity of frequency and energy splitting detection by using exceptional points: Application to microcavity sensors for single-particle detection. *Phys. Rev. Lett.* **112**, 203901 (2014).

[84] Liu, Z.-P. *et al.* Metrology with $\mathcal{PT}$-symmetric cavities: Enhanced sensitivity near the $\mathcal{PT}$-phase transition. *Phys. Rev. Lett.* **117**, 110802 (2016).

[85] Hodaei, H. *et al.* Enhanced sensitivity at higher-order exceptional points. *Nature* **548**, 187–191 (2017).

[86] Chen, W., Özdemir, Ş. K., Zhao, G., Wiersig, J. & Yang, L. Exceptional points enhance sensing in an optical microcavity. *Nature* **548**, 192–196 (2017).

[87] Cai, M., Painter, O. & Vahala, K. J. Observation of critical coupling in a fiber taper to a silica-microsphere whispering-gallery mode system. *Phys. Rev. Lett.* **85**, 74 (2000).

[88] Zhang, M. *et al.* Quantum noise theory of exceptional point sensors. *arXiv:1805.12001* (2018).

[89] Loh, W. *et al.* Dual-microcavity narrow-linewidth Brillouin laser. *Optica* **2**, 225–232 (2015).

[90] Knight, J. C., amd F. Jacques, G. C. & Birks, T. A. Phase-matched excitation of whispering-gallery-mode resonances by a fiber taper. *Opt. Lett.* **22**, 1129–1131 (1997).

[91] Vetsch, E. *et al.* Optical interface created by laser-cooled atoms trapped in the evanescent field surrounding an optical nanofiber. *Phys. Rev. Lett.* **104**, 203603 (2010).

[92] Goban, A. *et al.* Demonstration of a state-insensitive, compensated nanofiber trap. *Phys. Rev. Lett.* **109**, 033603 (2012).

[93] Birks, T. A., Wadsworth, W. J. & Russell, P. S. J. Supercontinuum generation in tapered fibers. *Opt. Lett.* **25**, 1415–1417 (2000).

[94] Wadsworth, W. J. *et al.* Supercontinuum generation in photonic crystal fibers and optical fiber tapers: a novel light source. *J. Opt. Soc. Am. B* **19**, 2148–2155 (2002).

[95] Lu, P., L. Men, K. S. & Chen, Q. Tapered fiber Mach-Zehnder interferometer for simultaneous measurement of refractive index and temperature. *Appl. Phys. Lett.* **94**, 131110 (2009).

[96] ao, O. F., Caldas, P., Araújo, F. M., Ferreira, L. A. & Santos, J. L. Optical flowmeter using a modal interferometer based on a single nonadiabatic fiber taper. *Opt. Lett.* **32**, 1974–1976 (2007).

[97] Alton, D. J. Interacting single atoms with nanophotonics for chip-integrated quantum networks. *PhD thesis, California Institute of Technology, Chap. 7* (2013).

[98] Ding, L., Belacel, C., Ducci, S., Leo, G. & Favero, I. Ultralow loss single-mode silica tapers manufactured by a microheater. *Appl. Opt.* **49**, 2441–2445 (2010).

[99] Snyder, A. W. & Love, J. D. *Optical waveguide theory* (Chapman and Hall, London, 1983).

[100] Birks, T. A. & Li, Y. W. The shape of fiber tapers. *J. Lightwave Tech.* **10**, 432–438 (1992).

[101] Hartog, A. H. & Gold, M. P. On the theory of backscattering in single-mode optical fibers. *J. Lightwave Tech.* **2**, 76–82 (1984).

[102] Nakazawa, M. Rayleigh backscattering theory for single-mode optical fibers. *J. Opt. Soc. Am.* **73**, 1175–1180 (1983).

[103] Soller, B. J., Gifford, D. K., Wolfe, M. S. & Froggatt, M. E. High resolution optical frequency domain reflectometry for characterization of components and assemblies. *Opt. Express* **13**, 666–674 (2005).

[104] Glombitza, U. & Brinkmeyer, E. Coherent frequency-domain reflectometry for characterization of single-mode integrated-optical waveguides. *J. Lightwave Tech.* **11**, 1377–1384 (1993).

[105] Barfuss, H. & Brinkmeyer, E. Modified optical frequency domain reflectometry with high spatial resolution for components of integrated optic systems. *J. Lightwave Tech.* **7**, 3–10 (1989).

[106] Eickhoff, W. & Ulrich, R. Optical frequency domain reflectometry in single-mode fiber. *Appl. Phys. Lett.* **39**, 693–695 (1981).

[107] Lines, M. E. Scattering losses in optic fiber materials, I. a new parametrization, II. numerical estimates. *J. Appl. Phys.* **55**, 4052–4063 (1984).

[108] Tsujikawa, K., Tajima, K. & Zhou, J. Intrinsic loss of optical fibers. *Opt. Fiber Tech.* **11**, 319–331 (2005).

[109] Ohashi, M., Shiraki, K. & Tajima, K. Optical loss property of silica-based single-mode fibers. *J. Lightwave Tech.* **10**, 539–543 (1992).

[110] Yariv, A. *Electronics in modern communications, 5th edn., Chap. 3* (New York: Oxford University, 1997).

[111] Borselli, M., Johnson, T. & Painter, O. Beyond the Rayleigh scattering limit in high-Q silicon microdisks: theory and experiment. *Opt. Express* **13**, 1515–1530 (2005).

[112] Gorodetsky, M. L., Pryamikov, A. D. & Ilchenko, V. S. Rayleigh scattering in high-Q microspheres. *J. Opt. Soc. Am. B* **17**, 1051–1057 (2000).

[113] Saito, K. *et al.* Limit of the Rayleigh scattering loss in silica fiber. *Appl. Phys. Lett.* **83**, 5175–5177 (2003).

[114] Sakaguchi, S. & Todoroki, S. Rayleigh scattering of silica core optical fiber after heat treatment. *Appl. Opt.* **37**, 7708–7711 (1998).

[115] Agrawal, G. P. *Nonlinear Fiber Optics, 4th edn.* (Academic Press, 2006).

[116] Vali, V., Shorthill, R. W. & Berg, M. F. Fresnel-fizeau effect in a rotating optical fiber ring interferometer. *Appl. Opt.* **16**, 2605–2607 (1977).

[117] Jacobs, S. F. & Zanoni, R. Laser ring gyro of arbitrary shape and rotation axis. *Am. J. Phys.* **50**, 659–660 (1982).